ABSTRACT

Title of dissertation: UNDERSTANDING ELECTRIC FIELD-ENHANCED TRANSPORT FOR THE MEASUREMENT OF NANOPARTICLES AND THEIR ASSEMBLY ON SURFACES

De-Hao Tsai, Doctor of Philosophy, 2007

Directed by: Michael R. Zachariah, Professor.

Departments of Mechanical Engineering and Chemistry

The goal of this dissertation is to understand the synthesis, characterization, and integration of nanoparticles and nanoparticle-based devices by electric field-enhanced transport of nanoparticles. Chapter 1 describes the factors used for determining particle trajectories and found that electric fields provide the directional electrostatic force to overcome other non-directional influences on particle trajectories. This idea is widely applied in the nanoparticle classification, characterization, and assembly onto substrate surfaces as investigated in the following chapters.

Chapter 2 presents a new assembly method to position metal nanoparticles delivered from the gas phase onto surfaces using the electrostatic force generated by biased p-n junction patterned substrates. Aligned deposition patterns of metal nanoparticles were observed, and the patterning selectivity quantified. A simple model accounting for the generated electric field, and the electrostatic, van der Waals, and image forces was used to explain the observed results. Chapter 2.2 describes a data set

for particle size resolved deposition, from which a Brownian dynamics model for the process can be evaluated. Brownian motion and fluid convection of nanoparticles, as well as the interactions between the charged nanoparticles and the patterned substrate, including electrostatic force, image force and van der Waals force, are accounted for in the simulation. Using both experiment and simulation the effects of the particle size, electric field intensity, and the convective flow on coverage selectivity have been investigated. Coverage selectivity is most sensitive to electric field, which is controlled by the applied reverse bias voltage across the p-n junction. A non-dimensional analysis of the competition between the electrostatic and diffusion force is found to provide a means to collapse a wide range of process operating conditions and an effective indicator or process performance. Directed assembly of size-selected nanoparticles has been applied in the study of nanoparticle enhanced fluorescence (NEF) bio-sensing devices.

Chapter 3 presents results of a systematic examination of functionalized gold nanoparticles by electrospray-differential mobility analysis (ES-DMA). Formation of selfassembled monolayers (SAMs) of alkylthiol molecules and singly stranded DNA (ssDNA) on the Au-NP surface was detected from a change in particle mobility, which could be modeled to extract the surface packing density. A gas-phase temperature-programmed desorption (TPD) kinetic study of SAMs on the Au-NP found the data to be consistent with a second order Arrhenius based rate law, yielding an Arrhenius-factor of 1×10^{11} s^{-1} and an activation energy ~105 kJ/mol. This study suggests that the ES-DMA can be added to the tool set of characterization methods being employed and developed to study the structure and properties of coated nanoparticles.

Chapter 3.2 demonstrates this ES-DMA as a new method to investigate colloidal aggregation and the parameters that govern it. Nanoparticle suspensions were characterized by sampling a Au nanoparticle (Au-NP) colloidal solution via electrospray (ES), followed by differential ion-mobility analysis (DMA) to determine the mobility distribution, and thus the aggregate distribution. By sampling at various times, the degree of flocculation and the flocculation rate are determined and found to be inversely proportional to the ionic strength and proportional to the residence time. A stability ratio at different ionic strengths, the critical concentration, and surface potential or surface charge density of Au-NPs are obtained from these data. This method should be a generically useful tool to probe the early stages of colloidal aggregation.

Study of ES-DMA is extended to include the characterizations of a variety of materials. Biologically interested materials such as viruses and antibodies could also be characterized. These results show ES-DMA provides a general way to characterize the colloidal materials as well as aerosolized particles.

UNDERSTANDING ELECTRIC FIELD-ENHANCED TRANSPORT FOR THE MEASUREMENT OF NANOPARTICLES AND THEIR ASSEMBLY ON SURFACES

by

De-Hao Tsai

Dissertation submitted to the Faculty of the Graduate School of the
University of Maryland, College Park in partial fulfillment
of the requirements for the degree of
Doctor of Philosophy
2007

Advisory Committee:

Professor Gregory S. Jackson, Chair
Professor Michael R. Zachariah
Professor Raymond J. Phaneuf
Professor Gottlieb S. Oehrlein
Professor Sheryl H. Ehrman

Dedication

This dissertation is dedicated to my dear grandfather, General Ta-Yeh Tsai. His love, honor, and integrity will stay with my family forever.

Acknowledgements

Foremost, I sincerely thank my advisor Professor Michael Zachariah for his consistent support throughout the years of my Ph.D. study. I especially appreciate his efforts in educating me on scientific thought and research, and providing an opportunity to carry out my research work. I would also like to thank Professor Ray Phaneuf and Dr. Leonard Pease for their guidance, collaboration, and invaluable research assistance with my academic study.

During the years of studying at the University of Maryland, I have been fortunate to meet with numerous talented people including my research group members, Prahalad, Takumi, Zhou, Ashish, Kuk, Martin, Kyle, Anand, Ahmet, Purnendu, Dibyendu, and Soo, my senior friends, Kao-Shuo, Wei, and Jae, and my friends at NIST, especially Rebecca, Kristen, and Chip. I would like to take this opportunity to thank all of them for providing several memorable moments that I will cherish forever. I would also like to thank Professor Greg Jackson, Professor Sheryl Ehrman, and Professor Gottlieb S. Oehrlein for their advice and help with my dissertation.

At end thanks are also reserved for my parents and relatives, whose blessings and firm support have shaped me into a better person.

Table of Contents

List of Figures

Chapter 1

Chapter 2

Chapter 3

Figure 3.7: Arrhenius plots for three different sizes of Au-MUA particles. T=200-350°C. t =0.3 s for 20 nm Au-NPs and t =1.2 s for both 30 nm and 60 nm Au-NPs. Y^*=Ln(ρ^{*-1}-1)-Ln(At). The slope = $-E/R$. R =gas constant (8.314 Jmol^{-1}K^{-1}).

Figure 3.8: Interaction potential for two spherical colloidal nanoparticles (Particle diameter is 10 nm). Surface potential is 64 mV. Curve 1 represents particles in the reaction-limited regime (C = 1 mmol/L), Curve 2 represents particles in the intermediate regime (C = 3 mmol/L), and Curve 3 represents particles in the diffusion-limited regime(C = 20 mmol/L). a is the radius of the particles, r is the center-to-center distance between two particles, and $h = r-2a$. C is the salt concentration.

Figure 3.9: (a) Ion-mobility spectrum of colloidal Au ammonium acetate solution at different ionic strength conditions. Mobility size of individual particles is ≈10 nm. (b) $N_{c,n=1}/N_0$ vs different ionic strength conditions listed in (a). $N_{g,n}$ is the number concentration of Au particles measured by DMA-CPC in the gas phase ($N_{g,n}^* = N_{g,n}/N_0$), N_0 is the initial concentration of monomer Au particles, and n is the number of single particles in a Au aggregate. Volumetric fraction of Au-NP in solution is ~10^{-6}, and the reaction time t of sampled Au-NPs is ≈ 20 mins.

Figure 3.10: (a) Ion-mobility spectra of unconjugated colloidal Au vs reaction time, t. Mobility size of monomer is ~10 nm. a: C=2.12 mmol/L ; b: C=4.21 mmol/L ; c: C=7.89 mmol/L.

Figure 3.11: (a) Number concentration of different Au-aggregates vs reaction time. C=7.89 mmol/L. $N_{c,n}$ is the number concentration of Au-NP in solution, and n is the number of individual particles in one aggregate. □: n = 1; □: n = 2; ▲: n = 3; ×: n = 4. (b) Degree of flocculation, DF, vs reaction time. C varies from 4.21 mmol/L to 9.47 mmol/L.

Figure 3.12: Total number concentration of Au–NPs in solution, N_{total}, vs. reaction time.

Figure 3.13: Stability ratio of Au colloids vs ionic strength; the interpolate on the *X*-axis (concentration of ammonium acetate) represents the critical concentration of salt needed for flocculation of Au colloids, n_c.

Figure 3.14: (a) Dimensionless analysis. W vs E_a^*. (b) E_a^* vs $d_{p,n=1}$ (primary particle diameter) obtained by Eq. 3.8 by assuming a constant surface charge density, 0.075 e/nm^2.

Figure 3.15: Two typical particle size distributions of nominally 20 nm Au particles, one bare (o) and the other coated with $(dT)_{20}$-SH (x). The difference between the two particle size distributions determines the apparent coating thickness.

Figure 3.16: Apparent coating thickness, H, versus number of dT nucleotides per strand, N_b, for a variety of salt concentrations, n_s. The dashed and solid lines respectively represent fits for a contour length model for fully stretched out DNA versus that of a square root dependence [$H = 1.1 N_b^{0.53} n_s^{0.35}$ nm L$^{0.35}$ mol$^{-0.35}$] characteristic of strands coiled into low grafting density layers.

Figure 3.17: The surface coverage versus the salt concentration of the ssDNA solution in which the particles were immersed during preparation. Shorter strands display higher surface coverages because each strand occupies a smaller footprint.

Figure 3.18: Ion-mobility spectrum of virus particles. (a) PP7 (b) PR772. (c) Size distribution of PR772 sample after being dialyzed and stored at room temperature for 18 weeks. Samples were 5-times diluted by 2mM ammonium acetate solution. (d) TEM images of sized classified (50 nm, 60 nm) PR772 collected after 18 weeks.

Figure 3.19: Number density versus the mobility size for various agglomerates of IgG. (a) Rabbit IgG at 18 µg/mL (120 nmol/L or $7.3 \cdot 10^{13}$ antibodies/mL) and pH 8 in 20 mmol/L ammonium acetate. (b) Human IgG previously lyophilized at approximately 75 µg/mL (500 nmol/L or $3.0 \cdot 10^{14}$ antibodies/mL) and pH 8 in 2.0 mmol/L ammonium acetate.

Appendix

Chapter 1

Introduction

1.1 Overview

Functionalization of nanoparticles (NPs) has become one of the major focus areas in the material research society with applications in electronics[1], pharmaceuticals[2, 3], and chemical[4]/biological sensors[2, 5]. An example, gold and silver nanoparticles can be applied in the diagnostics for bio-molecules because their unique plasmon bands effectively enhance the detection limits of the sensing processes[2, 5-7].

To integrate these nanoparticles into future applications, a key is to understand their transport properties, which can impact material synthesis, classification, characterization and integration processes.

Brownian motion, particle drag and the external force are the major factors affecting nanoparticles' transports [8-11]. Hence the external force includes the net force from all external fields acting on the particles, such as electric fields, magnetic fields and van der Waals attractions. Particle drag is defined as the particle resistance to momentum change caused by external fields, and this resistance is due to directional collisions of the surrounding medium molecules to nanoparticles. Brownian motion is induced by non-directional, random collisions between the particle and molecules in the surrounding

medium, which is important especially when the size of materials goes down to the nano-scale.

My dissertation is focused on the study of nanoparticle transport properties in the gas phase, and the enhanced transport properties by applying an electric field. The advantage of transporting nanoparticles in a gas is that it is a clean medium[12] and it offers minimal resistance to steer/direct the trajectories of charged nanoparticles. By choosing polarities of particles and adjusting the intensity of the electric field one can control their trajectory, which can be applied to the classification, characterization, and assembly of these nano-sized particles. In Chapter 2 and 3 we will discuss further on these applications.

1.2 Electric Field Enhanced Transport

Generally, twokinds of external forces are acting on nanoparticles in an electric field [9, 11, 13]. One is the van der Waals force, which is attractive, non-directional, and always presents between two objects. The other is the electrical force. Generally, the electrostatic force is the major electrical force when applying a uniform, time-invariant electric field to minimize the effect of nanoparticle polarization; this force is defined as a charged object having a coulomb interaction with the surrounding electric field. The electrostatic force is a directional, long-range force, can be employed for directing particle trajectories. Upon application of a sufficient electric field, the electrostatic force can overcome the van der Waals forces in the gas phase, so that particle can be controlled

by the applied electric field. Next we discuss the theory for using electric field to measure particle size distributions and directed-assembly of particles onto patterned surfaces.

1.3 Differential Mobility Analysis (DMA)

The idea behind measuring particle sizes with electric fields is based onto measuring the electrical mobility of NPs based on their time-of-flight physics[14, 15]. Figure 1.1 shows in-flight particles in a differential mobility analyzer. A convective flow (sheath flow) having a constant velocity, U, is used to carry the particle in the X-direction, which is usually fixed during the mobility analysis. In the vertical (r) direction, the particle's velocity is determined by its electrical velocity, v_e, which is a function of electrical mobility of the particle, Z_e, and the applied voltage in the mobility analyzer, V_{DMA} [v_e= f(V_{DMA}, Z_e)],

$$t = \frac{L_s}{U} = \frac{h_{DMA}}{v_{e,r}} = \frac{h_{DMA}}{f(V_{DMA}, Z_e)} \tag{1.1}$$

Here L_s and h_{DMA} are design parameters of the mobility analyzer from the manufacturer [15]. For a constant-time measurement, $v_{e,r}$, U, L_s and h_{DMA} are all constant, and the only variables left in Eq. 1.1 are V_{DMA} and Z_e. Hence, the electrical mobility of different sized nanoparticles can be measured from a balance of electrical and drag forces by ramping through V_{DMA}.

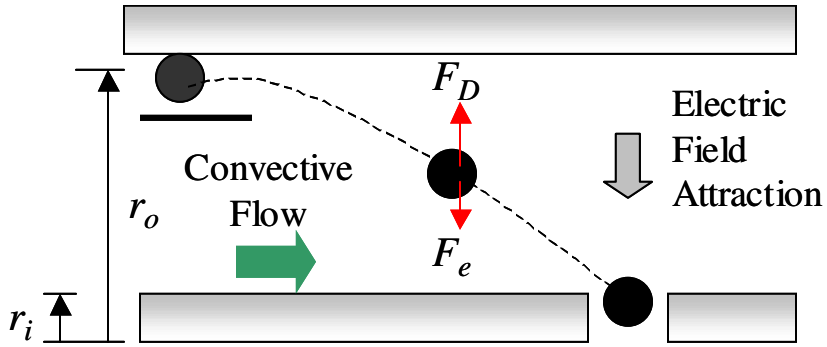

Figure 1.1: Description of in-flight particles in a differential mobility analyzer. F_e is the electrostatic force, and F_D is the drag force, which retards the motion.

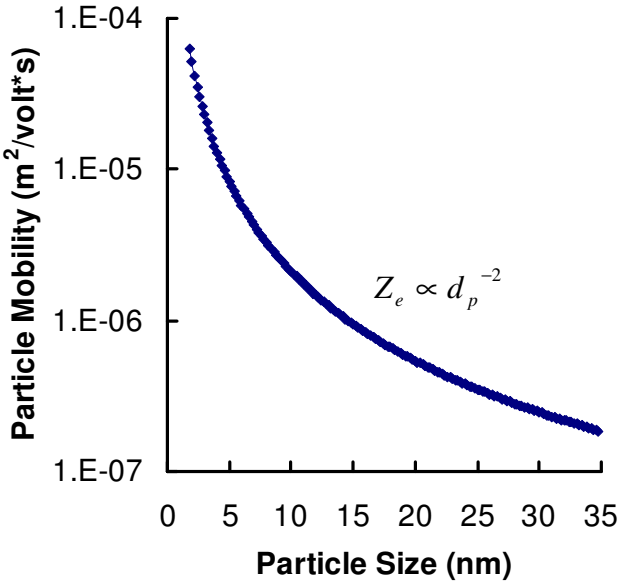

Figure 1.2: Electrical mobility versus particle size (in the free molecular regime). Particle size is expressed as the diameter of particles.

1.3.1 Electrical Mobility of Nanoparticles in Gas Phase

Similar to the electrical mobility of an electron[16], the electrical mobility of a charged NP, Z_e, can also be measured through its electrical drift velocity,

$$Z_e = v_e / E, \tag{1.2}$$

where E is the applied electric field in the differential mobility analyzer. To determine the mobility we balance the electrical and drag forces.

$$F_e = F_D \tag{1.3}$$

$$F_e = neE \tag{1.4}$$

$$F_D = \frac{3\pi\mu\chi d_p v_e}{C_c} \quad . \tag{1.5}$$

Then Z_e can be derived from Eq. 1.2 to Eq. 1.5,

$$Z_e = \frac{v_e}{E} = \frac{neC_c}{3\pi\mu d_p \chi} \quad , \tag{1.6}$$

where n is number of unit charges, e is the elementary charges ($1.6*10^{-19}$ coulombs), μ is the viscosity of surrounding medium, d_p is the particle size, C_c is the Cunningham slip correction factor ($C_c = 1 + \frac{\lambda}{d}[2.34 + 1.05\exp(-0.39\frac{d}{\lambda})]$) [14] and χ is the shape factor used for nano-sized materials having different shapes (for a spherical NP, χ=1). An example plot for converting particle mobility into particle diameter is shown in Figure 1.2. For

nano-sized particles (d_p<100 nm), Z_e is approximately proportional to d_p^{-2} because C_c is proportional to d^{-1}, approximately.

1.3.2 Electric Field in Gas Phase

To study how nanoparticle trajectories are affected by the electric field, it is necessary to obtain the electric field distribution within the DMA. For simplification, the applied electric field directing particle trajectory is assumed to be one-dimensional and perpendicular to the direction of convective flow. For a cylindrical electrostatic classifier having a central-rod electrode (Figure 1), the electric field attraction is in the axial direction (r-direction),

$$E_r = \frac{dV}{dr} = \frac{-V_{DMA}}{r \ln(ro/ri)} \quad . \tag{1.7}$$

Here r is the position of in-flight particle, r_o and r_i are the outer and inner diameter of the DMA, respectively. By getting E_r from Eq. 1.7 then Z_e can be obtained through Eq. 1.2.

In addition to the electric field and particle drag, the Brownian motion of a particle should also be included in the particle trajectory analysis, as it adds uncertainty to the field-directed trajectory. Generally, increasing the applied field in the DMA can effectively reduce the importance of Brownian motion because the electrical velocity increases without changing the diffusional velocity. A further discussion of electrostatics versus diffusion is included in Chapter 2.2.

1.3.3 Charge Neutralization of Aerosolized Nanoparticles

Generally, the size of nanoparticles of interest to us is less than 100 nm. Figure 1.3 shows[15] the ratio of singly and doubly charged particles to all particles versus particle diameter under charge equilibrium. Clearly, when particle size is less than 20 nm, the probability of forming doubly charged (n=2) particles is negligible. In contrast, when the particle size is larger than 150 nm, the probability of forming multiply-charged particle becomes significant (>5 %), which is a significant challenge to the size purification processes. For spherical-like particles ranging less than 100 nm, we use a factor, β, to represent the ratio of singly charged positive particle to the total number of particles in the gas phase [15, 17]: (the unit of d_p is nanometer)

$$\beta = 10^{[-2.3484+0.6044\log(d_p)+0.48\log(d_p)^2+0.0013\log(d_p)^3-0.1553\log(d_p)^4+0.032\log(d_p)^5]} \quad (1.8)$$

In order to obtain β, it is necessary to bring nano-sized materials to charge equilibrium before entering the DMA. An aerosol neutralization process can bring the charge distribution of aerosolized particles from a non-equilibrium state (unknown charge ratio) to equilibrium with a known Boltzmann charge distribution[14, 17]. Briefly, the radioactive source bi-polarly charges the surrounding gas molecules. Nanoparticles passing through this housing collide with these charged gas molecules, and become charge-neutralized. From β the number concentration of all particles can be calculated based on the number of singly charged, positive particles measured by DMA after charge equilibrium.

[Number of particles]= β^{-1}*[Number of singly-charged positive particles] (1.9)

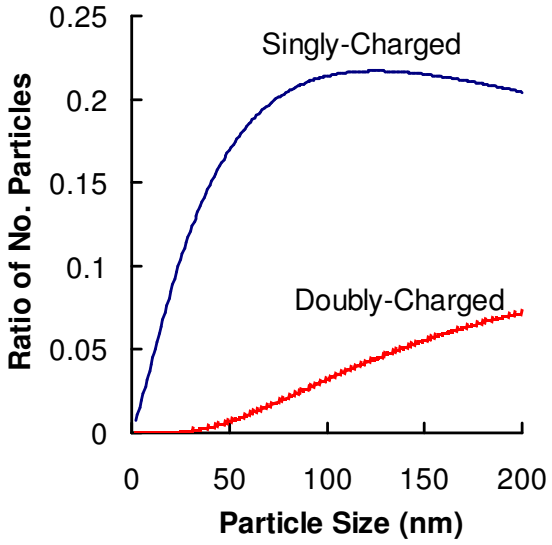

Figure 1.3: Ratio of singly and doubly charged particles to all particles versus particle diameter in charge equilibrium. Assume particles are positive and spherical.

1.3.3 Differential Ion-mobility spectrum and the Particle Size Distribution

Ion-mobility spectra of NPs (i.e. their number density versus particle mobility) are obtained by using an electrostatic classifier followed by a condensation particle counter (CPC). As changing V_{DMA}, particles having a specific Z_e are classified under different V_{DMA}. Then the number concentration of these mobility-classified NPs, $N_{g,p}$, is characterized by the CPC and recorded by a personal computer. By knowing β (Eq. 1.8) and mobility size (Fig 2), the ion mobility spectrum can be converted into a full particle size distribution representing the status before the DMA.

This ion-mobility spectrum can be widely applied toward many potential applications. For example: the DMA may be used for characterization of the size of spherical particles, the length of nanotubes and nanorods, and the coating thickness on nanoparticles. Moreover, this ion-mobility spectrum can be applied as an electrostatic classification tool to obtain size-selected nano-materials, which can be used in many applications requiring high size purity [13].

1.4 Electrostatic Deposition of Nanoparticles

In addition to being able to characterize functional nanoparticles, integrating these particles into the device engineering is important for nanoparticle applications. However, fabrication of nanoparticle-based devices requires effective deposition of nanoparticles onto a substrate surface and accurate alignment of nanoparticles in specific locations. The most obvious and effective method to position particles is through the use of electrostatic forces. Compared to micron-sized materials, nanoparticles are difficult to bring from the gas phase onto a substrate surface by simple impaction due to their low inertia[14]. Because the Stokes number of nanoparticles is <<1, particles follow the gas streamline if there is no external field. In contrast, they have relatively high electrical mobilities due to their low drag (Eq. 1.6). Hence, electrostatic deposition is a promising method to assemble these nanoparticles onto the substrates. For example, in commercially-available electrostatic deposition systems[18], the deposition efficiency is highly dependent on the particle size and smaller sized NPs have higher deposition efficiency (100 % when $d < 30$ nm). We can estimate the yield of a deposition process as:

$$Yield = (Concentration \quad in \quad Gas \ Phase) * (Deposition \quad Efficiency) \ . \quad (1.10)$$

In the following chapters we will use these concepts to characterize and deposit nanoparticles.

Chapter 2

Directly-Assembly of Functional Nanoparticles on a Field Generating Substrate-Applications in Nanotechnology

2.1. Electrostatic-Directed Deposition of Nanoparticles on a Field Generating Substrate

2.1.1 Introduction

Functional nanoparticles have been widely considered as the building blocks of potential micro- and nano-scale electronic, optoelectronic devices and gas sensors [12, 19]. Fabrication of nanoparticle based devices would require accurate alignment of nanoparticles in specific locations. The most obvious and effective method to position particles is through the use of electrostatic forces. For example Jacobs et al. [20-22] demonstrated that charged carbon nanoparticles could be aligned with an electric field on a charge-patterned substrate. Fissan et al. [23-25] also applied a contact charging method by employing a metal-coated polymer stamp to form charging patterns on an insulating substrate, where the oppositely charged nanoparticles were eventually attracted and aligned. For 30 nm-sized particles, the best lateral resolution achieved with this method was around ~100 nm. However, the gas-phase patterning of nanoparticles on a charge-patterned substrate still has many difficulties, including: (i) the charge patterns are

relatively unstable, and change during the particle deposition process, (ii) the metal-coated polymer stamp is easily damaged in the charging process, (iii) the necessity of using an insulated surface on the substrate, limits its applications especially on metal-semiconductor devices.

We have approached the problem of particle alignment from the point of view of developing a substrate that could be easily patterned and fabricated with traditional microelectronic process methods as well as possessing thermal and chemical stability. To that end we have considered the simplest device structure, a planar p-n junction. Upon bias of the junction, an electric field is established on the charge depletion zone. We will demonstrate the use of this field to direct nanoparticles deposited from the gas-phase.

2.1.2 Directed Assembly Approach

As is well known, in the region where the P and N type doped regions are in contact, electrons from the N-type diffuse toward the P-type region and combine with holes to form a charge depletion zone, resulting in a build-up of a net charge in each region. Upon reverse bias the width of the charge depletion region is increased, and an additional electric field is established on the charge depletion zone [26].

Our goal is to use the field generated in the depletion zone under various conditions of reverse bias to assess the feasibility of directing the motion and deposition of charged nanoparticles.

We begin with a simple analysis of the expected magnitude of the forces on the particles and the deposition selectivity. The electric field E in the vertical direction of the substrate, Y is given by:

$$E = \frac{Q}{4\pi\varepsilon_g\varepsilon_0 r^2} \times \frac{Y}{r} \qquad (2.1)$$

Where $r = \sqrt{X^2 + Y^2}$, X is the horizontal distance between a particle and the charged surface of a substrate, Y is the vertical distance between a particle and the substrate, ε_g is the dielectric constant of the carrier gas N_2 (=1.0006), and Q is the net charge in each depletion zone.

Figure 2.1 presents the schematic of a p-n junction patterned substrate, consisting of arrays of p-type GaAs stripes (number concentration of acceptors, N_A=10^{19} cm^{-3}; 0.3 cm in length, 1 μm in width and 30 μm gap between p-stripes) within n-type GaAs (number concentration of donors, N_D=10^{18} cm^{-3}). The calculated built-in potential (V_{bi}) of this substrate is 1.45 V, calculated as follows[16],

$$V_{bi} = \frac{kT}{e}\ln\left(\frac{N_A N_D}{N_i^2}\right) \qquad (2.2)$$

Where k is Boltzmann's constant, T is the temperature, N_i is the intrinsic carrier concentration of GaAs (=1.79×10^6 cm^{-3}) and e is the elementary unit of charge (=1.6×10^{-19} C). The total width of the charge depletion zone, d_{n+p}, was estimated to be around 50 nm[27]. To simplify the calculation of the electric field generated from the p-n junction, the thickness of p-type-doped GaAs layer on this substrate was assumed to be 1μm. With the

parameters of N_A, N_D, and d_{n+p}, we can estimate the net charge in the depletion zone (Q) and estimate E, the generated field, using Equation 1.

The electrostatic force on a charged particle is given by,

$$F_e = n\ e\ E \tag{2.3}$$

Where n is the number of unit charges on an incoming nanoparticle, and E is the net electric field generated from the p-n junction patterned substrate, at that location in space.

Taking into account the van der Waals force (F_{vdw}) and the image force (F_i) between particles and a substrate, we can obtain the net external force (F_{ext}) on a particle in the vertical direction as follows [9, 25],

$$F_i = -\frac{(ne)^2}{4\pi\varepsilon_g\varepsilon_0(2Y)^2}\frac{\varepsilon_s-\varepsilon_g}{\varepsilon_s+\varepsilon_g} \tag{2.4}$$

$$F_{vdw} = -\frac{2}{3}A_h\frac{(\frac{d}{2})^3}{(Y-\frac{d}{2})^2(Y+\frac{d}{2})^2} \tag{2.5}$$

$$F_{ext} = F_e + F_{vdw} + F_i \tag{2.6}$$

where d is the particle diameter and A_h is the Hamaker constant of metal particles in the air (= 4×10^{-19} J). Note that both F_{vdw} and F_i are attractive forces.

The net external force exerting on a spherical particle is a function of the position (X, Y) above the substrate. When nanoparticles are initially located far from the substrate (Y>>100 nm), the electrostatic force is relatively strong compared with the van der Waals

and image forces, so that the trajectory of nanoparticles depends only on F_e. Because of the random nature of Brownian motion, a direct calculation including this effect becomes computational quite expensive. However, Brownian motion is only important when the electric force is weak. Once a particle is close to the surface of the substrate (Y<100 nm), the effect of Brownian motion is negligible because F_e, F_{vdw}, and F_i increase significantly. Figure 2.2 presents the net external force acting on a negatively singly-charged 50 nm particle at an applied bias of –0.9 V at various heights above the surface. Positive and negative values of the net external force represent repulsive and attractive forces, respectively. As one can see, the negatively charged particles are repelled by p-type regions and attracted by n-type regions, particularly at the interface of p-n junctions, where the local field is highest. As the negatively charged particles get closer to the substrate they experience stronger attracting or repelling forces. If the polarity of the particle is changed to positive, the opposite situation is expected, i.e. the particles should preferentially array in the P-type regions.

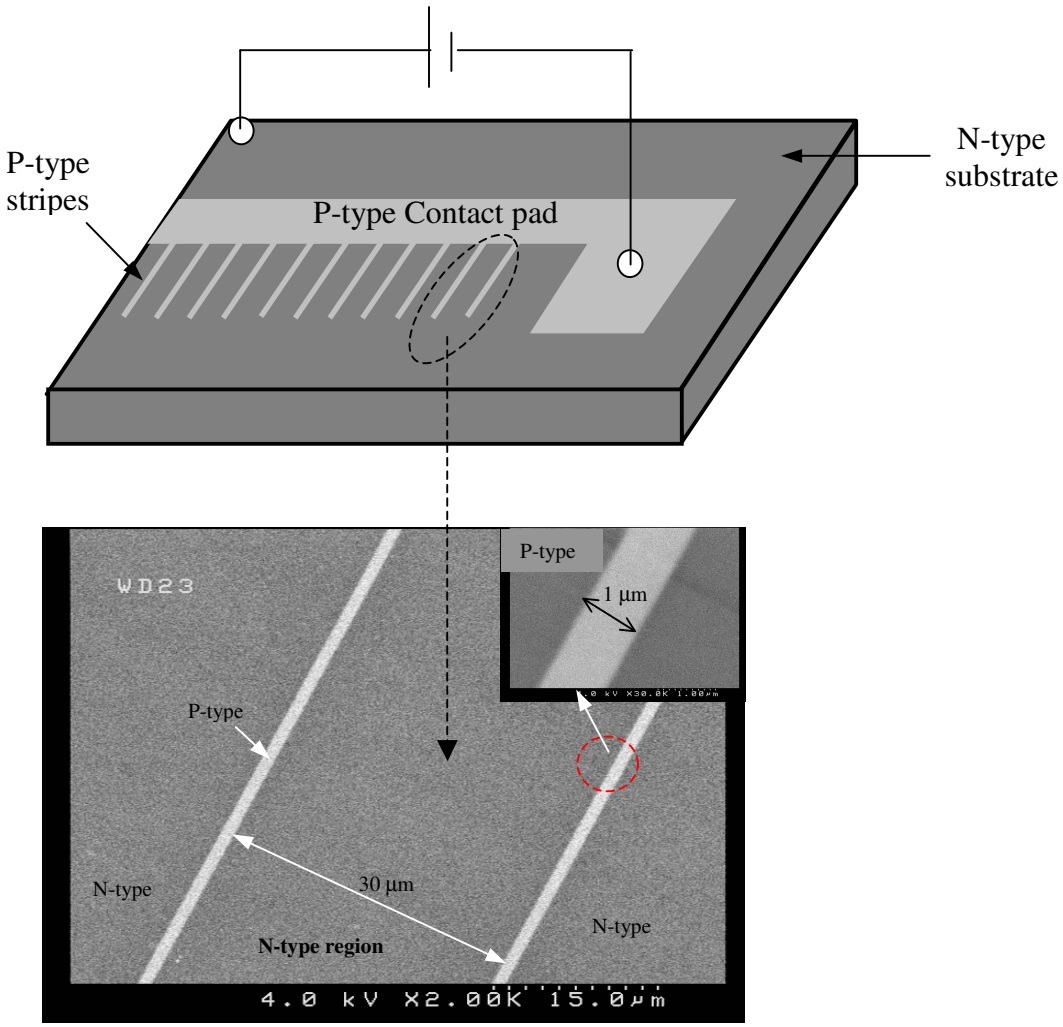

Figure 2.1: The schematic of a p-n junction patterned substrate.

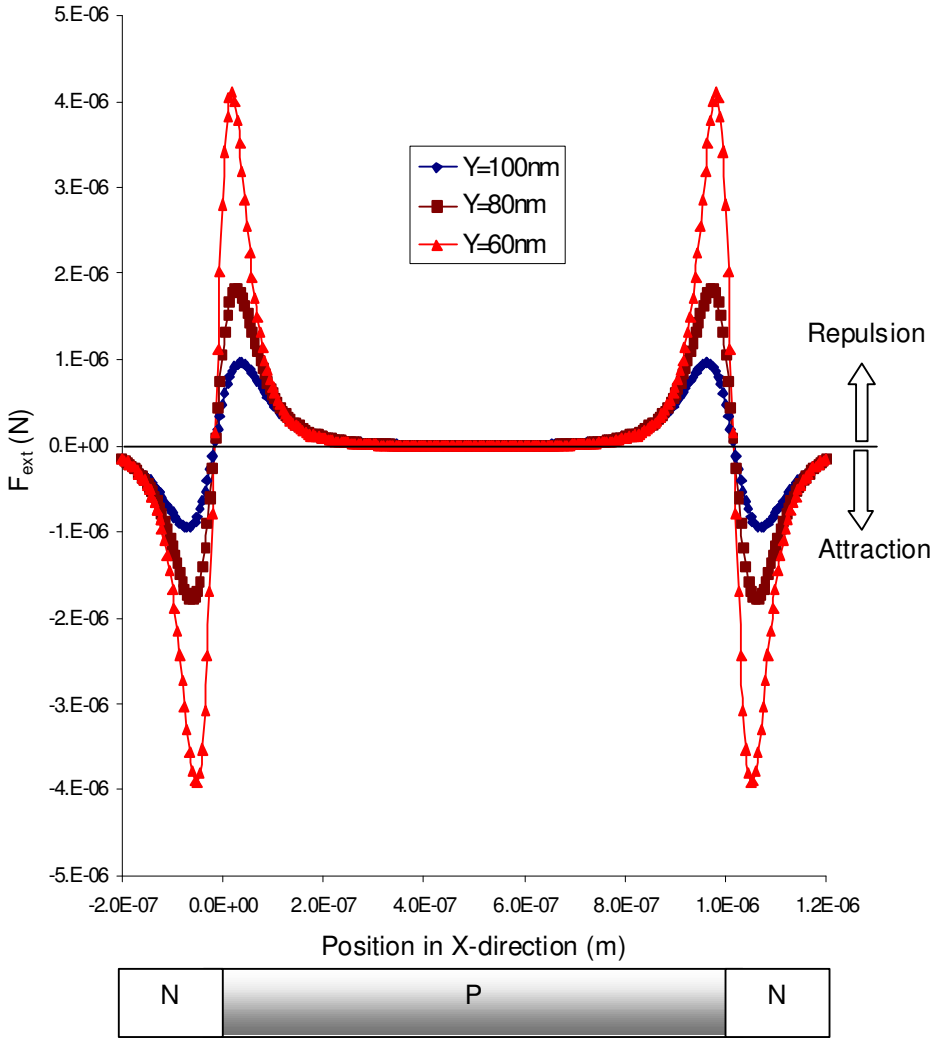

Figure 2.2: The net external force on an incoming negatively charged nanoparticle across a p-n junction-patterned substrate. Three curves express different vertical positions at Y=60nm, 80nm and 100nm. (Calculation conditions: d_p =50 nm, V_{bias} = -0.9 V).

2.1.3 Experimental

Figure 2.3 presents a schematic of the experimental system. Nickel nanoparticles were generated by pulsed laser ablation (PLA) from a solid nickel target (99.995%, Lesker, 1″ O.D. × 0.125″ in thickness), using a 1064 nm Q-switched Nd:YAG laser operating at 10 Hz with a pulse duration of 4 ns. The choice of nickel was based on an eventual goal of using the particles as catalysts for carbon nanotube growth. The laser beam is focused on the solid nickel target, which leads to vaporization of the target material due to local micro-plasma formation on the target surface. The nickel vapor was continuously swept by 2 lpm nitrogen carrier gas, and then rapidly quenched and nucleated into nickel nanoparticles in the gas phase.

To measure the particle size distribution of nickel particles generated by PLA, we used a differential mobility analyzer (DMA model 3081, TSI, Inc.) for selecting monodisperse particles based on their electrical mobility, and a condensation particle counter (CPC, model 3025A, TSI, Inc.) for counting the number concentration [28]. The polydisperse nickel particles were then sent to a tube furnace at 1000^{o}C to sinter the particles. The sintered particles were then passed through a unipolar charger composed of six radioactive ionizing Po-210 strips (0.5 mCi) circumferentially placed in the entrance of the charger which then flowed into a ±300 V/cm DC field to remove either positive or negative ions so that only one polarity of ions remained in the charger [29]. Inside the unipolar charger, nanoparticles become uni-polarly charged by the charge transfer from the gas-ions.

The p-n junction-patterned substrate was n-type GaAs (Si doped) coated with SiO_2. Photolithography was used to define lines for the p-type doping. The p-type doping was created by ion implantation of Zn^+ ions through the SiO_2 layer. The photoresist was then removed and the oxide layer stripped before rapid thermal annealing for activation of the Zn^+ ions. For particle deposition, the p-n junction-patterned substrate was connected to a DC power supply and placed in a deposition chamber (9 cm in I.D. and 10 cm in height) with an aerosol feed nozzle (2 mm in I.D.) 1 cm above the substrate. Reverse bias was applied by connecting the p-type doped contact pad with the cathode of the DC power supply, and the n-type doped substrate with the anode of the power supply (as shown in Figure 1). The bias across the substrate was varied from 0 to -2.5V, and current measured was less than 0.02 mA. The nanoparticle deposition pattern was observed with a Hitachi S-4000 field emission scanning electron microscope (SEM) operated at 4 kV.

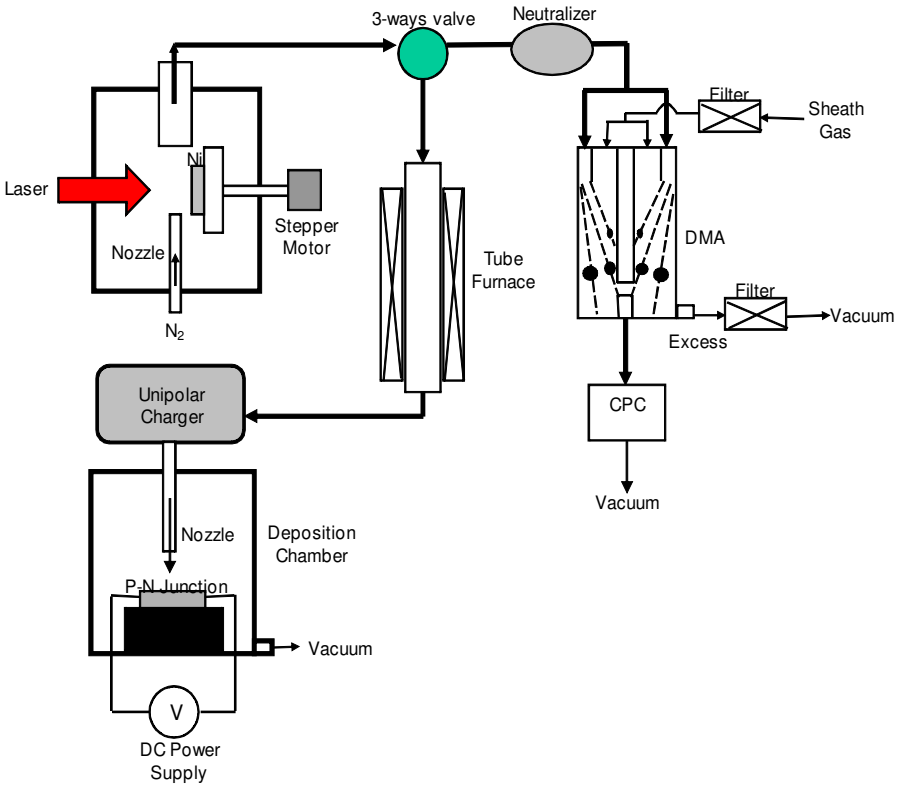

Figure 2.3. Schematic diagram of the experimental system. (DMA is the differential mobility analyzer and CPC is the condensation particles counter)

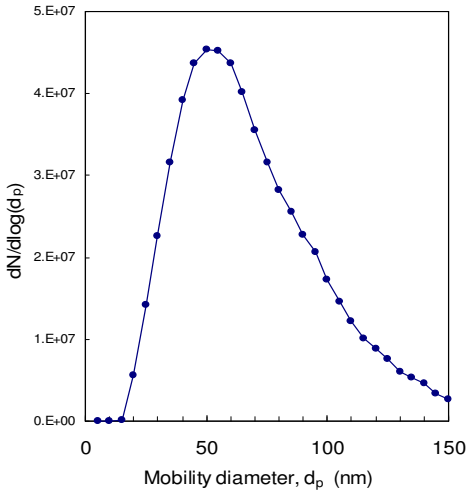

Figure 2.4. Particle size distribution of nickel nanoparticles generated by PLA.

2.1.4 Results and discussion

The Ni particle size distribution generated is shown in Figure 2.4, and indicates a peak size of ~50 nm, and the total number concentration around ~10^8 cm^{-3}. The measured built-in potential of the p-n junction-patterned substrate was about 1.2-1.5 V, which was very close to the calculated result (~1.45 V). This built-in potential was used as the zero-biased electric field in the following experiments.

Figure 2.5 shows SEM images of the p-n junction-patterned substrates, following particle deposition for different reverse bias voltages. When no bias voltage is applied (Figure 2.5a), nickel nanoparticles are homogeneously distributed on both p-type and n-type regions, indicating that the zero-biased electric field generated by the built-in potential was not sufficient to affect the trajectory of the charged particles. However, beginning with a reverse bias of -0.2 V (Figure 2.5b), a higher number concentration of nickel nanoparticles are clearly deposited in the n-type region, indicating that negatively charged particles were being repelled by p-type regions and attracted to the n-type regions. With increasing reverse bias (as shown in Figure 2.5c, d, e), the negatively charged nickel nanoparticles are almost exclusively deposited on the n-type regions and a particle-free zone is clearly observed on p-type regions. Comparing our calculation result of the peak F_e shown in Figure 5f with those SEM images (Figure 2.5a-2.5e), we can see it is sufficient to repel negatively charged particles from the p-type region while the peak F_e is more than 8×10^{-7}N. To quantify the difference in particle deposition level between the p and n-type regions in Fig. 2.5, we define a coverage selectivity of n-type to p-type regions as follows,

$$\text{Coverage selectivity} = \frac{C_N - C_P}{C_N} \times 100\% \qquad (2.7)$$

C_P and C_N are the coverage of particles deposited on the p-type and the n-type regions obtained via digital image processing [30] and presented in Figure 2.5g as a function of bias voltage. Apparently, by about -0.5 V selectivity exceeded 99%. This corroborated with the fact that as the reverse bias was increased, the negative electric field generated on the p-type regions was also increased to sufficiently repel the incoming negatively charged nanoparticles, and resulted in a gradually increase in the coverage selectivity.

It is expected that changing particle polarity to positive will attract particles to the depletion zone of the p-type regions, and repel them from the depletion zones of n-type regions. Figure 2.6 presents SEM images of the positively charged particles deposited on p-n junction substrates. As seen in Figure 2.6a, there was no obvious difference between p- and n-type regions when no bias was applied indicating the built-in potential had no effect on particle deposition. However, as the reverse bias was increased, as shown Figure 2.6b, c, d and e, one can clearly see that particles were preferentially deposited on the negatively charged p-type, and in particular for the higher bias cases (Figure 2.6c, d, e) formed dendrite-like structures due to the presumable attraction of the van der Waals force between deposited particles and incoming particles from the gas phase [31]. We can expect the calculated peak F_e (shown in Figure 2.6f) is increased up to 1.5×10^{-6}N by increasing the reverse bias to –2.5V so that more nanoparticles can be induced to deposit on the p-type region. By Eq. 2.7 we defined the coverage selectivity of p-type to n-type regions in Fig. 2.6,

$$\text{Coverage selectivity} = \frac{C_P - C_N}{C_P} \times 100\% \qquad (2.8)$$

As shown in Figure 2.6g, the coverage selectivity was similar to that observed for the negatively charged particles. However, unlike the formation of the particle-free zone on p-type regions for negatively charged particles (see Figure 2.5d), the particle-free zone for positive particles on n-type regions was not complete even when –0.9 V was applied. Presumably this is because the strength of the positive electric field generated across n-type regions is weaker (~10^5 V/m in the middle of the n-type region at Y=100nm) than that of p-type regions (>10^{10} V/m), and results from the broad width of n-type regions (~30 μm) compared with the relatively narrow width of p-type regions (~1 μm) used in these experiments. The electrostatic force in p-type is more than 1000pN but is only 0.01pN in n-type. This insufficient force in n-type is unable to repel nanoparticles away from that region. Asymmetry of the deposition patterns was observed which we attribute to the role of the bulk convection of the carrier gas affecting the trajectory of the nanoparticles. We estimate the boundary layer thickness to be less than 2 mm under the convective flow conditions of our experiment. As such the gas flow near the substrate is essentially flowing parallel to the surface. The electric force however, is acting perpendicular to the surface. As a result when a particle enters the region of strong attractive field it is also being convected out of that field region by the net gas flow. If the flow velocity is sufficiently high the particle may exit the field region without being deposited or be deposited in a region farther down stream. Effectively this is what is being observed in the asymmetry of our deposits as observed in both Fig 2.5 and 2.6 where the flow direction is from left to right. We have developed a simulation of this

using a full trajectory calculation (Section 2.2). Nevertheless, it is quite clear that by appropriate choice of surface patterning using simple device structures, one may be able to create nanoparticle deposited patterned surfaces. One could imagine the design of PN junction patterns designed to steer particles in a 2-D plain, and/or coupling the electric field effects with thermal fields to have a more precise control of lateral deposition patterns.

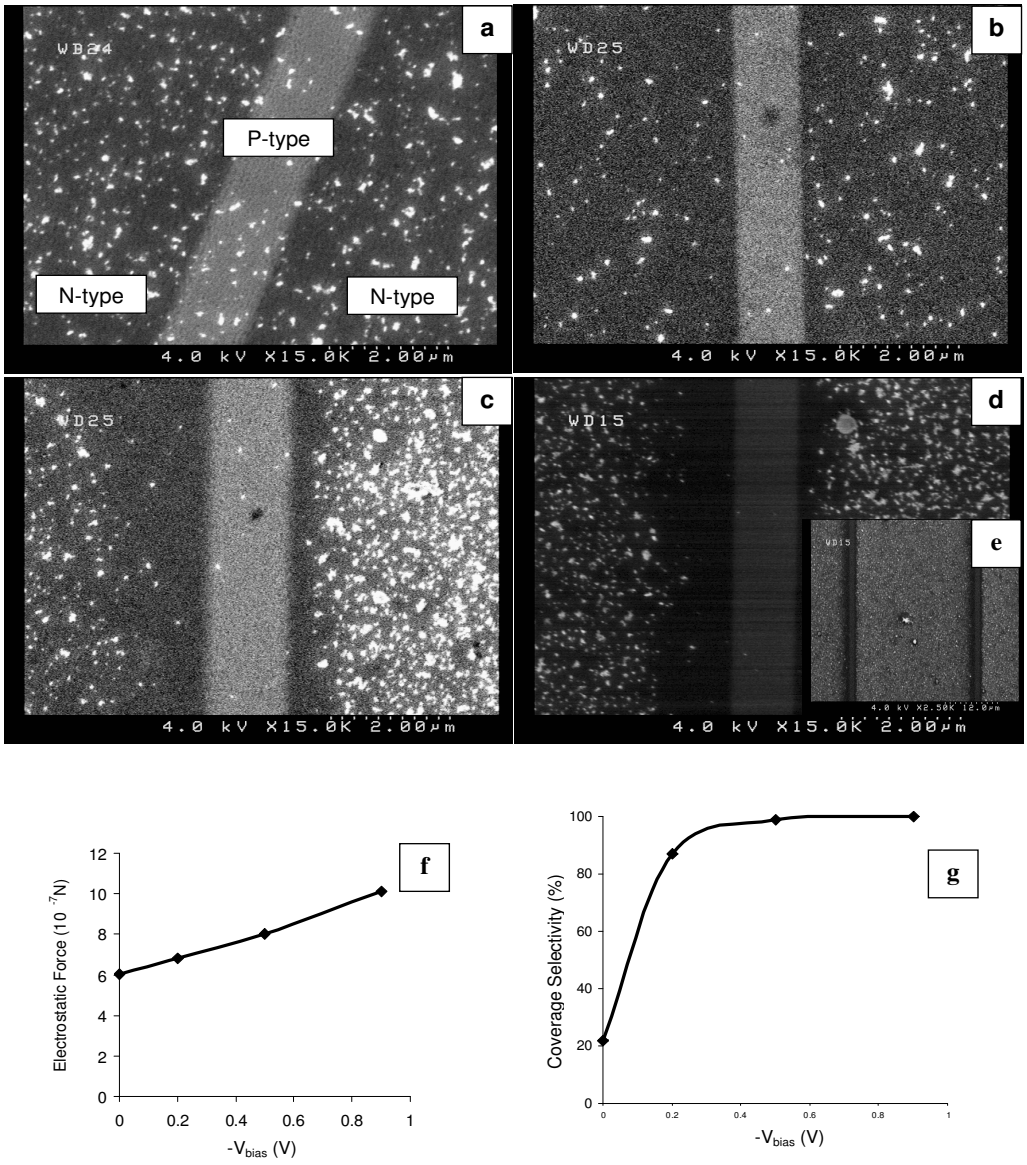

Figure 2.5. SEM images of negatively charged nickel particles deposited on GaAs with the p-n junction under different applied bias voltages. The bright stripes are p-type regions, and the dark stripes are n-type regions. (a) 0 V, (b) –0.2 V, (c) –0.5 V, (d) –0.9 V, (e) Lower resolution SEM image for –0.9 V. (f) Calculated peak electrostatic force, F_e, in the p-type regions, (g) Coverage selectivity of the samples shown in a-d.

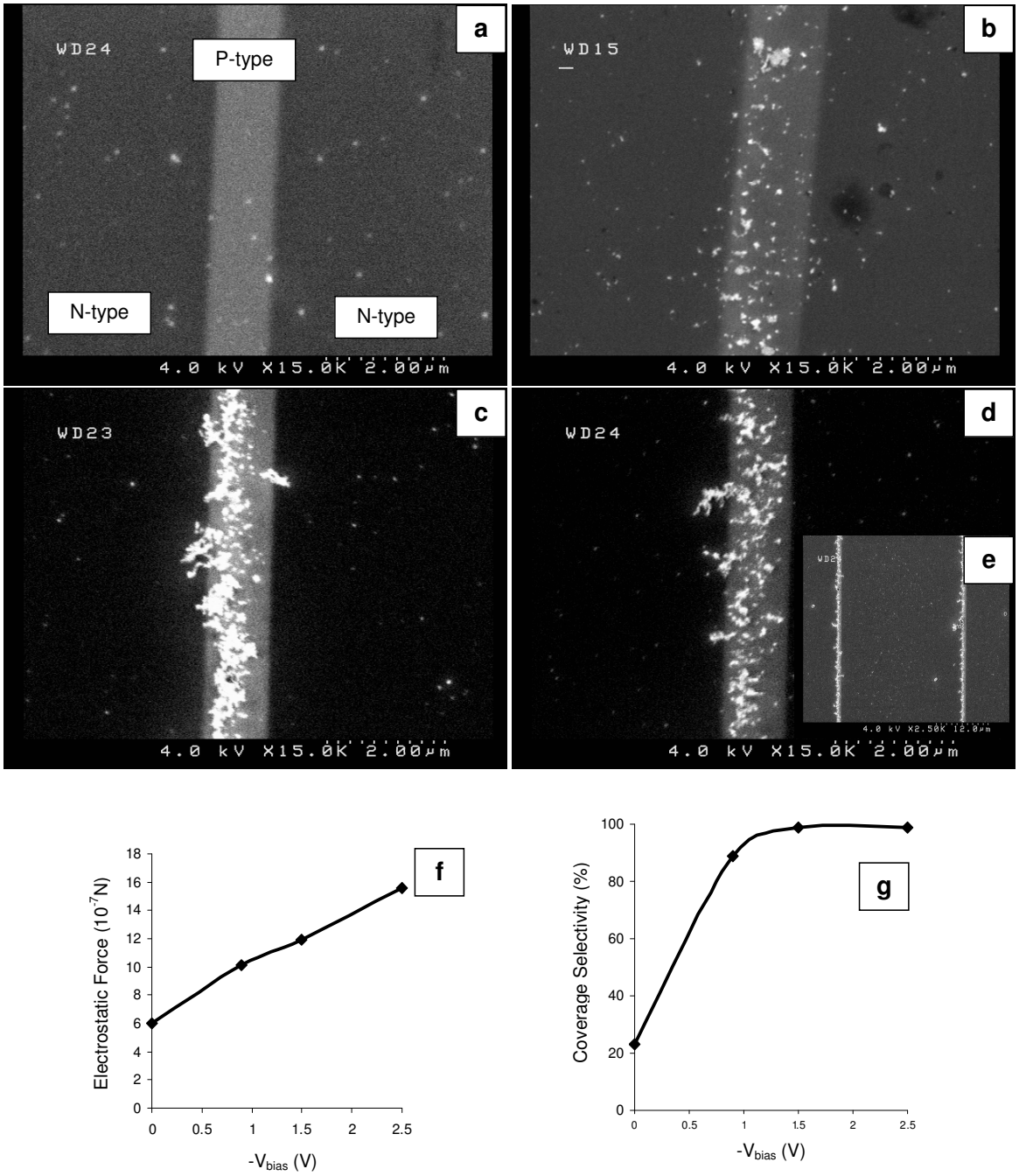

Figure 2.6. SEM images of positively charged nickel particles deposited on GaAs with the p-n junction under different applied bias voltages. The bright stripes in theses figures are p-type regions, and the dark stripes are n-type regions. (a) 0 V, (b) –0.9 V, (c) –1.5 V, (d) –2.5 V, (e) Lower resolution SEM image for –2.5 V. (f) Calculated peak electrostatic force in the p-type regions, (f) Coverage selectivity of the samples shown in a-d.

2.2. Spatial and Size-Resolved Electrostatic-Directed Deposition of Nanoparticles on a Field-Generating Substrate: Theoretical and Experimental Analysis

2.2.1. Introduction

Functional nanoparticles have been widely considered as the building blocks of potential electronic, optoelectronic, and sensing devices [12, 32]. For many applications of nanoparticles, in for example sensors or other electronic devices precise positioning for integration into a working device becomes a considerable challenge. The production of nanoparticles using gas phase methods has the advantage of a clean, continuous process which can be operated at atmospheric conditions without requiring any vacuum environment or solvent medium [12]. An additional advantage is that charge can be readily placed on nanoparticles, which can be used both to conduct size selection or filtration, and to direct deposition through the implementation of electric fields. Electrostatic-directed methods have been used previously with some success [11, 21, 22, 24] and suggest a good strategy to achieve this alignment. In our previous work [11], we directed the deposition of particles using a substrate with lateral and vertical tunable fields. This was achieved by using an array of biased p-n junction patterned substrate to generate a pattern of tunable electric fields, which enabled us to form stable charge patterns on the substrate. Using unipolarly-charged Ni nanoparticles we observed that with sufficient reverse-bias on the p-n junction we could achieve selective deposition on the specific positions on the

substrate. Under the right conditions we achieved very high coverage selectivity (~100 %), and stripe-like deposition patterns of nanoparticles (~500 nm in width)

The success of this work suggested further investigation into the particle size dependence of coverage selectivity, and some consideration of the ultimate resolution that could be achieved in this patterning approach. In this paper we discuss an expanded set of experiments using size segregated (monodisperse) particles. This data forms the basis for the development of a validated Brownian dynamics model.

2.2.2 Experimental

To understand the nature of the deposition process we employ an approach to prepare unipolarly-charged nanoparticles with a very narrow size distribution (~ monodisperse). Figure 2.7a presents a schematic diagram of our experimental system. Silver nanoparticles were synthesized by a spray pyrolysis method [33]. The choice of silver was based on an eventual goal of using these particles for surface plasmon resonance (SPR) bio-sensing devices [6, 7]. A silver nitrate (99+%, Aldrich)/water solution was atomized into droplets (~ 2 μm) and passed to a 850^{o}C flow reactor in nitrogen. At this temperature the metal nitrate is converted to pure silver aerosol with a rather wide particle size distribution [34]. We employ ion-mobility separation of charged particles to create a narrow size cut using a differential mobility analyzer (DMA) [11, 13, 28]. The output of the DMA, which operates like a band-pass filter, provides an output of unipolar charged monodisperse aerosol. The number concentration of monodisperse particles was ~10^5-10^6 cm^{-3} at a flow rate of 1 lpm.

These aerosol particles were then delivered to a second tube-furnace at 600-800 ^{o}C for the purpose of creating spherical nanoparticles. A unipolar charging process [11, 29] was applied to maximize the charges before deposition. These nanoparticles were delivered to the deposition chamber. A more detailed description of the nature of the PN junction substrate can be found in Section 2.1. For particle deposition, the PN junction-patterned substrate was placed in a deposition chamber (9 cm in I.D. and 10 cm in height) with an aerosol feed nozzle (2 mm in I.D.) 1 cm above the substrate.

We prepared three different sized Ag nanoparticles, 30 nm, 50 nm, and 70 nm in diameter, for our studies. The deposition process was the same as we described in Section 2.1. For this part, we chose to work with negatively charged particles. The applied reverse bias voltage across the substrate was varied from 0.1 V to 0.9 V, and the current measured was always less than 0.02 mA. A 2-D electric field is generated from the depletion regions of the p-n junction and is employed to steer the incoming nanoparticles flowing in the boundary layer (details are described in the model section). The nanoparticle deposition pattern was observed with a Hitachi S-4000 field emission scanning electron microscope (SEM) operated at 4-6 kV.

2.2.3 Theoretical model of electrostatic-directed assembly

We have developed a trajectory model based on the force balance on an individual particle approaching the surface of a p-n junction patterned substrate. The flow field is illustrated in Figure 2.7b. For a stagnation point flow, such as we have, the flow carrying the nanoparticles will turn parallel to the substrate, to form the

boundary layer [9, 35]. We analyze the nanoparticle patterns at a location 0.3 cm from the stagnant point (x_f=0.3 cm), where the flow is essentially parallel to the substrat`e. From a mass balance the boundary layer integrated velocity parallel to the substrate can be evaluated.

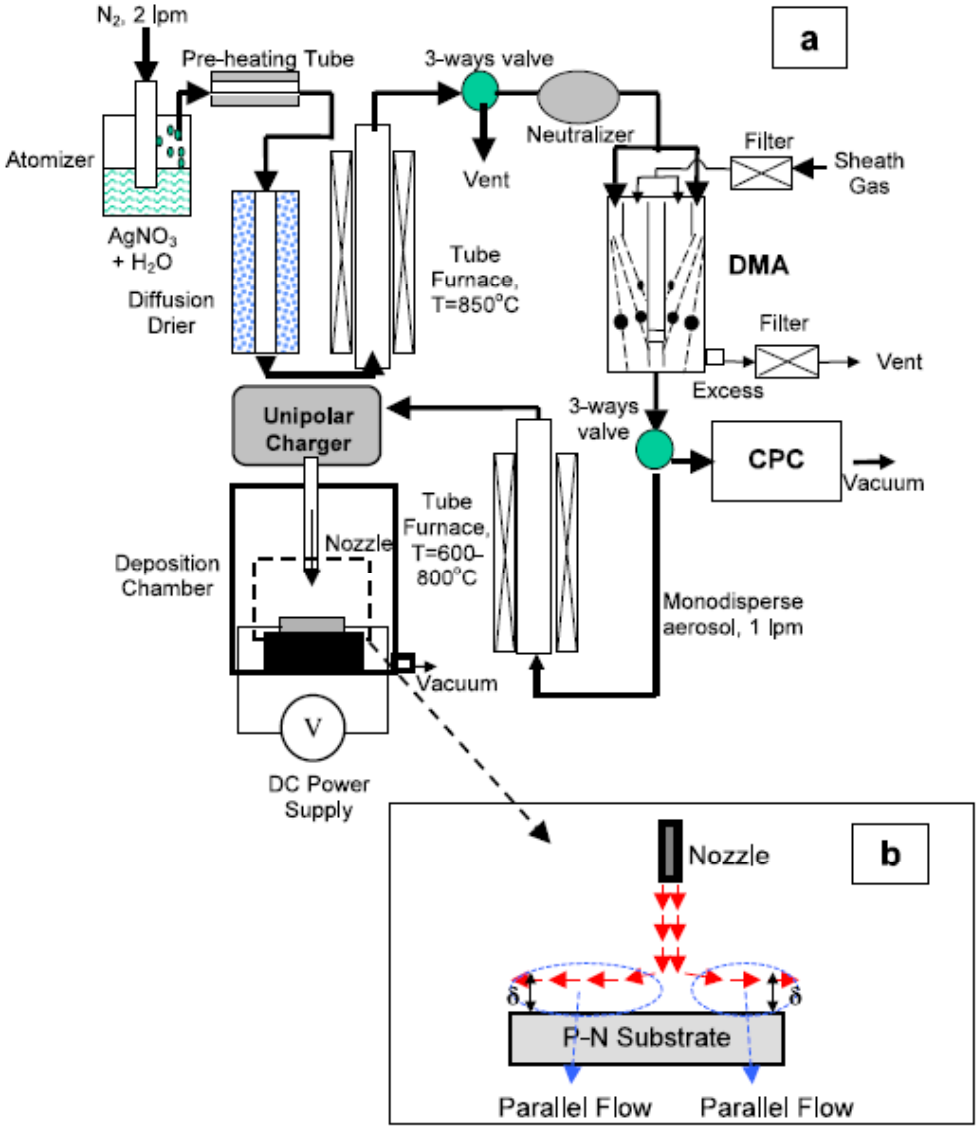

Figure 2.7. (a) Schematic of the experimental system. (DMA: differential mobility analyzer; CPC: condensation particle counter). (b) Flow field above a p-n junction patterned surface. δ represents the thickness of boundary layer.

$$Q = (\pi x_f) \times \delta \times U \qquad (2.9)$$

Here, Q is the flow rate of carrier gas (~1 Lpm), and U is the free stream velocity. For a stagnation point flow the boundary layer thickness δ can be estimated as [35],

$$\delta = \frac{5 x_f}{\sqrt{\frac{\rho_g U x_f}{\mu}}} \qquad (2.10)$$

Here, ρ_g is the density of N_2 carrier gas, and μ is its viscosity. Using typical values yields δ ~1 mm. For a stagnation point flow the convective flow velocity parallel to the substrate can be expressed as a function of height Y_f above the substrate as

$$v_g = U \sin(\frac{\pi Y_f}{2\delta}) \qquad . \qquad (2.11)$$

The deposition process of nanoparticles can be thought to involve two limiting regimes [9]. In regime 1 the weak interaction between the incoming particle and the substrate means that particle motion is governed by convective and Brownian motion. In regime 2 the particles are sufficiently close to the substrate, such that the interaction between an incoming nanoparticle and the substrate strongly influences the particle trajectory [9, 11]. The net external force acting on a particle, $\vec{F}_{ext}$, is given by Eq. 2.6.

For our experimental conditions, nearly all particles are singly charged as they exit the mobility classifier, therefore n=1 [17, 36]. For the electric field, $\vec{E}$, we first solve the Laplacian equation $\nabla^2 V = 0$ [37] for the electrical potential distribution, V(X,Y),

near the substrate. Due to the linear nature of the substrate patterning, we solve the Laplacian equation in 2D, with the following boundary conditions.

$$V\left(-\frac{L_1}{2},Y\right)=V\left(\frac{L_1}{2},Y\right) \quad \text{..... (2.12a)}$$

$$\left.\frac{\partial V}{\partial X}\right|_{X=-\frac{L_1}{2}}=\left.\frac{\partial V}{\partial X}\right|_{X=\frac{L_1}{2}} \quad \text{..... (2.12b)}$$

$$V(X,0)=V_s(X) \quad \text{..... (2.12c)}$$

$$-\left.\frac{\partial V}{\partial Y}\right|_{Y=H}=E_H \quad \text{..... (2.12d)}$$

,where the X-coordinate is the direction parallel to the substrate surface and normal to the P-stripes, the Y-coordinate is normal to the substrate surface, L_1 is the special period of the pn junction array, i.e. the sum of the widths of the P-type and the width of the N-type regions. $V_s(X)$ is the surface potential across the p-n junction, and E_H the electric field strength at the position H above the substrate. Equation 2.12(a) and 2.12(b) specify the periodic boundary conditions in the X direction, Equation 2.12(c) specifies the potential on the PN substrate, and Equation 2.12(d) specifies that the E-field beyond a vertical distance H from the substrate be uniform. We employ a simplified model for the potential $V_s(X)$ on the substrate surface, assuming the abrupt junction model and step-wise charge distributions for the depletion region. Based on these assumption, the lateral variation of $V_s(X)$ can be written explicitly as shown in Figure 8a, where $x_2=L_p/2+\Delta w_n$, $x_1=L_p/2-\Delta w_p$. ($-V_{bias}$) is the reverse bias voltage applied across the pn junction. N_a is the ionized acceptor concentration in the P-type

region (~10^{19} cm^{-3}), and N_d is the ionized donor concentration in the N-type region (~10^{18} cm^{-3}), Δw_n and Δw_p are the widths of the depletion zone in N-type and P- type regions, respectively [11], e is the unit charge (1.6x10^{-19} C), ε_s, is the dielectric constant of GaAs (13.1), and ε_0 is the permittivity of free space. The analytical solution of the electrostatic potential distribution for the boundary conditions described above is the following.

$$V(X,Y) = K_1 + \frac{4e}{\varepsilon_0 \varepsilon_s L_1} \sum_{N=1} (N_a \sin(k_n x_1) + N_d \sin(k_n x_2) - (N_a + N_d) \sin(\frac{k_n L_p}{2})) \frac{\cos(k_n X)}{k_n^3} e^{-k_n Y} \quad (2.13)$$

$$K_1 = \frac{e(N_a \Delta w_p^3 + N_d \Delta w_n^3)}{3\varepsilon_0 \varepsilon_s L_1} + (-V_{bias})(1 - \frac{L_p}{L_1}) \ldots\ldots\ldots\ldots\ldots\ldots\ldots\ldots \quad (2.14)$$

Where, $k_n = 2N\pi/L_1$, The corresponding electric field components E_x and E_y are:

$$E_x = -\frac{dV}{dX} \ldots\ldots \quad (2.15)$$

$$E_y = -\frac{dV}{dY} \ldots\ldots \quad (2.16)$$

which are linear in ($-V_{bias}$). In addition to the applied electrical force, we also consider the image and van der Waals forces in Eq. 2.6 as given by Eq 2.4 and 2.5. [9]

By combining the effects of the external forces, drag, convective flow, and Brownian motion, we can obtain analytic solutions for the particle trajectories by integrating the Langevin equation [8, 10]. The analytical solutions of the velocity and the displacement of a particle in the X-direction during a characteristic time step, $\Delta t = t_N - t_{N-1}$ are given by

$$v_{x,N} = v_{x,_{N-1}} e^{-\beta\Delta t} + \frac{F_{x,N-1}}{m_p \beta}(1 - e^{-\beta\Delta t}) + B_{1,x} \qquad (2.17)$$

$$x_N = x_{N-1} + \frac{1}{\beta}(v_{x,N} + v_{x,_{N-1}} - \frac{2F_{x,N-1}}{m_p \beta}) \times (\frac{1 - e^{-\beta\Delta t}}{1 + e^{-\beta\Delta t}}) + \frac{F_{x,N-1}}{m_p \beta}\Delta t + v_g \Delta t + B_{2,x} \qquad (2.18)$$

We can use similar forms to describe the motion in y and z direction except that v_g is assumed to be zero in both y and z direction, and F_i and F_{vdw}, which depend only depend on the vertical separation distance, are added to the component of the force acting in the y direction. In Eq's (2.17) and (2.18) B_1 and B_2 are random functions of time used to express Brownian motion of a particle, both of which follow a Gaussian distribution, with a mean value of zero. The mean-square values of B_1 and B_2 are expressed in the following:

$$< B_{1,x}{}^2 >= \frac{kT}{m_p}(1 - e^{-2\beta\Delta t}) \qquad (2.19)$$

$$< B_{2,x}{}^2 >= \frac{2kT}{m_p \beta^2}[\beta\Delta t - 2(\frac{1 - e^{-\beta\Delta t}}{1 + e^{-\beta\Delta t}})] \qquad (2.20)$$

Here, k is the Boltzmann constant, T is the temperature, m_p is the mass of a particle, β is the friction constant ($\beta = \frac{3\pi\mu d}{m_p C_c}$), and β^{-1} represents t_r, relaxation time of a particle. N is the step number, C_c is the slip correction factor of a particle ($C_c = 1 + \frac{\lambda}{d}[2.34 + 1.05\exp(-0.39\frac{d}{\lambda})]$) [14], λ is the gas mean free path, and d is the particle diameter. For the size range we consider, $C_c \propto\sim d^{-1}$.

To describe the effects of diffusion, the diffusion force is also calculated from [38].

$$F_{diff} = \left(\frac{6\pi\mu dkT}{C_c \Delta t}\right)^{0.5} \qquad (2.21)$$

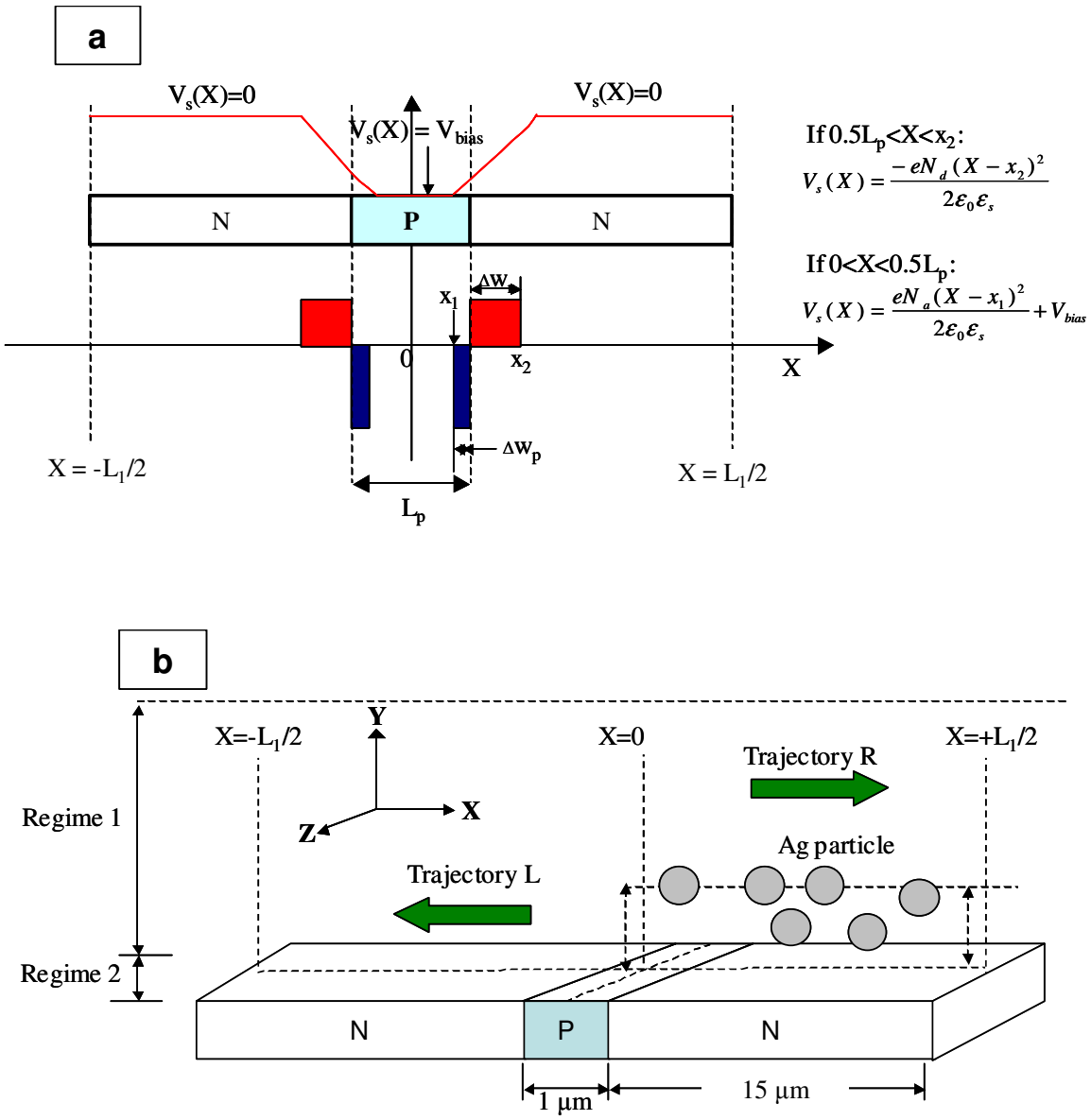

Figure 2.8: (a) Description of the surface potential, V_s, of a reverse-biased p-n junction. (b) Description of our trajectory model. 2 pairs of p-n junctions are located in the specific position of a control volume with a periodic boundaries between X=-L_1/2 and X=+L_1/2.The length of N-type region is 30 µm, and the length of P-type region is 1 µm. The initial position of particles for initialization of trajectories is Y<=10 µm, and 0<X<L_1/2. Regime1 is at Y> 200nm, and Regime 2 is at 0.5d<Y<200nm. d= particle diameter.

2.2.4 Simulation methodology

In our model, we focus on the incoming particle-substrate interaction, and the resulting coverage selectivity of nanoparticles deposited on the patterned substrate. Figure 2.8b is a schematic diagram of our trajectory model in a control volume. In the X coordinate, a pair of PN junctions bound the P-stripe, and the lateral extent corresponds to one period of our PN-array [11]. We neglect the movement in the Z coordinate because the length of the P-stripe is orders of magnitude larger than the width of the charge depletion zone along the X-direction. Along the (vertical) Y coordinate, we define the surface of the substrate as Y=0, and set an upper boundary limit of 5 mm. For the theoretical analysis, we are interested in the effect of the particle size (d), electric field intensity (E), and the convective flow (v_g) on coverage selectivity. We explored the role of three parameters d, $-V_{bias}$, and U, in our simulations.

The boundary between regimes 1 and 2 is selected to be at Y=200 nm, beyond this the electrostatic interaction between an incoming particle and the substrate is very small, F_{ext}<1 pN. To maintain calculation accuracy, while reducing the required calculation time, we chose different simulation time steps, Δt for regime 1 and 2, and for the different particle sizes. In regime 1, Δt was chosen as less than or equal to the time required for a particle to travel one mean free-path. In regime 2, the particles are sufficiently close to the substrate that small effects of the choice of time step can lead to changes in the computed lateral location of deposition to the surface, so that much smaller time steps were used in this region. Because the electrostatic force varies

significantly with height and lateral location relative to the PN junction, we chose time steps in regime 2 such that particles travel a distance no greater than the p-region of the depletion zone, Δw_p (~5 nm), in one time step, as calculated using the electrophoretic velocity, v_e. For a 30 nm sized particle, the required time to travel Δw_p is ~10 ns for a field, E_s ~10^6 V/m. The time steps are summarized in Table 1.

Regime/Diameter	<30 nm	30 nm	50 nm	70 nm
1	2.5 ns	400 ns	400 ns	400 ns
2	0.25 ns	10 ns	10 ns	10 ns

Table 2.1: Simulation time step vs. particle size in the weak interaction regime (1) and strong interaction regime (2).

The starting height of each particle trajectory was at Y<=10 μm, which turned out to be a maximum distance over which a particle would ever make it to the surface in the simulation volume considered. We began with randomly distributed particles over a region 15.5 μm in length along the X direction, spanning a PN junction. Our goal is to produce a one-dimensional simulation of the variation of the coverage across both P-type and N-type regions. To reduce the complexity and calculation time, we did not evaluate the forces in the Z-direction, i. e. parallel to the P-stripes. In the defined control volume with a periodic boundary condition in X-direction, we considered particles convected by gas flow in two different directions along X: Trajectory L is from the right to the left, and Trajectory R is from the left to the right. Each trajectory calculation ends when the particle impacts the substrate.

In order to obtain reasonable statistics, we used a large number of trajectories, 50000 for both the L and R cases. The final positions of the deposited particles were recorded as 1-D simulated deposition patterns for trajectories of type L and R.

2.2.4 Comparison of simulation with experimental results

(1) Effect of the electric field

Figure 2.9 shows SEM images of PN junction patterned substrates following particle deposition for both the smallest and largest diameter particles we investigated, under various reverse bias voltages. In our experiments, all Ag particles were negatively charged in the gas phase so that we see enhanced deposition in the N-type region under the influence of the electric field, as expected. Generally, the Ag nanoparticles were homogeneously distributed into both the N-type and P-type regions at low bias voltages, $(-V_{bias})$ = 0.1V (Fig. 2.9A). With increasing reverse bias voltage, Ag particle deposition is enhanced in the N-type region over the P-type region (Figure 2.9B-C). Significant particle-free zones are observed to either side of the P-type region (we discuss the asymmetry below) when $(-V_{bias})$ = 0.9 V (Figure 2.9D). In our previous study [11], we observed analogous effects of the electric field on charged Ni nanoparticles. We use SEM images like those of Fig. 2.9 to determine the measured coverage selectivity for each particle size as a function of reverse bias voltage. The results are plotted as solid triangles in Figure 2.10.

We next performed simulations, choosing similar parameters of reverse bias voltage, particle size, convective flow velocity, temperature and pressure to those used in the experiments. We see that, in qualitative agreement with experiment, the simulated coverage selectively (shown by the solid curves marked with squares) increases with increasing bias voltage for all three particle sizes, and that coverage selectivities very close to 100 % are indeed predicted by the simulation at the highest bias voltages. In the simulation, this trend results from how the dominant forces act on the particles, mainly electrostatic, diffusion, and drag forces. However, our simulation predicts a coverage selectivity which initially increases with bias voltage at a rate ~ 3 times faster than observed experimentally.

The discrepancy between experiment and the simulations can be understood, at least qualitatively, if the potential drop across the surface of the PN junction is reduced from that within the bulk. In fact, previous direct measurements of the surface potential across a Si PN junction using scanning x-ray photoemission microscopy showed just such an effect [39]. Physically, at least in part of this comes from the effect of electronically active surface states, which result in near-surface band bending. In principle the observed reduction might be used to calculate the density of surface states. In practice, however, the flux of ions to the surface drives the junction further from equilibrium, making such a calculation difficult. To account for this reduction we repeat the simulations, scaling the surface potential difference by an empirically determined factor of γ =0.3. This produces good agreement between the simulation results (dashed lines marked by diamond points) and experimental data, as seen in Fig. 2.10, for all three particle diameters studied.

(1) 30 nm

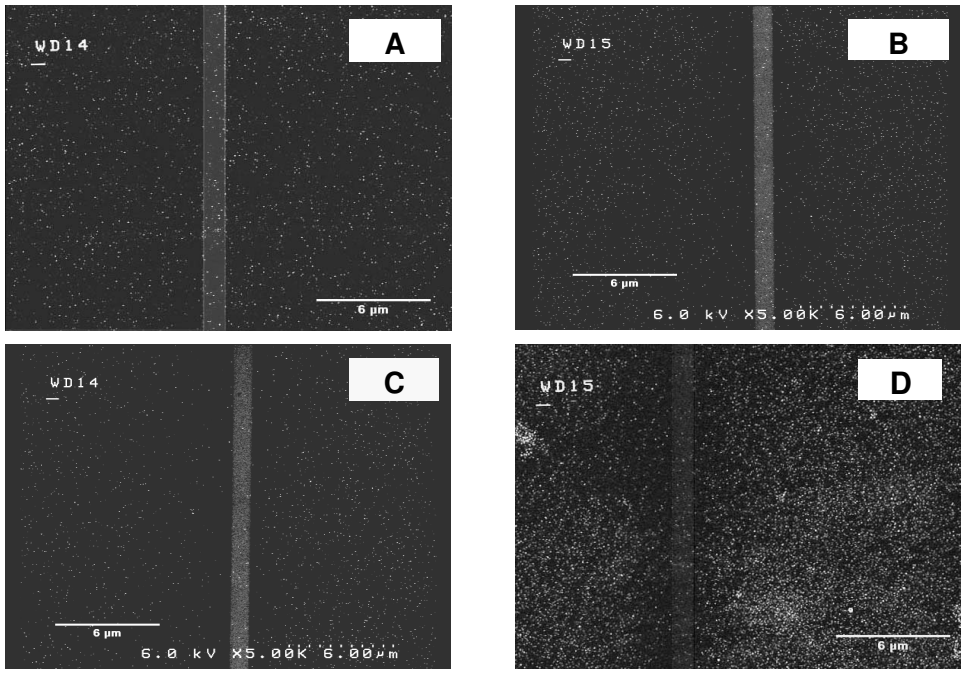
WD14
A
6 µm
WD15
B
6 µm
6.0 kV X5.00K 6.00µm
WD14
C
6 µm
6.0 kV X5.00K 6.00µm
WD15
D
6 µm

(2) 50 nm

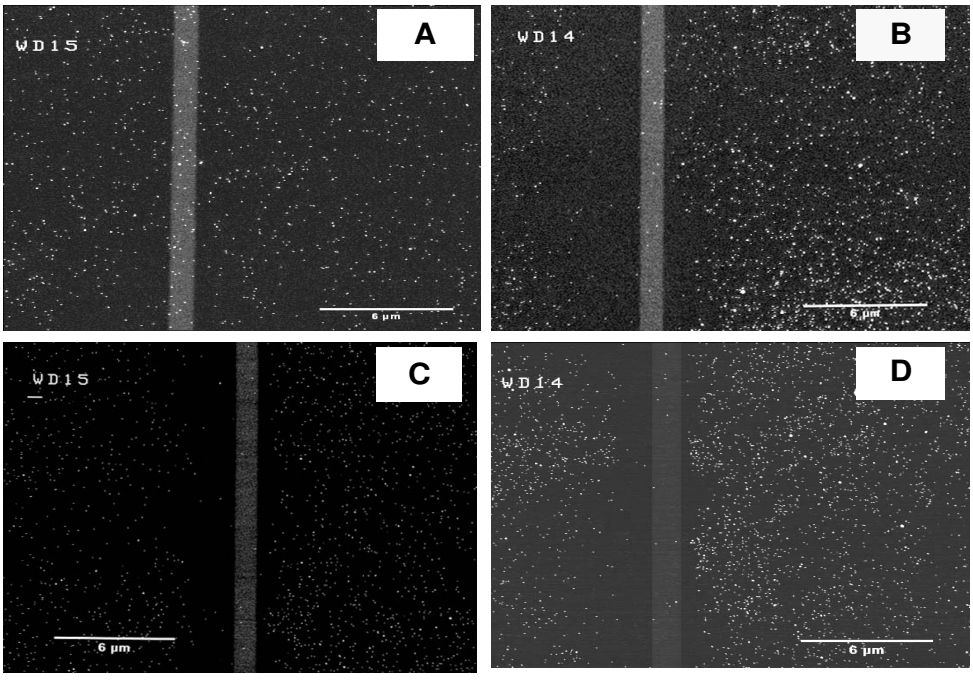
WD15
A
6 µm
WD14
B
6 µm
WD15
C
6 µm
WD14
D
6 µm

(3) 70 nm

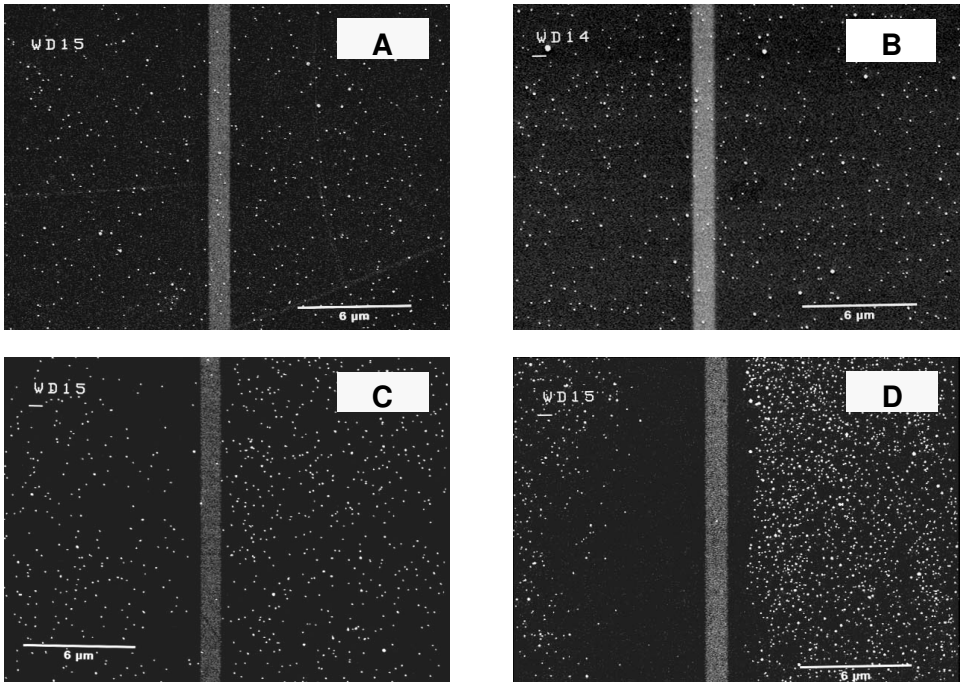

Figure 2.9: SEM images of Ag nanoparticle deposition patterns. Three different size particles, 30 nm 50 nm, and 70 nm, at four different applied bias conditions. A: -0.1 V; B:-0.5 V; C: -0.6 V; D: -0.9 V. Scale bar: 6 µm.

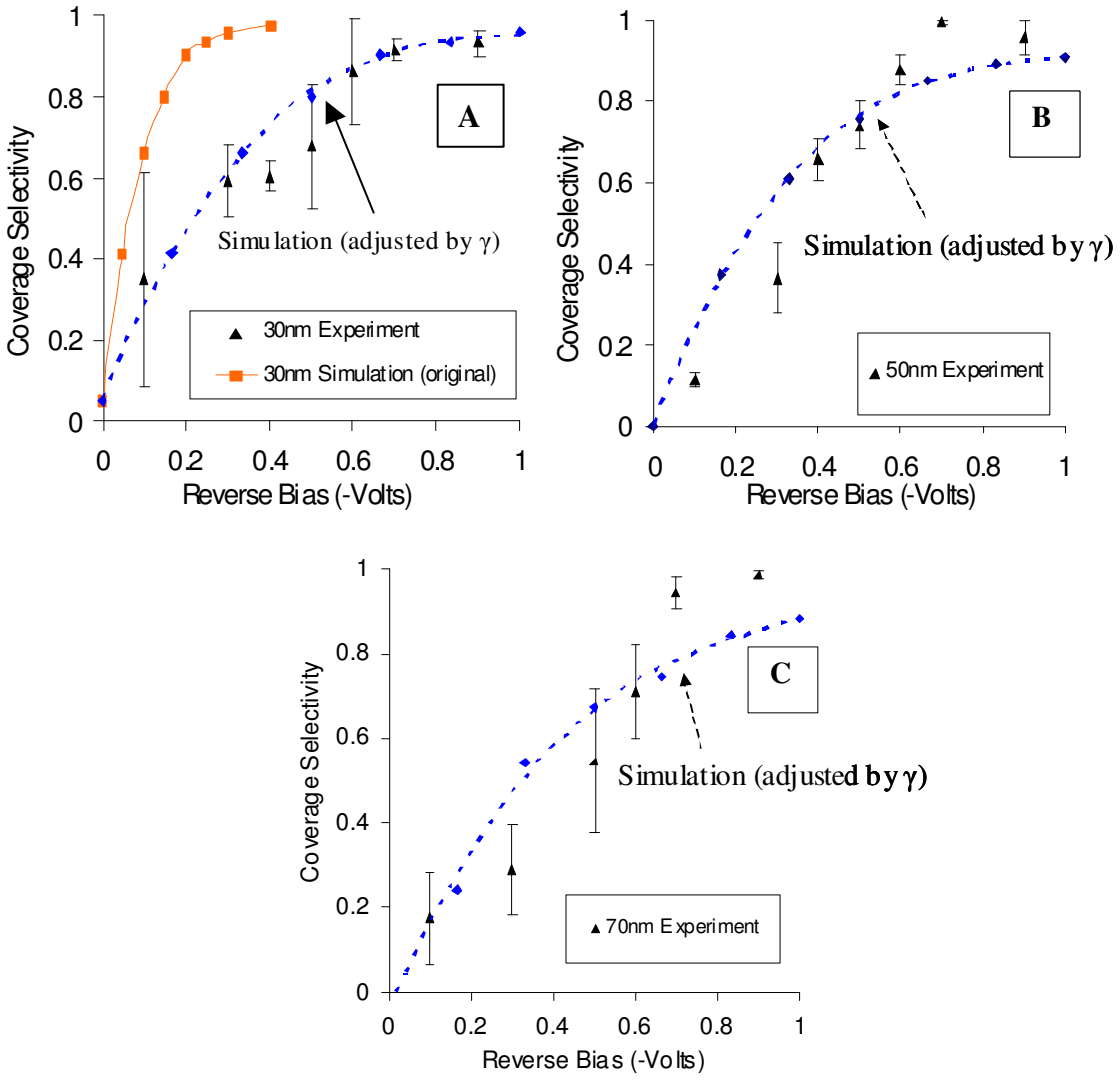

Figure 2.10: Coverage Selectivity vs. various reverse bias voltages. (A) 30 nm particles; (B) 50 nm particles; (C) 70 nm particles. Triangles: experimental data; Squares: simulation data; Diamonds: simulation data fitted by a factor, γ; Dash curve: fitted curve of the simulation data (diamonds).

(2) The effect of the convective flow

The SEM images recorded at higher bias, where the selectivity is high also show a clear asymmetry in the lateral extent of the particle free zone. This asymmetry can be understood as due to the direction of convective flow; in Fig. 2.9d is the flow is evidently from right to left. Figure 2.11 demonstrates this effect, for flows along this direction at a series of flow velocities. Fig. 2.11a shows a simulated trajectory for a singly negatively charged 50 nm diameter particle across a P-type region in the absence of Brownian motion. The particle is initially attracted by the N-type depletion zone (position 1), but does not quite reach the substrate. Rather it continues above the P-type region, where the ionized acceptors electrically repel it, deflecting it upward as it crosses out of that region (position 2). After leaving the P-type region, this particle is deflected downward by the attractive force from the ionized donors in the N-type depletion zone on the left side of the second junction (position 3). The heights of the "lift-up" and "drag-down" parts of the trajectory are determined by the flight time of a particle across the P-N junction and are inversely proportional to the convective flow velocity. As such the lift-up and drag-down distance increases when the convective flow velocity is decreased. Simulations of single particle trajectories for increasing flow velocities are presented in Figure 2.11b. Without convective flow (U=0), the particle travels nearly straight downward to the substrate with a slight lateral deflection due to the horizontal field component E_x. For the lower flow velocities illustrated, U=0.5, 1, 2 m/s, the particle reaches the surface before entering the p-n junction; the lateral distance from the starting point to place of deposition is 1.5 μm, 2.4 μm and 3.6 μm respectively. On the other hand, particle "lift-up" and

"drag-down" are observed for the larger two velocities, U=5, 10 m/s. Decreasing U from 10 m/s to 5 m/s, causes the lift-up distance to increased from ~0.2 μm to ~0.5 μm, and the drag-down distance to increase from ~0.03 μm to ~0.04 μm, i.e. the lift-up height is at approximately an order of magnitude larger than the drag-down distance, resulting in a net lift-up process when a particle crosses a p-n junction. Because the dopant concentration in the N-type region is lower than in the P-type region, the attractive force is weaker than the repulsive force [11]. As such, particles which cross the PN junction are convected farther downstream before they are deposited. Due to the Y-directed electric field, and X-directed convective flow, it is difficult to avoid asymmetry in the deposition pattern. One possible way to reduce this would be to more closely approximate a stagnation point by having multiple particle inlet jets (micromachined) to minimize the X-component of the flow and have a flow that is more perpendicular to the substrate.

The convective flow, in addition to creating asymmetry in the deposit as discussed above might be expected to affect coverage selectivity. To evaluate its effect we carry out simulations at variable gas velocity, v_g, while F_{diff} and F_e are kept constant. Figure 2.12 presents the simulated coverage selectivity as a function of flow velocity for three different experimental conditions; 30 nm particles at V_{bias}= -0.9 V and -0.5 V respectively, and coverage selectivity for 70 nm particles at V_{bias} = -0.5 V. The results indicate that reducing the convective flow velocity only slightly enhances the coverage selectivity. Given this weak dependence, the convective flow velocity is neglected in the non-dimensional analysis to be presented later in the paper.

(3) The effect of particle size

Figure 2.13 compares the measured and simulated coverage selectivity we obtain for three different applied reverse biases, as a function of particle diameters. The solid symbols show the experimentally determined values and the solid lines are the simulation results. While the simulation predicts that the coverage selectivity should decrease with increasing particle size, the experiment shows such a trend only for the smallest bias. At V_{bias} = -0.3 V (circular symbols) and V_{bias}= -0.5 V (triangular symbols), the experiment does show an inverse relationship between coverage selectivity and particle size. In contrast, the experiment clearly shows little size dependence or if anything a positive dependence on size, with selectivity of almost 100 % for the 70 nm particle. The effect of particle size on coverage selectivity should reflect the size dependence of the competing forces acting on the particles. We note that the electrostatic force is directional and is independent of particle size. The diffusion force (Eq. 18) has no preferred direction; due to the size effects on the no-slip boundary condition correction factor (C_c), the diffusion force over the range off particles being considered, will have an approximately d^1 dependence. In our model these are the dominant forces, and thus the ratio, F_e/F_{diff} should physically represent the extent of directional motion generated by the electrostatic force over non-directional Brownian motion, and should dominate the coverage selectivity. Thus in our simulations decreasing particle size increases the ratio $F_e/F_{diff,}$ (proportional d^{-1}) and therefore promotes higher coverage selectivity. This intuitive interpretation of the results clearly does not hold at higher bias voltages, where the simulation predicts the same trends to hold as the lower bias cases although with higher selectivity. We defer

the discussion of the discrepancy between simulation and experiment until we develop the non-dimension analysis in the next section.

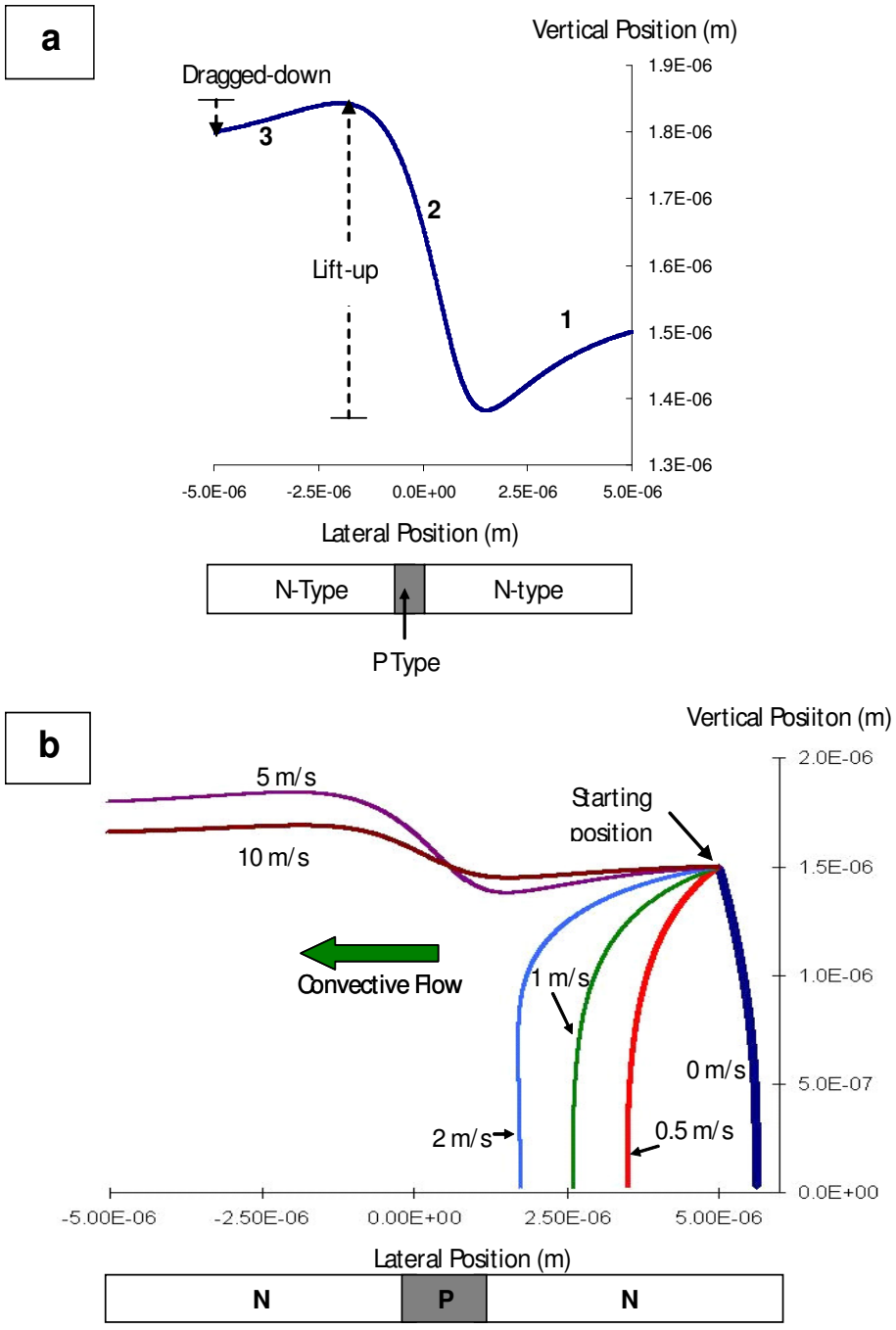

Figure 2.11: Analysis of a single particle trajectory without Brownian motion. (a) Trajectory of a particle at the p-n junction. Curve label 1: The particle was attracted by N-type depletion zone. Curve label 2: If not deposited, the particle is lifted up by the repulsive force from the P-type depletion zone. Curve label 3: When the particle was convected out of the P-type region, it was draged-down by the attractive force from the N-type depletion zone. (b) Particle trajectory at six different convective velocities, *U*: 0, 0.5, 1, 2, 5 and 10 m/s. Particle size: 50 nm. Applied bias voltage is -1 V.

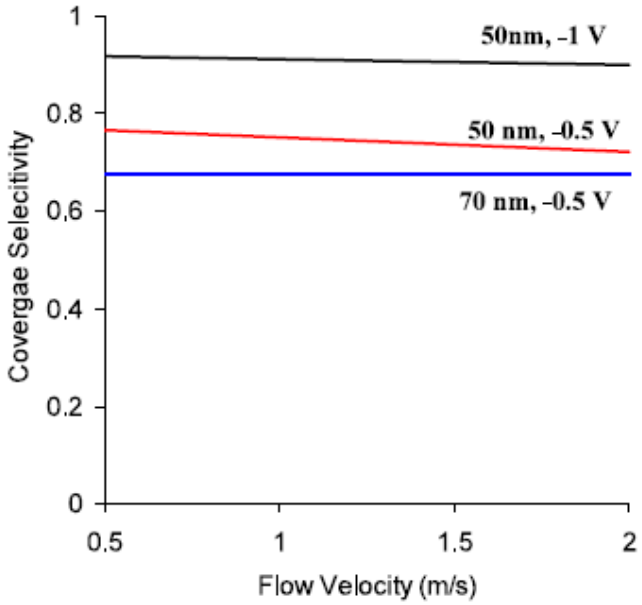

Figure 2.12: Coverage selectivity vs. the convective flow velocity obtained from simulation. U is the free-stream velocity used in the calculation (0.5 m/s to 2 m/s).

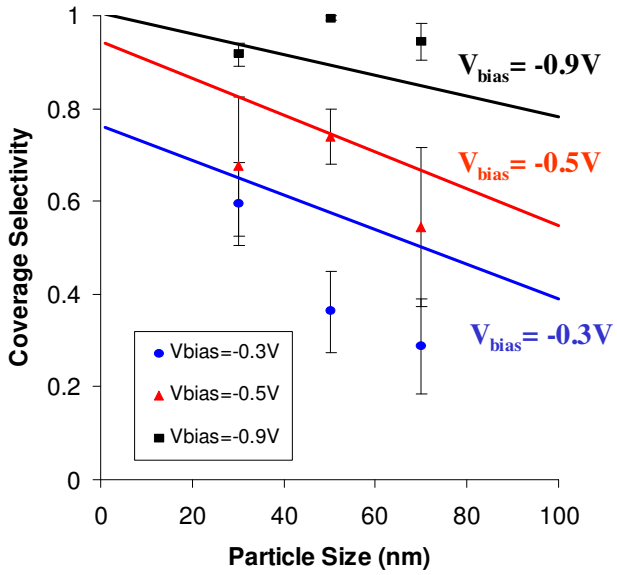

Figure 2.13: Coverage selectivity vs. particle size under three different reverse bias voltages: -0.3 V, –0.5 V, and –0.9 V. Negatively charged particles. Lines represent the simulation of coverage selectivity. The solid points are experimental coverage selectivity: Square: V_{bias} = -0.9 V; Triangle: V_{bias} = -0.5 V; Sphere: V_{bias} = -0.3 V.

(4) *Non-dimensional analysis*

Because of the large number of variables that can affect the coverage selectivity, it is useful to employ a non-dimensional analysis. Clearly of central importance to coverage selectivity, is the competition between the electrostatic force, which is the driving force for a patterned deposit, and the Brownian force, which tends to create a random deposit. Based upon our assignment of the dominant interactions, discussed in the last section, we now introduce a non-dimensional parameter, Ω, which is a ratio of kinetic energy generated by the electrostatic force, W_e, to the diffusion energy, W_{diff}.

$$\Omega = 100 \frac{w_e}{w_{diff}} = \frac{0.5 m_p v_e^2}{1.5 kT} = \frac{(neE_y)^2}{3kT} m_p B^2 \propto (V_{biass})^2 d^3 B^2 \propto V_{bias}^2 d^{-1} \qquad (2.22)$$

Where, v_e is the electrical drift velocity of a particle (v_e=F_e*B), $B = \frac{C_C}{3\pi\mu d}$ is the mobility of a particle ($B \propto\sim d^{-2}$); the factor of 100 is just used for convenience. We evaluate E_y at a fixed position, X=Y=100 nm, to have a simple relationship that E is linear proportional to (-V_{bias}). The dependence of Ω on particle size and applied reverse bias given by Eq. 2.22 shows that $\Omega \propto d^{-1}$ and $\propto (-V_{bias})^2$.

We plot our experimental data (triangle symbols) for coverage selectivity as a function of Ω, shown in Figure 2.14. Also presented are the results of simulations, represented by the solid squares with a logarithmic curve fit (solid line). The clear correlation between coverage selectivity and Ω for the range of particle sizes, applied

voltage, and conditions studied, does indicate that this parameter provides a reasonable non-dimensional parameterization.

The modeling curve obtained by Eq 2.22 agrees well with the experimental data particularly for Ω<5. Hence, one may conclude that the most important factors in this system are the electrostatic force and the diffusion force, which is affected primarily by the applied reverse bias voltage and particle size respectively. On the other hand, when 5<Ω<10, we see a clear deviation between model and experimental results. This was observed earlier for 50 nm and 70 nm particles at high reverse bias conditions ($-V_{bias}$>0.7V, Figure 2.13) where our model under-predicted the experimental coverage selectivity by about 10-15 %. These discrepancies may arise from the additional effects that particles that deposit on the surface can alter the effective field, through image forces, on subsequent particle deposition. We have observed experimentally that at higher deposition conditions that particles on a surface act as attractors to subsequent particle deposition relative to a bare surface.

We begin by evaluating the effect of particles previously deposited to the surface on subsequent deposition. It is well know from experiments on electrostatic particle precipitators, that particles lose their charge when they deposit on a substrate (i.e. no coulomb interaction with the gas-phase particles). As such particle-particle interactions can be calculated from the combination of image and van der Waals forces F_{i_pp} and F_{vdw_pp} given by: [9, 13]

$$F_{i\_pp} = -2\left[\frac{d^2(ne)^2}{8\pi\varepsilon_0(S+d)^3} - \frac{2d^2(S+d)(ne)^2}{\pi\varepsilon_0[4(S+d)^2 - d^2]^2}\right] \qquad (2.23)$$

$$F_{vdw\_pp} = -\frac{32A_H}{3}\frac{(\frac{d}{2})^6}{S^2(S+2d)^2(S+d)^3} \quad (2.24)$$

Here, A_H is the Hamaker constant (4×10^{-19} J), and S is the particle-particle distance. F_{i_pp} is negligible (~<10^{-10} pN when S=90 nm) comparing to the F_e (~0.003 pN when S=90 nm, X=2L_p, and V_{bias} = -0.7 V). Considering F_{vdw_pp}, Eqn. 2.24 indicates that larger sized particles will increase the attractive force to incoming particles. For example, when S is 90 nm, $F_{vdw\ p\_p}$ is 1.5×10^{-4} pN for a 30 nm particle, but increases by a factor of 20 to 3×10^{-3} pN for a 70 nm particle, which is about equivalent to F_e (~0.003 pN). At high coverage selectivity, and high surface coverage the deposited particles in the N-type region can assist the incoming particles to be deposited to enhance this coverage selectivity. This effect should most affect the larger particles. In our studies the discrepancy between experiment and model occurs at the intermediate values of Ω. While we are not in a position to firmly establish this point we believe this is likely because at low values of coverage selectivity (i.e. low Ω the low substrate coverage mitigates the effects of particle-particle forces, while at high values of Ω the coverage selectivity is already so high so as to mask these effects. Thus we only see these effects at the intermediate values of Ω where high coverage density effects of particle-particle interaction can impact the overall coverage selectivity. A more thorough analysis would require a detailed analysis and correlation of particle deposition vs. particle–particle separation distance for various particle sizes, and is beyond the scope of this work. Generally, the minimum coverage selectivity can still be estimated by Ω without taking into account the particle-particle interaction.

We have previously demonstrated that we can obtain selective deposition with positively charged particles [11]. By changing particle polarity, the N-Type region now becomes repulsive. Eqn. 2.22 is still applicable for this case. However to make the geometric adjustment (the width of attractive zone is 1 μm and the width of repulsive zone is 30 μm), we introduce a new dimensionless parameter, Ω_2 (=K_2 Ω, K_2 is a geometry adjusting factor) to evaluate the performance for depositing particles on the P-type region. For polydisperse particles (the peak mobility diameter is 50 nm), K_2 is found to be ~0.4 by fitting the coverage selectivity results [11]. The implication is that one must increase the reverse bias voltage in order to obtain the same Ω.

This analysis indicates that Ω is an effective indicator of process performance. If one desires greater than 80 % coverage selectivity, then Ω should be least 6**.** However, the use of the present form of Ω implies that inertial effects are relatively weak in comparison with electrostatics, drag, and diffusion forces. As such this non-dimensional analysis is limited to higher pressure situations where ballistic deposition is unimportant.

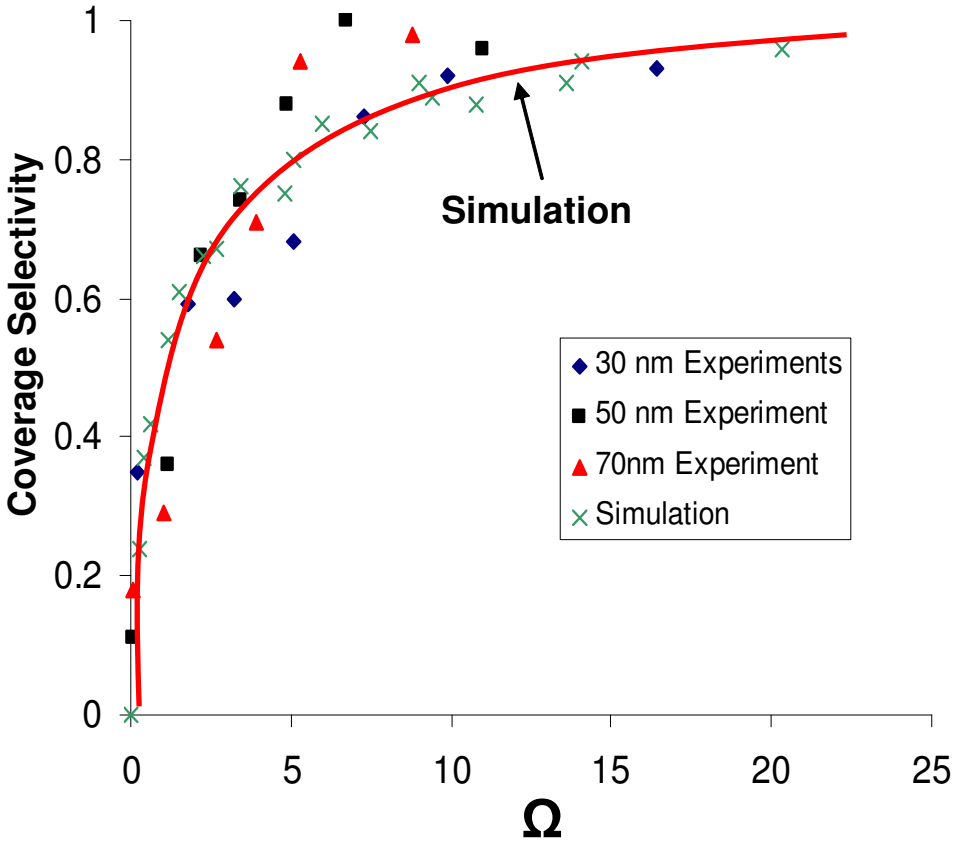

Figure 2.14: Non-dimensional analysis. Coverage selectivity vs. Ω. Diamonds: experimental coverage selectivity of 30 nm particles; Squares: experimental coverage selectivity of 50 nm particles; Triangles: experimental coverage selectivity of 70 nm particles. The simulation curve, obtained from curve fitting of simulation data (crosses).

2.3 Applications in Nanoparticle-Enhanaced Bio-Sensing Devices

2.3.1 Introduction[7]

One of the most promising potential applications in nanotechnology is bio-sensing based on nanoparticle-enhanced spectroscopies. These include detectors with extreme sensitivity for target molecules and biosensor systems having capability to work at very low input power. While most of the experimental investigations have centered on surface enhanced Raman scattering (SERS)[5], there is also considerable interest in understanding and employing nanoparticle enhancement of fluorescence spectroscopy [6, 7]. Passive enhancement of fluorescence, provided by proximity to noble metal nanoparticles is expected to allow the development of highly sensitive biomolecule detectors.

Silver nanoparticles have been considered as a desired component to enhance the labeling signal in bio-sensing[6, 7, 40, 41], and a schematic of the concept is shown in Figure 2.15. Compared with Au nanoparticles, Ag particles have a higher-frequency surface plasmon band and therefore can be employed for analytes requiring a higher frequency of excitation. In addition, the extinction coefficient of the surface plasmon band of Ag nanoparticles is ~ 4 times as large as that of Au nanoparticles [40], and a stronger metal-enhanced fluorescence (MEF) ratio could be expected theoretically.

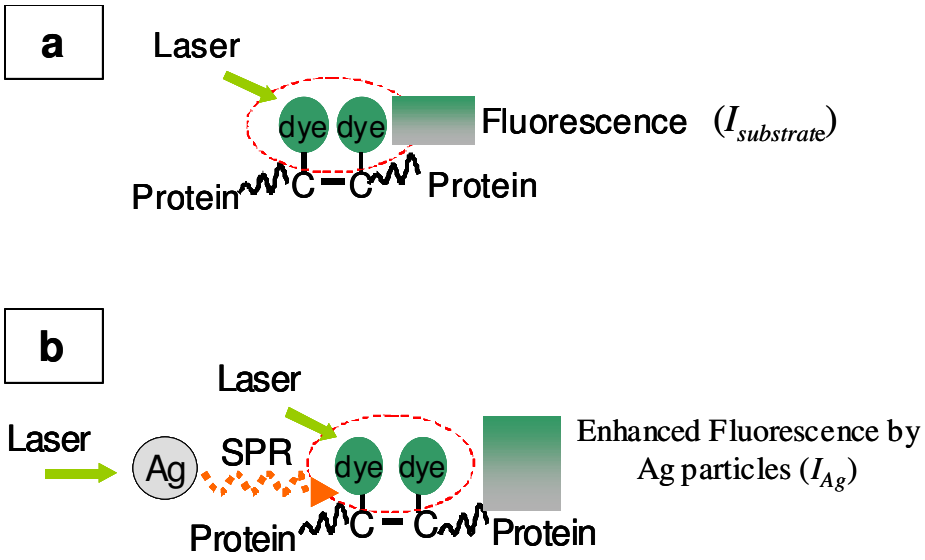

Figure 2.15: Fluorescence-based Bio-sensing. The representative analytes are proteins conjugated with fluorophores (dyes). (a) Fluorescence without using Ag nanoparticles and having a fluorescence intensity of $I_{substrate}$. (b) Fluorescence with Ag nanoparticles and having an enhanced fluorescence intensity of I_{Ag}.

To successfully apply Ag nanoparticles in this bio-labeling process, three conditions are required: (1) high purity; (2) well-controlled particle size; (3) effectively depositing and precisely positioning nanoparticles onto the required region.

The production of silver nanoparticles using the gas phase method has several characteristic advantages to achieve the required conditions described above. First, gas phase production of Ag nanoparticles is a clean, continuous process which can be operated at atmospheric conditions without requiring any vacuum environment or solvent medium [12, 13]. Second, charges can be readily placed on nanoparticles in the gas phase,

which can be used both to conduct size selection. By a gas-phase electrostatic classification, high purity, monodisperse particles with a narrow size distribution can be obtained [13].

2.3.2 Experimental

Figure 2.7 presents a schematic diagram of our experimental system [13]. Briefly, silver nanoparticles were synthesized by a spray pyrolysis method [33]. A silver nitrate (99+%, Aldrich)/water solution was atomized into droplets and passed to a 850°C flow reactor in nitrogen. At this temperature the metal nitrate is converted to pure silver aerosol with a rather wide particle size distribution. We employ ion-mobility separation of charged particles to create a narrow size cut using a differential mobility analyzer (DMA) [11, 13, 42]. The output of the DMA, which operates like a band-pass filter, provides an output of unipolarly-charged monodisperse aerosol ($d_p \pm 0.1 d_p$).

For the MEF measurement[6, 7, 41], we first deposit size-classfied Ag nanoparticles on the SiO_2/Si substrate and then characterize their bio-sensing performance based on fluorescence at the Laboratory for Physical Science, College Park. We coat these nanoparticle-covered substrates with a BSA-biotin spacer layer, whose thickness is 3-4 nm. Next we deposit drops of solution containing both Cy3 and Cy5 fluorophores tagged complementary streptavidin protein. Finally we rinse away fluorophore-tagged protein not bound to the underlying BSA-biotin. Fluorescent images of the sample are collected using a confocal laser scanning microscopy (Zeiss model LSM 410). The samples are maintained wet, i.e., under a thin layer of dilute buffer solution (pH 7.5, 5 mmol/L

solution of mixture of $NaH_2PO_4 \cdot H_2O$ and $Na_2HPO_4 \cdot 7H_2O$). For the Cy3 fluorophore the wavelength of the incident (excitation) light is 514 nm, produced by an Argon laser, and the fluorescent image is collected through a filter which passes wavelengths between 535nm and 575 nm wavelength. For the Cy5 fluorophore the wavelength of incident light is 633nm, produced by a He-Ne laser, and the fluorescent image is collected through a filter which passes 660nm wavelength and above. The details about the sample preparation are described in ref [6, 7, 41] by Corrigan and Kuo et. al.

2.3.3 MEF of size-selected Ag nanoparticles

Figure 2.15a shows an SEM image of 100 nm Ag nanoparticles deposit. Particles are monodisperse and homogeneously distributed on the substrates with an average spacing > 300nm. Figure 2.15b is the MEF image from a sample of Cy5-coated 100 nm Ag nanoparticles. The bright spot represents high fluorescence intensity, which is from the area covering Ag nanoparticles.

We investigated the size-dependent MEF behavior, and the details are described by Kuo et. al. in ref [41]. Quantitative analysis of the fluorescence enhancement for Cy3 and Cy5 fluorophores from the silver nanoparticles is shown in Figure 2.16. Here the coverage corrected enhancement is defined to be $MEF = \frac{I_a - I_B}{I_f - I_B}$, where I_a is the average fluorescent intensity corrected for the area fraction of the surface covered by the silver nanopartilces[43] . I_f is the fluorescent intensity measured from an area covered with a fluorophore/spacer layer with no silver nanoparticles, I_B is the "background"

intensity, measured from an area where neither fluorophore nor silver nanoparticles are present. Figure 2.16 shows the measured nanoparticle diameter dependence. As shown in Fig 2.16, the enhancement initially increases with particle diameter, reaching a maximum of ~23 fold enhancement at d ~ 80 nm for the 514 nm wavelength (Cy3) excitation. For excitation at a wavelength of 633 nm (Cy5), the maximum enhancement of ~ 22 is measured at a slightly larger diameter, ~120 nm, as seen in Figure 2.16. This result indicates that the particle size and the type of chosen fluorophores can tune the MEF, and a red-shift is expected by choosing larger sized silver nanoparticles.

2.4 Conclusion

We have demonstrated a new electrostatic-directed method to position metal nanoparticles deposited from the gas-phase on a p-n junction-patterned substrate. Unipolarly charged nanoparticles are laterally confined on the substrate from a balance of electrostatic, van der Waals and image forces. This assembly method has an advantage that it employs commonly used substrate architectures for the patterning of an electric field.

A Brownian dynamic simulation has been developed that can semi-quantitatively explain most of the behavior observed experimentally, and can be extended to other geometric and process conditions. A non-dimensional parameter Ω is developed which provides a guide on expected coverage selectivity. The approach

offers the opportunity to create a variety of more sophisticated electric field patterns, which may be used to direct particles with greater precision.

Ag nanoparticle with high MEF have been prepared by the electrostatic classification of particle size from the gas phase. Well-positioned and aligned size-selected Ag nanoparticle patterns have also been achieved by the assistance of electrostatic force. The electrostatic force provides a good strategy to control both the particle size and the quality of particle deposits required for the nanoparticle-based devices.

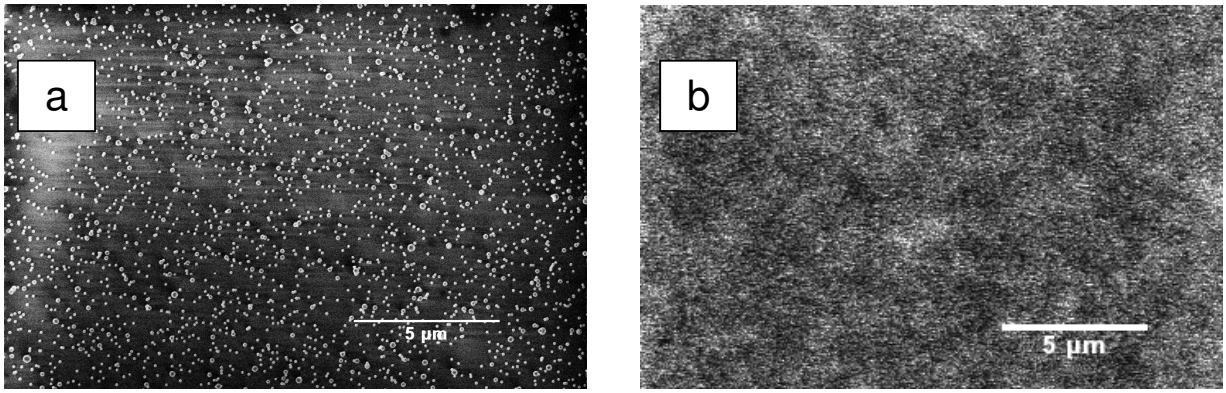

Figure 2.16: (a) SEM images of 100 nm Ag particles. (b) Scanned fluorescence image of 100 nm particles coated with Cy5.

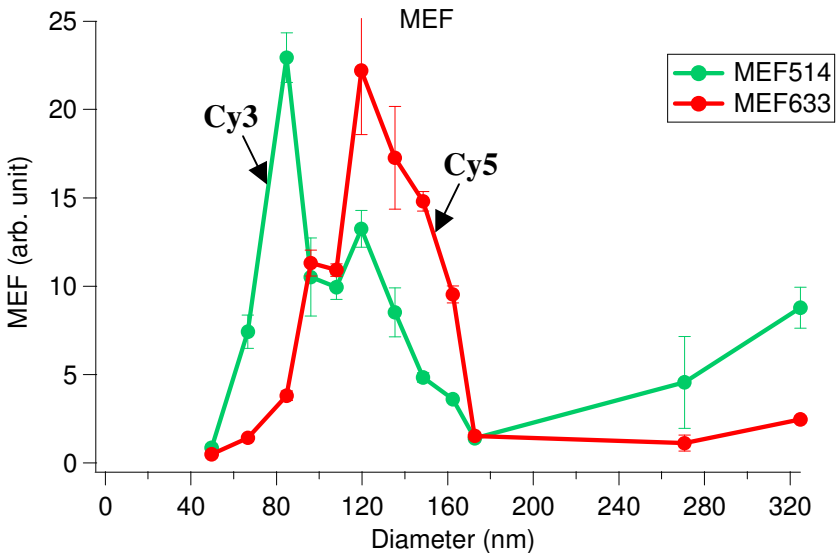

Figure 2.17: MEF v.s Particle Size. Two kinds of fluorophores, Cy3 and Cy5 were used for the test.

Chapter 3

Gas-Phase Ion-Mobility Characterization of Functional Nano-Materials

3.1 Characterization of SAM Functionalized Au Nanoparticles

3.1.1 Introduction

Gold nanoparticles (Au-NP) are widely considered to be useful components in many nanobiological applications in part due to their unique and distinctive surface plasmon resonance band that enhances the sensitivity of bio-sensing processes [2, 5]. Au-NPs can also be readily modified with alkanethiol self-assembled monolayers (SAMs) for precise control of surface chemical and physical properties of Au NPs [44, 45]. The wide range of available terminal functional groups of SAMs enables facile attachment of biological molecules such as proteins, nucleic acids, and carbohydrates. One exemplary application of surface-modified Au nanoparticles is for the diagnosis and treatment of cancers [2, 46]. For such applications, desirable properties of the functional Au nanoparticles include: (1) a high purity, (2) a well-controlled particle size, (3) a well-controlled adsorption/release of materials on/from the surface/interior of nanoparticles.

One of the challenges in the reliable use of these materials, particularly as they relate to any biomedical application, is characterization. This is a particularly challenging problem as it relates both to the physical size of the particle, the size distribution, and the

physical and chemical nature of any coating. Naturally, no individual diagnostic tool can answer all these questions.

In this section we focus on the determination of the surface coverage and strength of binding of alkanethiol SAMs on gold nanoparticles. The approach taken is to apply electrospray (ES) followed by ion-mobility characterization (gas-phase electrophoresis). A gas-phase approach is employed for many of the same reasons that ES-mass spectrometry (ES-MS) approaches are used so extensively in the proteomics research community. It is a clean, continuous process that readily charges the nanoparticles. These charged nanoparticles can in turn be easily size-classified based on their mobility [12, 13]. We present here an approach to electrospray alkyl-thiolated functionalized gold nanoparticles and characterize the size and coating stability of these conjugated Au nanoparticles by differential mobility analysis (DMA). We demonstrate the utility of the method to identify the coating thickness and employ a programmed thermal environment in the gas-phase to determine the binding energy of the thiol monolayers as a function of particle size.

3.1.2. Experimental

Electrospray (ES) of Au nanoparticles from solution is a promising method for generating individual aerosol nanoparticles for DMA. Although the ES of unconjugated Au nanoparticles has very recently been demonstrated [47, 48], ES of clean Au nanoparticles remains challenging, because the presence of salts or surfactants, typically added to stabilize the colloid, can result in the formation of salt particles during ES that interfere

with DMA. Furthermore, for stable cone-jet operation, the solution conductivity must be precisely controlled.

3.1.2.1. Materials

For the preparation of the functionalized Au-NPs, it was necessary to develop protocols to remove, or at least assure ourselves that we understood the role of additives that serve to stabilize the colloid. Commercially available, monodisperse Au colloids (10 nm, 20 nm, 30 nm, and 60 nm, citrate stabilized, Ted Pella Inc.) were used in this work, and 11-mercaptoundecanoic acid (99+%, MUA) and (1-mercapto-11-undecyl)tri(ethyleneglycol) (99+%, PEG) were chosen for the either charged or neutral self-assembled monolayers (SAMs) on Au nanoparticles. Conjugated Au colloids were prepared using 5 times excess the amount of thiol needed to form a full monolayer on the Au colloids as approximated using a surface density of 5 x 10^{14} molecules/cm^2 [49], and total gold colloid surface area based on vendor provided information. After addition of thiol was added to 1 mL aliquots of the as received Au colloids, they were allowed to react for 20 hrs. The Au colloid solution was then centrifuged to separate the colloids from the supernatant that contains excess stabilizer and thiols. The supernatant was then removed, and replaced with an equivalent volume of aqueous ammonia acetate (99.9 %) solution (~2.5 mmol/L, 0.03 S/m). The Au colloids then were easily dispersed by mixing. Additional characterization of the SAM/Au colloid conjugates was performed using FTIR and XPS analysis.

3.1.2.2 FTIR, XPS, and TEM Analysis

Conjugated Au colloids were concentrated by centrifugation, and then dried on commercially available Teflon cards for IR analysis, and indium foil for XPS analysis. Transmission FTIR absorption spectra were measured using a commercially available spectrometer with a cryogenic mercury cadmium telluride detector. Presented FTIR spectra are the result of averaging 128 scans at 4 cm^{-1} resolution. XPS measurements were made on a commercially available spectrometer with monochromatic Al Kα radiation, and an X-ray power of 150 W. High resolution scans were acquired for Au 4f, S 2p and C1s regions in the fixed analyzer transmission mode with pass energy of 40 eV. All FTIR and XPS measurements were performed on freshly prepared samples.

Additionally, Au nanoparticles generated from the ES process were collected on TEM grids with an electrostatic precipitator[13] to enable TEM characterization. Conjugated Au nanoparticles were collected directly from the dried Au colloids onto TEM grids.

3.1.2.3 Electrospray Particle Generation and Differential Mobility Analysis

Figure 3.1 represents a schematic diagram of our experimental system, consisting of an electrospray aerosol generator, a differential mobility analyzer, and a condensation particle counter (CPC). Conductive solutions of Au colloids were placed in the pressure chamber, and then delivered to the nozzle through a capillary (0.025 mm in diameter, 24 cm in length). The liquid flow rate, Q_1, was about 66 nL/min and the flow rate of carrier

gas was 1.2 L/min. To achieve better electrical stability in the ES, the filtered air was mixed with CO_2 (83 % Air and 17 %CO_2) [50]. Operating with an applied voltage of 2-3 kV, the Au colloids were sprayed in a cone-jet mode and converted from highly-charged droplets (thousands of elementary charges), to neutralized particles having a known Boltzmann charge distribution by passing the aerosol stream through a housing containing a α-radioactive Po-210 source. The "neutralized" particles were directly passed to the differential mobility analyzer (DMA) for particle size measurement, and counted with the CPC. The diameter of Au particles, d_p, was characterized by electrical mobility, which is inversely

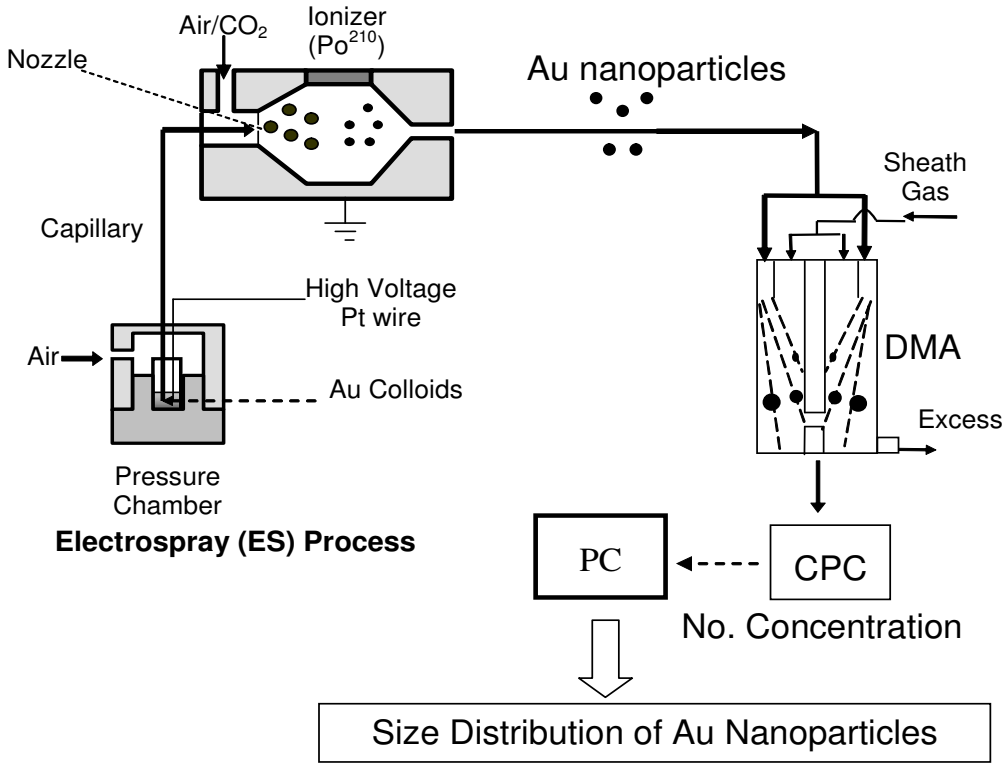

Figure 3.1: Schematic of experimental system, including DMA (differential mobility analyzer), (DMA), and condensation particle counter (CPC).

proportional to the projected areas of the particle. In order to have sufficient resolution and stability in the DMA measurements, its sheath flow of DMA was chosen to be 30 Lpm for the 10-30 nm sized particles, and 10 Lpm for the 60 nm particles. Based on the operating conditions of the DMA, the theoretical FWHM in the size distribution gives us: 10 ± 0.2 nm for 10 nm particles, 20 ± 0.3 nm for 20 nm particles, 30 ± 0.5 nm for 30 nm particles, and 60 ± 3 nm for 60 nm particles. To obtain a precise size distribution, the scanning step size was 0.2 nm, with a scanning rate of 0.01 nm/s. The variation in peak size for each sample was only ±0.2 nm. Because of the stability of DMA measurements, we were able to resolve a change in diameter as small as 0.2 nm [51, 52].

Because we do not directly evaluate the droplet size generated from the ES source we employ a scaling law for estimation purposes. The initial ES droplet size can be evaluated by:

$$D_d = D_{d,0} \times \left(\frac{Q_1 K_0}{Q_0 K_1}\right)^{\frac{1}{3}} \qquad (3.1)$$

where Q_0 is the flow rate, K_0 is the conductivity of the colloidal solution and $D_{d\,0}$ is the estimated droplet size (~378 nm)[50]. In our work the conductivity of Au colloids, K_1, was 0.03 S/m. Hence, the calculated droplet size using this scaling rule is ~200 nm.

3.1.3. Result and Discussion

Our objective is to develop a systematic approach for characterizing SAM-conjugated Au-NPs based on gas-phase mobility classification. We start our work on

unconjugated Au-NPs and then proceed to functionalized Au-NPs. From the change in particle mobility upon SAM Au-NP functionalization, we estimate the surface packing density of SAM molecules on the Au surface. Finally, we estimate the binding energy of alkanethiol molecules on Au-NPs by thermally desorbing alkanethiol molecules from Au-NPs and measuring the corresponding changes in particle mobility. A particular advantage of our approach is that these studies can be conducted on size-selected NPs.

3.1.3.1 Unconjugated Au Nanoparticles

(1) Particle Size Distribution and the Effect of Salt Residues

Figure 3.2a presents size distributions obtained by electrospraying as-received citrate stabilized Au nanoparticle samples of nominal diameters of 10, 30, and 60 nm without any additional sample preparation. For nominally 10 nm sized Au particles, an individual peak is observed at ~ 14 nm. However, for both of the 30 nm and 60 nm samples, two peaks are observed: One close to the expected nominal particle size (29 nm or 58 nm respectively) and another peak of much higher intensity centered at ~ 11-12 nm. Deposition of the electrosprayed particles on a TEM grid confirmed, as shown in Figure 3.2b, that they are two distinctly different sizes with different image contrasts. The large sized nanoparticles (dark ones) in the TEM images corresponded to the nominal peak size of the Au-NPs, and the small sized particles (light ones) corresponded to the "extra" much smaller peak seen in the 30 and 60 nm cases. Furthermore, the smaller particles in the TEM are clearly much more numerous, consistent with the DMA/CPC results.

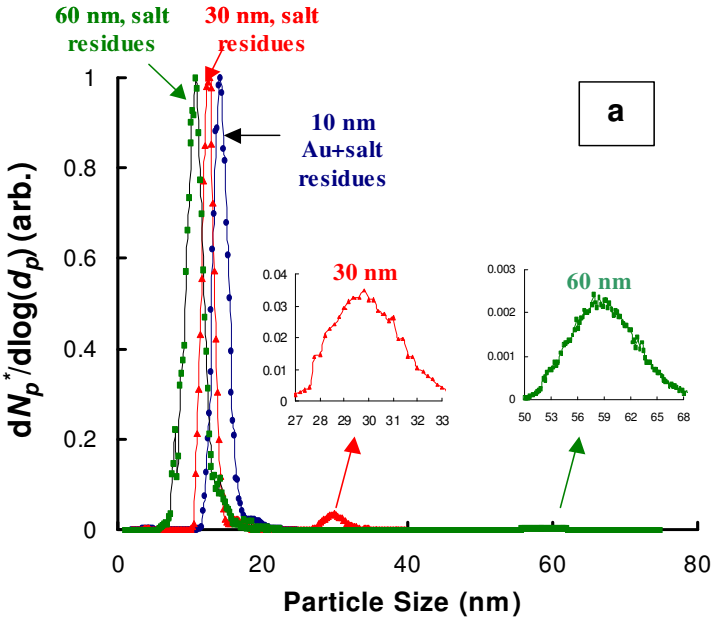

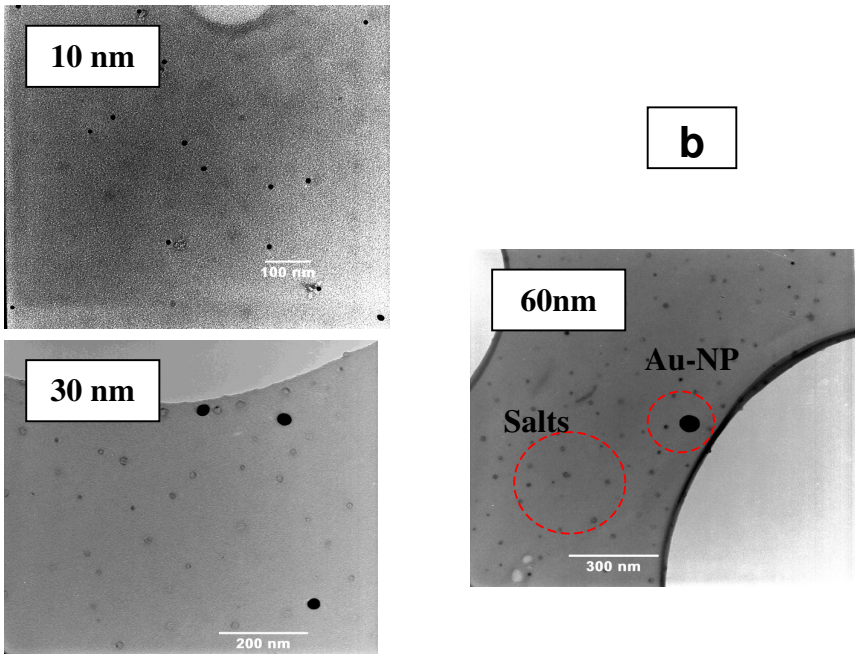

Figure 3.2: (a) Particle size distribution with 10 nm particles (spheres ●), 30nm (triangles ▲), and 60 nm (squares ■). All three sized Au nanoparticles are as-received samples (unconjugated and uncleaned). (b) TEM images of samples shown in (a).

We attribute the peak observed at ca. 11-12 nm is attributable to salt remnants in the Au colloid solution. Commercially available aqueous colloidal gold suspensions, like the ones used in the present study, are often stabilized using sodium citrate. XPS characterization of dried films of unconjugated Au colloids confirmed the presence of Na (1071.9 eV) and the presence of a C 1s peak at 289.1 eV, shifted 3.9 eV from the main elemental hydrocarbon peak at 285.2 eV, that is typically seen in samples containing carboxylic acid moieties as would be expected for sodium citrate [53]. On the basis of these results, we conclude that the peaks seen at < 10 nm in Fig. 3.2 originate from the nonvolatile sodium citrate salts in the commercial Au colloid solution.

Thus, in systems containing a nonvolatile soluble salt and Au-NPs, the ES generates two kinds of droplets. One droplet contains a Au-NP and salt, which upon solvent evaporation leads to a salt encrusts Au-NP. The other simply contains dissolved salt, so that upon solvent evaporation, the remnant becomes a small salt NP. From knowledge of the Au-NP concentration in solution, the droplet diameter, and the generation rate, we can obtain the ratio of the concentration of the two types of drops. From the measured size of the salt remnant particle we can back-out the concentration of the nonvolatile component in the Au-NP containing drop. For example, given the salt NP was measured to be ~12 nm, the volume fraction of salt on the Au-NP was estimated to be ~61 % for 10 nm, ~7 % for 30 nm and ~1 % for 60 nm samples. Thus, size measurement of smaller Au-NPs is more severely affected by salt formation than that for larger Au-NPs.

The relative magnitudes of the smaller peaks in Fig. 2a also comports with the foregoing explanation. For example, the number count of the salt particles should be ~ 1000 times larger than the 30 and 60 nm particles as determined by the drop size and the salt and Au-NP concentrations. Experimental observation, however, shows the ratio to be closer to 100, which discrepancy we attribute to transport losses of the smaller particles.

To unmask the salt shell from very fine particles (i.e. the nominally 10 nm diameter particles), a "cleaning" procedure was developed. Au-NPs were centrifuged and the supernatant containing excess salt was removed. The Au-NPs were then re-suspended with aqueous ammonium acetate solution, a volatile salt, to obtain the necessary conductivity. Through this process we effectively dilute the salts without diluting the colloids. Figure 3.3 shows the size distribution of Au colloids after centrifugation and re-suspension. Now for all three samples, we clearly see two peaks in the particle size distribution, corresponding to the Au nanoparticles and salt residues. The now distinct salt peak diameter, d_s, shrunk from 11-12 nm to 4-5 nm after processing. Thus, the volume of the salt particles decreased by ~ 18 times, in reasonably accord with the extent of dilution.

(2) Estimation of Mobility Size of Bare Au Nanoparticles

We obtained a corrected value for the mobility size of bare Au nanoparticles, $d_{p0,}$ by taking into account the contribution from the salt residue [54] with the expression:

$$d_{p0} = \sqrt[3]{d_{p,m}{}^3 - d_s{}^3} \qquad (3.2)$$

where $d_{p,m}$ and d_s are mobility sizes measured by DMA of the Au-NP encrusted with salts and the salt NP, respectively. Table 3.1 summarizes the results of this formula for spectra in Fig. 3.2. The table highlights the value of Eq. 2 to determine the salt-free value of d_{p0}. Indeed, correcting for the volume of the salt crust brings both values of d_{p0} into agreement within the limit of the DMA's resolving power. Hence Eq. 2 provides a simple way to obtain the size of bare Au-NPs under different salt concentrations (i.e. with varying d_s). Correcting for small changes in the net particle diameter is absolutely critical to distinguishing the increase in size after functionalization, to be discussed next.

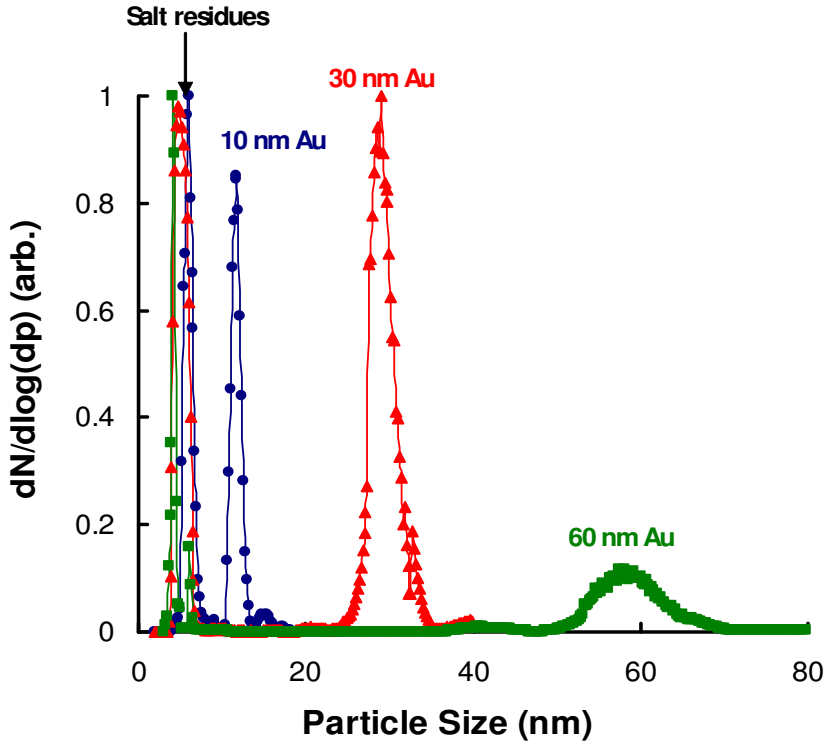

Figure 3.3: Particle size distribution with 10 nm particles (spheres ●), 30nm (triangles ▲), and 60 nm (squares ■). All three sized Au nanoparticles are as-received samples (unconjugated) after centrifuge cleaning.

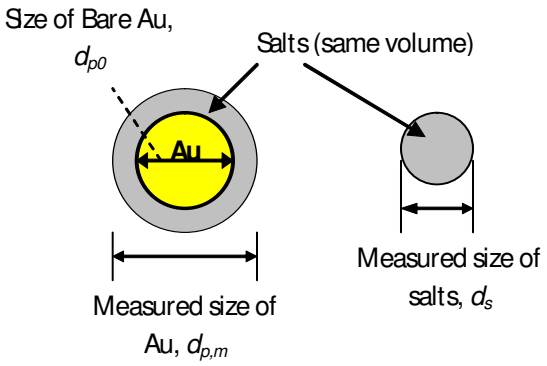

Nominal size (nm)	As received NPs			Processed NPs		
	$d_{p,m}$(nm)	d_s (nm)	d_{p0} (nm)	$d_{p,m}$ (nm)	d_s (nm)	d_{p0} (nm)
10	14.2	14.2	N/A	10.8	5.0	10.4
30	29.8	12.6	29.0	29.0	4.8	29.0
60	58.4	10.8	58.3	58.2	4.2	58.2

Table 3.1: Summary of particle sizes for unconjugated Au nanoparticles. $d_{p,m}$ and d_s are the particle mobility size of Au and salt-residue particles measured in Fig. 3.2 (as received) and Fig. 3.3 (processed). d_{p0} is the particle size of bare Au after the correction of salt residues on Au surface.

3.1.3.2 Conjugated Au nanoparticles

(1) Formation of Self-Assembly Mononlayer

Before measuring the thickness of SAM with ES/DMA, we confirmed the presence of the SAMs on the Au nanoparticles in the colloid phase using FTIR, XPS and TEM. We react two different thiols, 11-mercaptoundecanoic acid (99+%, MUA, negatively charged) and (1-mercapto-11-undecyl)tri(ethyleneglycol) (99+%, PEG, neutral), to 30 nm Au colloids. Briefly, FTIR characterization of dried films of SAM modified Au-NPs revealed vibrational features consistent with those observed for full monolayer coverage molecular layers formed of the same molecules on 2-D planar gold surfaces. XPS analysis of dried SAM modified Au-NP films on indium substrates also confirmed the presence of chemical functional groups expected after SAM modification. The ratio of S/Au peak intensities measured for modified Au-NPs was comparable with that measured for SAM films formed on 2-D planar surfaces, suggesting that similar molecular coverages are achieved on both substrates. TEM images (Figure 3.4a), reveal well-defined spacing between Au nanoparticles, suggesting that both MUA and PEG monolayers create a uniform coating on the Au nanoparticles to separated the Au-NPs [55]. Combined, the FTIR, XPS and TEM characterization data suggest the Au-NPs to be fully conjugated by the SAM modifiers.

This increase in size with the SAM should be observable with the ES/DMA. Indeed, the size distribution does shift to larger sizes for both MUA- (~2 nm) and PEG-coated (~1.7 nm) Au-NPs, as seen in Fig. 3.4b. Thus, we are able to detect the presence of SAM conjugation on the Au-NPs based on the difference in electrical mobility

between conjugated and bare Au-NPs in support of the FTIR, TEM, and XPS results. We now shows this change in size to obtain the surface coverage and binding energy may be obtained from ES-DMA as described in the next section.

(2) Evaluation of Surface Packing Density of SAM

The ability to size coated particles with 2 Å precision allows us to derive a reliable correlation between the change in particle size and the surface packing density of molecules within the SAM coating. We define a change in particle size as $\Delta L = d_p - d_{p0}$ where d_p and d_{p0} represent the coated and uncoated particle mobility diameter, respectively (Fig. 3.4c).

We now consider a simple core-shell model for the change in particle size (ΔL_1), considering only the molecular dimensions of the close-packed self-assembled monolayer normal to the particle surface and neglect any curvature effects. The length of an alkanethiol molecule, l, is,

$$l = a + bN \qquad (3.3)$$

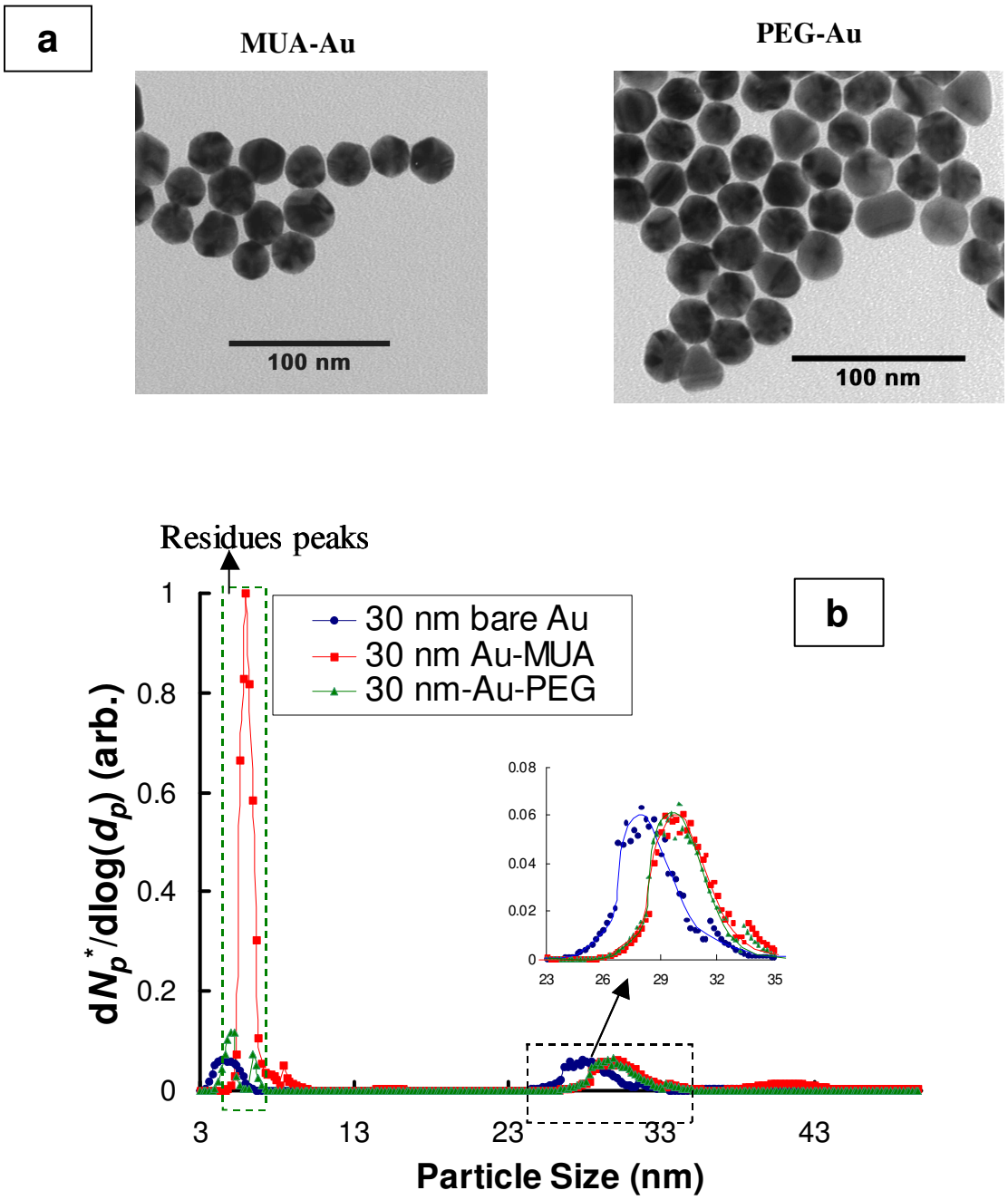

Figure 3.4: (a) TEM images of conjugated Au-NPs. Particle size was 30 nm. Au-NP were conjugated with MUA (left) and PEG (right). (b) Particle size distribution of Au-NPs with different kinds of SAM-coatings conditions. Blue spheres (●): bare Au-NPs; Red squares (■): MUA-coated Au particles; Green triangles: PEG-coated Au particles.

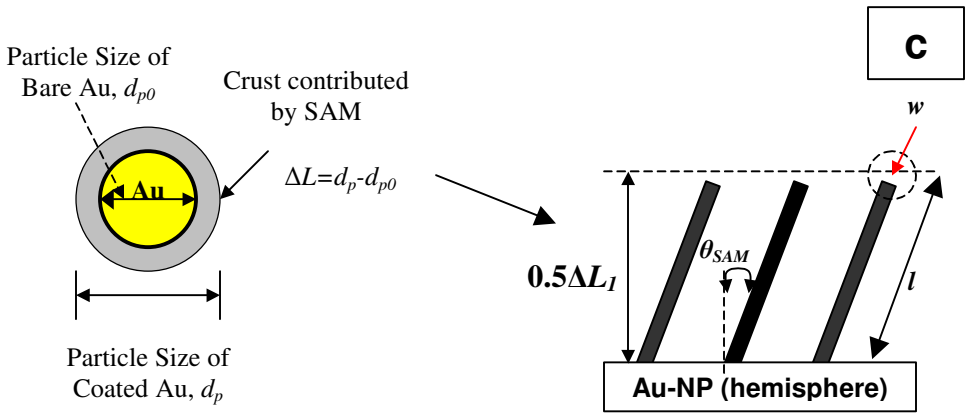

Figure 3.4: (c) Conceptual model of SAM-coated Au-NP. l and w are the length, l and diameter of a cylinder-like SAM molecule. θ_{SAM} is the tilt angle of SAM molecule normal to the surface.

where a is the contribution to the length from the thiol linkage at the Au surface to the SAM terminal functional group, b is the length of repeating methylene (CH_2) groups in the SAM backbone, and N is the number of CH_2 groups. Using previously published parameters for MUA [55-57], a = 0.3 nm, b = 0.127 nm, and N =10, the expected length of a MUA molecule is 1.57 nm. ΔL_1 is further refined by recognizing that molecules within a full covered SAM on a 2-D surface typically exhibit an average tilt angle to the surface normal, θ_{SAM}, of approximately 30° [57]. The addition to the diameter of the nanoparticle due to the SAM then becomes,

$$\Delta L_1 = 2l\cos(\theta_{SAM}) \qquad (2.4)$$

For MUA, ΔL_1 = 2.72 nm. *Note that this model implies ΔL_1 to be independent of the Au-NP size.*

Comparing theory to experiment, we find ΔL from experiment (~2.0 nm, Fig. 3.4b) to be ~35 % lower than the predicted value (ΔL_1 = 2.72 nm), indicating that a SAM-coated Au-NP has a lower drag than other rigid (metal or metal oxides, etc) core-shell particles. The most obvious reason would be that the SAM coating is not really a dense material. On average the SAM chains have an interchain spacing ~0.5 nm, about 3-5 times longer than the length of a chemical bond. As such the surface can be thought of as somewhat porous and the energy transfer from gas collision to the work of drag may be changed from that of dense core-shell particles. There is some evidence for this. For example, Shutler et. al via molecular beam experiments observed that a SAM affected gas-surface energy transfer and found that the interaction between SAM chains played a

role in the magnitude of the energy transfer. In particular, SAM chains with smaller chain-chain interactions (large-spacing) had greater translational-to-vibrational (TV) energy transfer [58]. At present there is no obvious way to connect the results of changes in TV energy transfer, to changes in drag force, and therefore the mobility of SAM coated NP's.

To simplify this problem, we introduce an adjustable parameter, α, to incorporate the effect of SAM spacing in the calculation, and obtain a modified mobility diameter, ΔL_2 ($=\alpha \Delta L_1$).

$$\alpha \equiv \frac{A_2}{A_1} = \frac{N_m w l}{\frac{\pi}{4}[(d_{p0} + \Delta L_1)^2 - d_{p0}{}^2]} = \frac{4 d_{p0} \rho^{0.5} l w}{(2 d_{p0} + \Delta L_1)\Delta L_1} \qquad (3.5)$$

where A_1 is the projected area of a rigid, solid shell, A_2 is the effective projected area of SAM, calculated by assuming molecules occupy a cylinder of length, l, and diameter, w, along the circumference ($A_2=N_m w l$, where N_m is the total number of SAM molecules along the circumference). N_m is related to the surface packing density of the SAM, ρ, by $N_m = \rho^{1/2}\pi d_{po}$. For SAM layers on a flat gold surface, $\rho \approx$ ~4.6×10^{14} cm^{-2} [57], and for a MUA-coated Au-NP, w was obtained by calculating the width of the COOH group in a MUA molecule ($w = 2\times(l_{C=O})\sin(\theta_{C=O}) + l_{O-H}$), where $l_{C=O}$ is ~1.43 nm, $\Theta_{C=O}$ is ~50^o [56], and $l_{O\text{-}H}$ is ~0.1 nm. Hence, the w becomes ~0.23 nm. A_1 is the projected area of SAM by assuming it to be a rigid shell. Taking the limit of Eq. 3.5 at constant packing density finds $\alpha \to 0$ as $d_{p0} \to 0$, whereas $\alpha \to \rho^{0.5} w/\cos(\theta_{SAM})$ as $d_{p0} \to \infty$.

In the following, we compare ΔL_2 to our experimental data for MUA-coated particles. We choose four different sized nanoparticles, 10 nm, 20 nm, 30 nm, and 60 nm with a MUA-coating for the comparison. Figure 3.5 shows the ES-DMA mobility size distributions for each NP size before and after coating. For each size we clearly observe an increase in peak size after coating with MUA. After correcting for the residual salt crusts, we can determined the increase in the number-averaged particle size [59] to be ~1.2 ± 0.1 nm for 10 nm particles (3.5a), 1.7± 0.1 nm for 20 nm particles (3.5b), ~1.8±0.3 nm for 30 nm particles (3.5c), and ~2.0±0.3 nm for 60 nm particles (3.5d). These data are plotted in Figure 3.5e, which show that changes in ΔL to be particle size dependent. This figure also compares ΔL_2 predicted by our modified core-shell model (solid) to the experimental measurements (diamonds). ΔL_2 does a reasonable job of predicting the size dependent trends to changes in mobility size. While the model is clearly simplistic it does provide a framework from which to study changes to SAM layers as will be discussed in the next section. It also suggests that greater attention, from a fundamental prospective should be paid in the future to the nature of momentum and energy transfer to "soft" coated NP's.

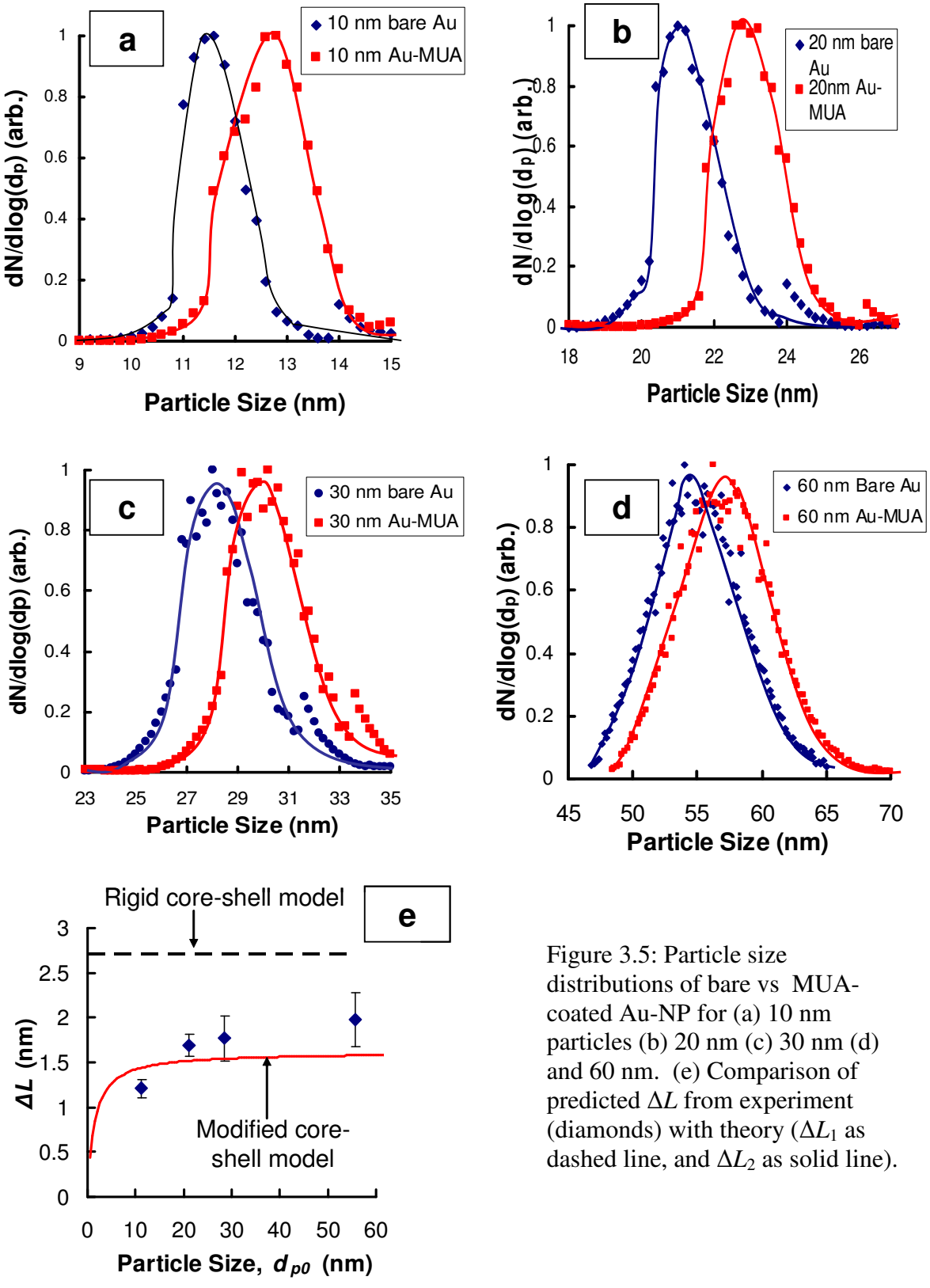

Figure 3.5: Particle size distributions of bare vs MUA-coated Au-NP for (a) 10 nm particles (b) 20 nm (c) 30 nm (d) and 60 nm. (e) Comparison of predicted ΔL from experiment (diamonds) with theory (ΔL_1 as dashed line, and ΔL_2 as solid line).

(3) Temperature-Programmed Desorption of SAMs

We now employ the change in thickness to assess the binding of SAMs to Au-NPs. Prior studies have reported on thermal stability values for SAMs on either 2-D planar Au surfaces or large Au clusters. Terrill et. al [60] conducted a thermal gravity analysis (TGA) on SAM-coated Au-cluster and observed that SAMs were removed from Au clusters at temperatures between 230 - 310 ^{o}C. These results are consistent with the observations by Schieber [57] and Nishida et. al. [61] who employed temperature-programmed desorption (TPD) analysis to monitor the extent of desorption on a planar Au surface. To our knowledge, the thermal stability of SAMs on individual Au -NPs remains largely unexplored.

With the ability to distinguish changes of 0.2 nm, ES-DMA offers the opportunity to further monitor the change in diameter from the thermal desorption of SAMs to gain insight into thermal stability and binding energy. One major advantage of using a gas-phase approach for thermal desorption studies is that thermal processing can be done rapidly, and in the absence of any complicating substrate effects. In particular, the temperature of the particles is well known (i.e. the temperature of the gas) due to their small thermal mass.

In this work, we carried out an in-situ temperature-programmed desorption (TPD) characterization using our ES-DMA system, as depicted in Figure 3.6a. Conjugated nanoparticles generated from the ES process were carried into a flow reactor, heated to various temperatures between 20 °C and 400 °C for residence times ~0.3-1.2 s, and then sent directly to the DMA for mobility size characterization.

Figures 3.6b and 3.6c show the change in ΔL as a function of reactor temperature. This figure shows a monotonic decrease in the apparent coating thickness with increasing temperature, where T is the temperature of the Au-NP, t is the reaction time (the residence time in furnace), and ΔL_0 represents ΔL at the initial condition ($T = T_0 = 20^oC$, $t = 0$). For all particles at the same reaction time (Fig. 3.5b, $t \approx 1.2$ s), we observed that MUA was effectively fully removed from the gold surface at T=300-350 ^oC independent of particle size. Considering the effect of reaction time (Fig. 3.6c, 20 nm particles), we observed that the required temperature for full desorption ($\Delta L/\Delta L_0 = 0$) increased from ~300-325 ^oC to ~375 ^oC when the residence time decreased from 1.19 s to 0.3 s, indicating that the desorption temperature was increased when the heating rate was increased. The relative high temperature of desorption confirms that the MUA is chemisorbed to the surface rather then physisorbed (T<80 ^oC) [57].

From the observed change of $\Delta L/\Delta L_0$ we can back out the change in the surface packing density of the SAM on an Au-NP. We first define $\rho^* = \frac{\rho(T)}{\rho(T_0)}$ and $\Delta L^* = \frac{\Delta L(T)}{\Delta L(T_0)}$. For the size range we considered, our model provides a simple correlation between ΔL, which we measure, and ρ, which we employ to determine the binding energy in normalized terms,

$$\rho^* = (\Delta L^*)^2 \qquad (3.6)$$

With Eq. 3.6, we evaluate the extent of thermal desorption of the SAM simply from the change of ΔL measured by the DMA.

Nishida et al describe the desorption rate, D_r, of MUA from a flat gold surface as a 2nd order reaction, and we adopt their description here for the gold particle and check for consistency [61]. The 2nd order desorption involves a dimerization process of SAM molecules at higher temperature ($T > 200^{o}$C), when the surface coverage is high [61, 62].

$$D_r = -\frac{d\rho^*}{dt} = k_1(\rho^*)^2 \qquad (3.7)$$

Using Eq. 3.7 and the Arrhenius form of k_1, we may evaluate of the apparent binding energy (E) between MUA and Au from the TPD results. With the initial condition $\rho = \rho(T_0)$ at $t=0$,

$$\ln\left(\frac{1}{\rho^*} - 1\right) = \ln(At) - \frac{\Delta E}{RT}, \qquad (3.8)$$

where k_1 is the rate constant ($= Ae^{(-E/RT)}$), A is the Arrhenius-factor and E is the activation energy. Fitting our TPD data to Eq. 3.8 in Figure 3.7 shows that a second order Arrhenius model fits the data quite well, and yields an Arrhenius-factor of 1.0×10^{11} s^{-1} with an activation energy E ~105 ± 10 kJ/mol for all three sizes of Au-NPs. Thus, for the range of sizes we considered, the curvature effect is negligible as each MUA molecule only has an arc of 4^{o} or less on the Au surface. This result implies binding of SAM's to Au-NP, at least for $d_{p0} \geq 10$ nm, to be curvature independent.

Accordingly, the energetics we observed are essentially consistent with the work on flat surfaces, where for example, Schreiber [57] observed the activation energy for the desorption from a flat Au surface to be ~126 kJ/mol, which is close to the value, ~115-140 kJ/mol, observed by Nishida et. al [61, 62]. Both these measurements are only

slightly higher than our 105 kJ/mol result, indicating that binding on the NP may not be significantly different from that observed on a flat surface.

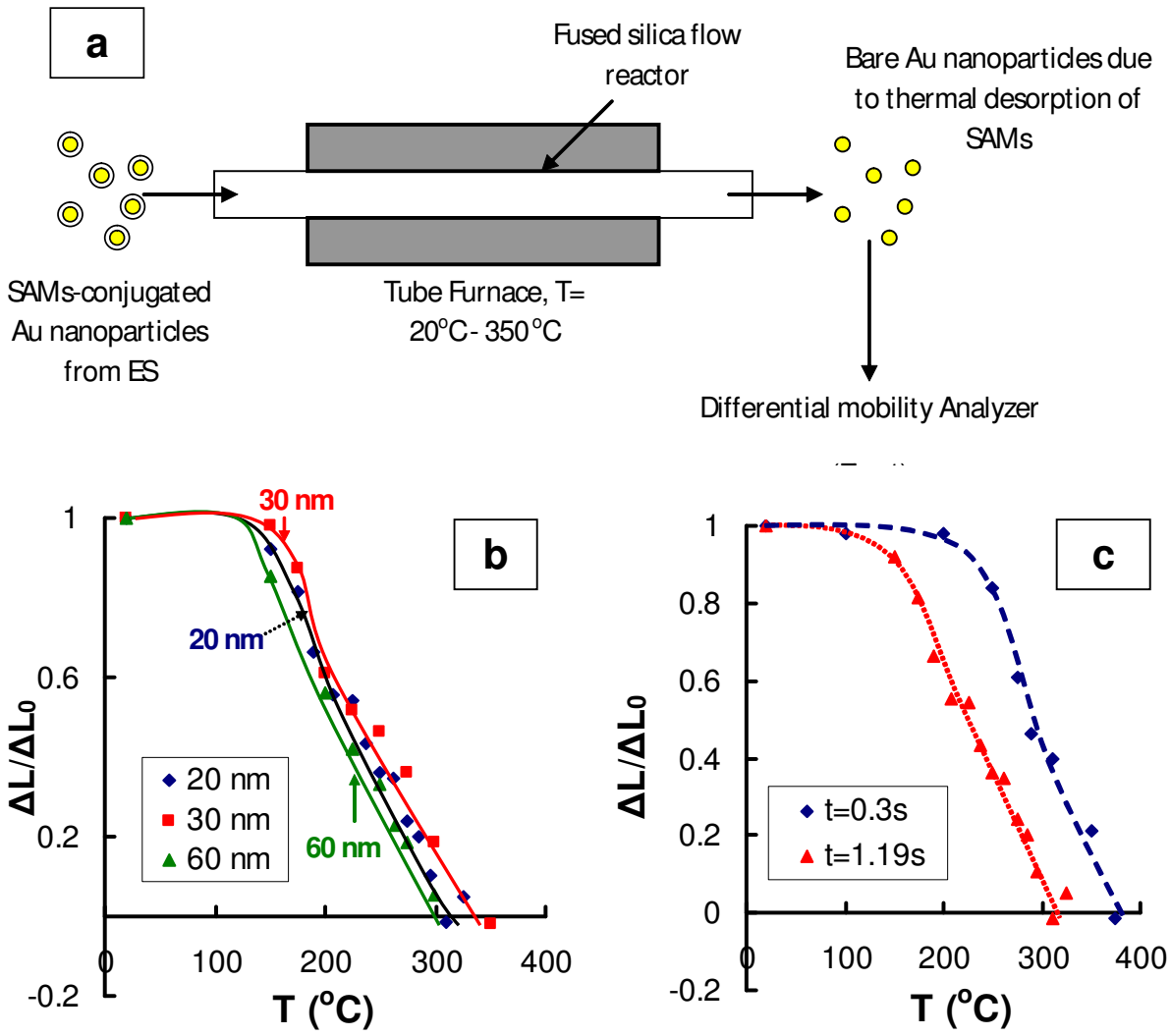

Figure 3.6: (a) Schematic of the temperature-programmed desorption (TPD) experiment. (b) ΔL^* (=$\Delta L/\Delta L_0$) vs T for three different sized Au nanoparticles, 20 nm, 30 nm and 60 nm. t: 1.2 s. (c) ΔL^* vs T for two different residence time, t =0.3 s and 1.2 s.

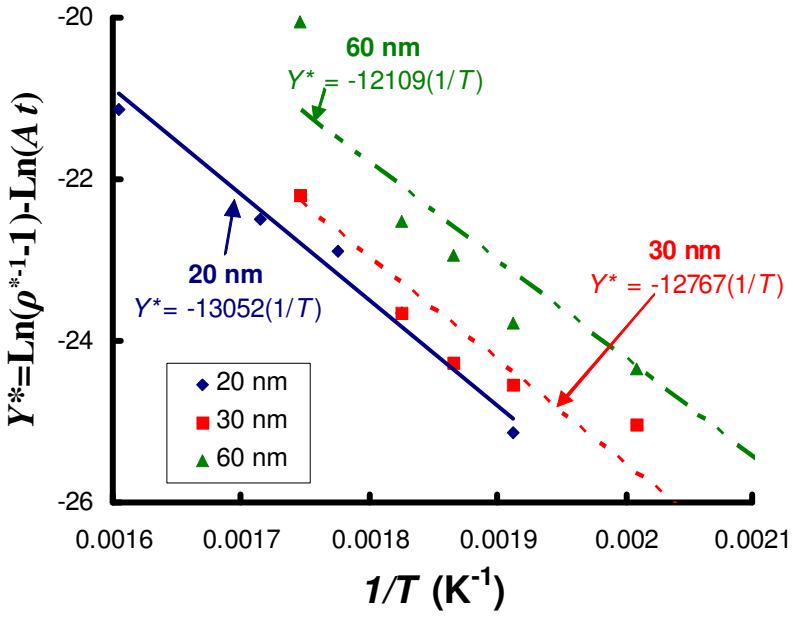

Figure 3.7: Arrhenius plots for three different sizes of Au-MUA particles. T=200-350°C. t =0.3 s for 20 nm Au-NPs and t =1.2 s for both 30 nm and 60 nm Au-NPs. Y^*=Ln(ρ^{*-1}-1)-Ln(At). The slope = $-E/R$. R =gas constant (8.314 Jmol^{-1}K^{-1}).

3.2 Flocculation Kinetics of Colloidal Nanoparticles Measured by Gas-Phase Differential Mobility Analysis

3.2.1 Introduction

Colloidal dispersions of nanoparticles have attracted attention for their variety of uses. For example, medical interest in colloidal gold particles may play a role in the diagnosis and treatment of cancers [2, 3, 46]. However, aggregation of colloidal nanoparticles represents a challenge to the development of nanotechnology and nanotherapeutics because aggregation affects the properties of these particles, including the transport, accessible surface area, optical and electronic properties [3, 45, 46].

DLVO theory, named after the seminal contributions of Derjaguin and Laudau, and Verwey and Overbeek, provides the foundation for a rigorous understanding of colloidal stability and, conversely, colloidal aggregation. This theory balances van der Waals attraction against electrostatic repulsion of like charged particles, and has been used previously to characterize Au-NP aggregation [63]. Thus, consideration of parameters, such as the surface potential of the particle, and the Hamaker constant are vitally important to enable design of functionalized engineered nanoparticles based colloids [64-73].

In this paper we present a novel method to determine the flocculation rate of colloidal nanoparticles by a gas phase analysis. Nanoparticle suspensions can be monitored by sampling the colloidal solution via electrospray (ES), transforming a nanoparticle dispersion to a nanoparticle aerosol, followed by differential ion-mobility analysis (DMA) to determine the mobility distribution, and thus the aggregate

distribution. By sampling at various times we determine the flocculation rate from which the parameters that control aggregation may be elucidated. In contrast to other techniques, such as microscopy [64, 66] and static and dynamic light scattering (LS) [65, 67, 68, 73], ES-DMA can rapidly and quantitatively identify the concentration of each aggregation state (i.e. individual particles, dimers, trimers and tetramers, etc.). Moreover, ES-DMA is most effective for small number aggregates and nano-sized particles (diameter<100 nm), which pose a significant challenge to other methods, especially in monitoring the flocculation of colloidal nanoparticles in the early stage.

We first present a review of the theoretical underpinnings of colloidal flocculation and describe our experimental approach. Next, we present mobility and aggregation distributions of colloidal gold nanoparticles (Au-NP), the representative materials, determined by ES-DMA. By monitoring the aggregation distribution as a function of ionic strength and reaction time, we provide data with which to determine the flocculation mechanism (rate constant, stability ratio) and surface potential of colloidal nanoparticles. Finally, dimensionless analysis is used to determine values of experimental parameters governing the aggregation.

3.2.2 Theory of Brownian Flocculation of Colloidal Nanoparticles

To place our efforts in context and provide a foundation for our analysis, we briefly review the now classic model of Brownian flocculation [70]. The model considers three influences on the particles. The first, Brownian motion, is always important in the colloidal regime, and so we scale all other energies, Φ, with the thermal energy, k_bT,

where k_b is Boltzmann's constant. The second influence is the van der Waals force represented by the Hamaker constant, A_{eff}. The third and final influence, the electrostatic force, depends on the surface potential, ψ_s, modulated by the ionic strength of the solution through the Debye-Hückel length, λ_D ($\approx 0.305nm/\sqrt{n_s}$ with n_s as the ionic strength in mol/L [74]). Equations 3.9-3.11 balance contribution by the electrostatic (E_e) and van der Waals (E_{vdw}) energies between two equally sized spherical particles:

$$\frac{\Phi}{k_bT} = \frac{1}{k_bT}(E_e + E_{vdw}) \tag{3.9}$$

$$E_e = B_1 \exp(-\kappa h) \tag{3.10}$$

$$E_{vdw} = -\frac{B_2}{h}. \tag{3.11}$$

Here, E_e represents the energy of electrostatic repulsion between two spherical particles where $B_1 = \frac{8ak_bT}{z^2 l_b}\tanh^2(\frac{ez\psi_s}{4k_bT})$ with constant potential conditions, $\kappa = 1/\lambda_D$, z is the charge of the solvated ion, and $l_b = e^2/4\pi\varepsilon_0\varepsilon_r k_bT$ is the Bjerrum length. The shortest distance between two spherical particles having a radius of a and a center-to-center distance r is $h = r-2a$. E_{vdw} is the energy of van der Waals attraction between two spherical particles where $B_2 = aA_{eff}/12$ under the Derjaguin approximation in the non-retarded limit [70] with A_{eff} of 3.0×10^{-19} J for Au-NP in water [70].

Figure 3.8 presents Φ/k_bT versus the separation distance, h, between two spherical Au-NPs for the reaction-limited (curve 1), intermediate (curve 2), and diffusion-limited (curve 3) regimes, respectively. The definitions of reaction-limited and diffusion-limted

may be found in ref [70]. Irreversible flocculation occurs as two particles approach each other and fall into the primary minimum near $h = 0$. In the reaction-limited regime, the sum of energies possesses both a maximum, Φ_{max}/k_bT near $r = 2a+\lambda_D$ [70], and a secondary minimum, Φ_{sec}/k_bT at relatively large particle separation, $h = r_{sec}$. The difference between these two provides an energy barrier to minimize or prevent flocculation. A dimensionless energy barrier to Brownian flocculation, E_a^*, can be defined as,

$$E_a^* = \frac{1}{k_bT}(\Phi_{\max} - \Phi_{\sec}) \tag{3.12}$$

$$\frac{\Phi_{\max}}{k_bT} = \frac{1}{k_bT}(0.37B_1 - \frac{B_2}{\lambda_D}) \tag{3.13}$$

$$\frac{\Phi_{\sec}}{k_bT} = \frac{1}{k_bT}(B_1 e^{-\kappa r_{\sec}} - \frac{B_2}{r_{\sec}}) . \tag{3.14}$$

For highly stable suspensions (i.e: the reaction-limited regime), $|\Phi_{max}| >> |\Phi_{sec}|$ such that $E_a^* \approx \Phi_{\max}/k_bT$. Conversely in the diffusion-limited regime (curve *3*), neither Φ_{max}/k_bT nor Φ_{sec}/k_bT are significant, such that the energy barrier is negligible or non-existent. In the intermediate regime (curve *2*), both Φ_{max}/k_bT and Φ_{sec}/k_bT possess similar magnitudes, so, Φ_{sec}/k_bT cannot be ignored in the evaluation of E_a^* in contrast to the reaction-limited regime. Because the intermediate regime is essential to our subsequent analysis, we now provide an analytical, approximate expression for Φ_{sec} that in turn depends on the separation of the particles, r_{sec}, through Eq. 3.14. Intuitively, we should be able to take the first derivative of Eq. 3.9 [i.e.: set $d(\Phi/k_bT)/dh=0$], however, this results in a transcendental expression for r_{sec}. To circumvent this difficulty, we

numerically calculated $\exp(-h/\lambda_D)$ for the intermediate regime where $2\lambda_D < h < 5\lambda_D$. In this domain, we find that $1.26(h/\lambda_D)^{-3}$ to be sufficiently precise, enabling an analytical solution for r_{sec}. Thus, Eq. 3.9 becomes

$$\frac{\Phi}{k_b T} = \frac{1}{k_b T}(1.26\ B_1 \kappa^{-3} h^{-3} - \frac{B_2}{h}) . \qquad (3.15)$$

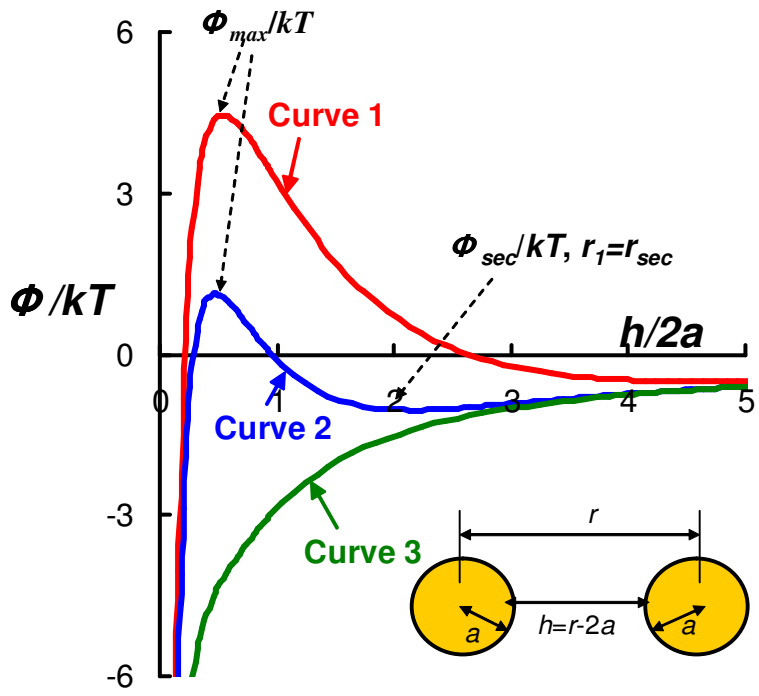

Figure 3.8: Interaction potential for two spherical colloidal nanoparticles (Particle diameter is 10 nm). Surface potential is 64 mV. Curve 1 represents particles in the reaction-limited regime (C = 1 mmol/L), Curve 2 represents particles in the intermediate regime (C = 3 mmol/L), and Curve 3 represents particles in the diffusion-limited regime(C = 20 mmol/L). a is the radius of the particles, r is the center-to-center distance between two particles, and $h = r-2a$. C is the salt concentration.

Now setting the first derivative of Eq. 7 to zero gives $r_{\sec} = \sqrt{\frac{3.78 B_1 \lambda_D^{\ 3}}{B_2}}$. The energy barrier, E_a^* of Eq. 3.12, then becomes

$$E_a^{\ *} = \frac{1}{kT}\left(1.26 B_1 - \frac{B_2}{\lambda_D} + 0.343\sqrt{\frac{B_2^{\ 3}}{B_1 \lambda_D^{\ 3}}}\ \right) \qquad (3.16)$$

in the intermediate regime. Generally, E_a^* is affected by several variables including ionic strength, particle size, and surface potential—each of which can be measured or set in an ES-DMA experiment. The remainder of this paper demonstrates how to obtain relationships among these variables in the intermediate regime with DLVO theory enabled by ES-DMA for the purpose of predicting the stability of nanoparticle suspensions.

3.2.3 Experiment

3.2.3.1 Materials

Commercially available monodisperse Au colloids (10 nm, citrate stabilized, Ted Pella Inc.) were used in this work. The Au colloid suspension was first centrifuged to separate the colloids from the supernatant containing excess citrate ions. The supernatant was removed (typically 950 μL of a 1 mL sample), and replaced with an equivalent volume of aqueous ammonium acetate (Sigma, 99.9 %) solution—the volatile salt we used to systematically vary the ionic strength. To avoid fast flocculation, the concentration of ammonium acetate was varied from 2.12 mmol/L to 9.47 mmol/L.

Though this concentration range is rather modest, it spans the intermediate regime and dramatically affects the kinetics of flocculation on the time scale of our experiments (≈ 20 mins).

3.2.3.2 Electrospray Particle Generation and Differential Mobility Analysis

Figure 3.1 depicts a schematic of our experimental system, consisting of an electrospray aerosol generator, a differential mobility analyzer and a condensation particle counter. A more complete description of the experimental setup and our modifications can be found elsewhere [75, 76]. To achieve better electrical stability in the ES, filtered air was mixed with CO_2 (83 % Air and 17 %CO_2) to increase the dielectric breakdown threshold. Operating with an applied voltage of 2-3 kV, the Au colloids were sprayed in a cone-jet mode and converted from highly charged droplets to neutralized particles having a known Boltzmann charge distribution by passing the aerosol stream through a housing containing an α-radioactive Po-210 source. The "neutralized" particles then passed immediately to the differential mobility analyzer (DMA) for particle size measurement, and were counted with a condensation particle counter (CPC). The diameter of the positively charged Au particles, d_p, was characterized by the electrical mobility, which is inversely proportional to the projected area of the particle [75-78]. In order to achieve sufficient resolution and stability from the DMA, the sheath-to-aerosol flow of the DMA was set to 30. Under these conditions we can collect data with a scanning step size of 0.2 nm because the uncertainty contributed by the DMA remains

less than 0.3 nm [52, 75, 76]. Thus, the width of the peaks in the resulting mobility spectra results primarily from the distribution in particle sizes.

The mobility diameter, $d_{p,n}$, of the Au-NP clusters can be characterized by the ion-mobility spectrum. Dividing the number of positively charged particle measured in the DMA by the fraction of positively charged particles emerging from the electrospray [79], converts the mobility size distribution into an equivalent distribution of spherical particles. Hereafter, we define n as the number of primary particles (herein termed monomers, i.e. $n = 1$) contained in an aggregate ($n = 2$ for a dimer, $n = 3$ for a trimer, and $n = 4$ for a tetramer). Transmission electron microscopy (TEM) confirms the equivalent mobility diameter of clusters of 10 nm primary Au-NPs to be ≈ 14 nm for dimers, ≈17 nm for trimer, and ≈20 nm for tetramers.

By integrating the peaks for each *n-mer* in the ion-mobility spectrum [14, 80], the number of Au particles in different aggregation states $N_{c,n}$, can be determined from the ES-DMA,

$$N_{c,n} = [\int_{d_{p,n,\min}}^{d_{p,n,\max}} \frac{dN_{g,n}}{dd_p} dd_p] \times \frac{Q_g}{Q_l} \qquad (3.17)$$

where $N_{g,n}$. is the measured concentration of Au-NP in gas phase, Q_l = 66 nL/min, Q_g =1.2 L/min, and $d_{p,n,max}$ and $d_{p,n,min}$ are the maxima and minima diameter of n-mer particles, respectively.

3.2.4 Results and Discussion

Our objective is to develop a systematic approach to detect liquid-phase aggregation using the ES-DMA. One advantage of our approach is that even a small change in Au flocculation should be detectable. We restrict the scope of the homoaggregation studied here to the earliest stages of flocculation where single particles form small clusters (<5 primary particles) prior to significant cluster-cluster aggregation, though ES-DMA can examine larger flocs. To achieve these conditions, we employ very dilute suspensions with concentrations of less than 0.1 mg/mL or a volume fraction of ~ 10^{-6}.

While it is possible for aggregation to occur in the gas phase, the particle concentration both within the aerosolized droplet (0.04 particles per droplet), and in the gas phase (at most 10^6 particles/cm^3) is sufficiently dilute, and the residence time is sufficiently short, to prevent significant aggregation (<10 s in the gas phase). Thus, we believe the observed aggregates accurately reflect the aggregation in the liquid phase. Unless we intentionally force aggregation by adding salts, the fraction of aggregated particles (not monomers) is exceedingly small, and often below our detection limit. Upon addition of salts, the solution changes color from a bright red to a purple or blue color which is characteristic of aggregated gold clusters [45].

We begin our work by identifying the peaks in the ion-mobility spectrum, and then proceed to the time-dependent kinetic study. From a temporal change in the number concentration of each aggregation state, we estimate the flocculation rate of Au-NP. From this, we estimate the surface potential between the colloidal Au nanoparticles and

compare it to surface potentials measured by other methods to test the validity of our results.

(1) Effect of Ionic Strength

Figure 3.9 presents ion-mobility spectra of gold colloids at various concentrations of ammonium acetate, *C*. Each spectrum presents up to five distinctive peaks representing salt residues and clusters containing one to four individual Au particles, which we term monomer, dimer, trimer, etc. The ion-mobility of the monomer peak (n = 1) results in a diameter of 11.6 nm consistent with the original colloidal sample encrusted with salts [76]. Further assignment of the dimer peak to 14.8 nm, the trimer peak to 17.4 nm, and the tetramer peak to 19.4 nm was confirmed by specifically depositing particles corresponding to each peak exiting the DMA on a TEM grid inside an electrostatic deposition chamber. TEM then confirms the identity (i.e the peak labeled as tetramer does contain four particles) [77, 81].

Figure 3.9a shows how the concentration of each cluster or aggregation state varies with salt concentration. As seen in Fig. 3a, the intensity of the monomer (n = 1) decreased, and the intensity of the dimer (n = 2), trimer (n = 3), and tetramer (n = 4) increases as *C* increases, reflecting the decreased electrostatic repulsion between Au-NPs due to a decrease in the Debye screening length with added salts. Importantly, this result indicates that one can clearly distinguish the aggregate distribution in solution with ES-DMA, and clearly identify changes due to solution conditions.

Figure 3.9b further quantifies the effect of the ionic strength on the extent of aggregation and the normalized monomer concentration $N_{c,n=1}/N_0$, where N_0 is the initial monomer concentration (4.6×10^{11} particles/cm^3) . Low ammonium acetate concentrations (i.e: C = 2.12 mmol/L) result in stable colloids leaving individual monomers (n = 1) to dominate the size distribution. As the salt concentration increases, significant quantities of dimers and trimers are observed. Increasing the salt concentration further to C = 9.47 mmol/L, left exceedingly few monomers to be observed such that $N_{c,n=1}/N_0$ fell sharply. Thus, our measurements are in excellent qualitative agreement with the predictions of the DLVO theory [64-73] as expected.

We note in passing the separation between the first few peaks in Figure 3a. One distinct advantage of using ion-mobility spectrometry is the clear differentiation among monomer, dimer, trimer, and tetramer species. Thus, ES-DMA is particularly sensitive for nano-sized material (<100 nm) in the early stage of flocculation. Changes in these concentrations can be tracked in time—a capability we use to study the flocculation kinetics as described in the next section.

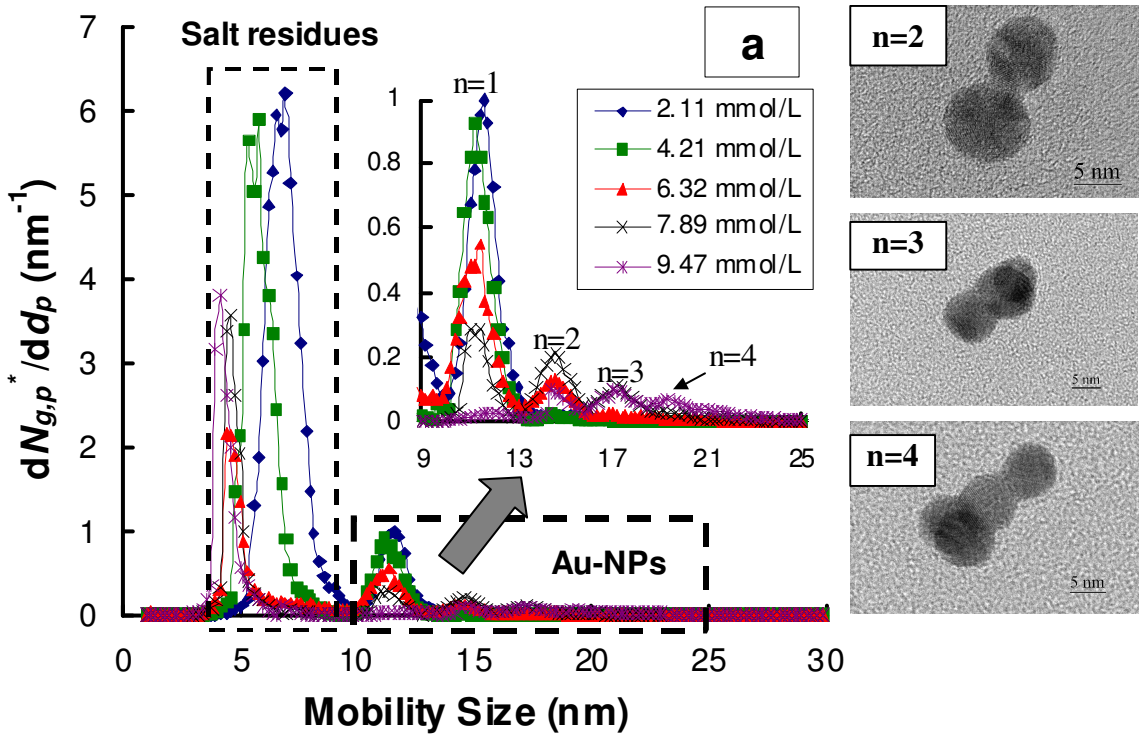

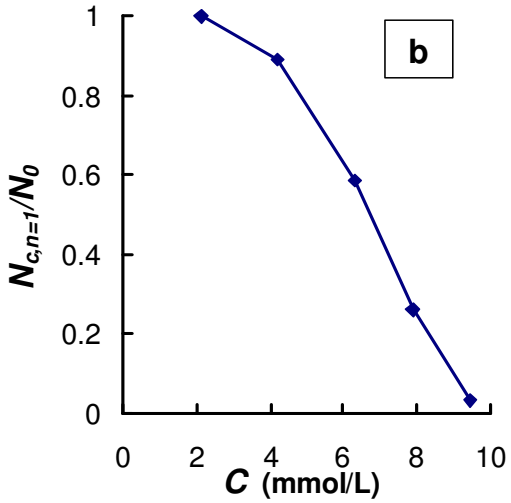

Figure 3.9: (a) Ion-mobility spectrum of colloidal Au ammonium acetate solution at different ionic strength conditions. Mobility size of individual particles is ≈10 nm. (b) $N_{c,n=1}/N_0$ vs different ionic strength conditions listed in (a). $N_{g,n}$ is the number concentration of Au particles measured by DMA-CPC in the gas phase ($N_{g,n}^{*} = N_{g,n}/N_0$), N_0 is the initial concentration of monomer Au particles, and n is the number of single particles in a Au aggregate. Volumetric fraction of Au-NP in solution is ~10^{-6}, and the reaction time t of sampled Au-NPs is ≈ 20 mins.

(2) Time-Dependent Kinetic Study and Degree of Flocculation

The results in Figure 3 obviously depend on when the flocculating solution was sampled, a fact we now exploit to determine the kinetics of flocculation. To quantify the extent of flocculation, we draw an analogy between the flocculation of colloidal nanoparticles and a step-growth polymerization process to define the degree of flocculation (*DF*).

$$DF = \frac{\sum_{n=1}^{n=4} nN_{c,n}}{\sum_{n=1}^{n=4} N_{c,n}} \qquad (3.18)$$

In this analogy, the average number of "repeat units" in a Au aggregate "polymer chain" corresponds to the average number of particles in an n-mer (where $n > 1$) aggregate. Like a polymer propagation process (our flocculation), *DF* increases from unity as a function of reaction time, *t*. [82]

Figure 3.10 characterize the extent of Au-NP flocculation versus time. For *C*=2.12 mmol/L (Fig. 3.10a), only monomer particles were observed after 9 days, indicating repulsive forces dominate on the experimentally accessible time scale. Hence, the energy barrier, characterized in Fig. 1 is high, and flocculation is reaction-limited when $C < 2.12$ mmol/L. At $C = 4.21$ mmol/L (Fig. 3.10b), monomer particles still comprise the major species, but the concentration of monomer clearly decreases with time; the concentration of dimers and trimers increases with time. When *C* increased to 7.89 mmol/L,

flocculation is very much enhanced as evidenced by both the high concentration of the various *n*-mers relative to the monomer, and the much shorter experimental times (Half-life time, $t_{1/2}$, decreased from days to minutes see Table 3.2).

Table 3.2: Half-life time of primary particles (n=1) versus salt concentration

Salt Concentration (mmol/L)	$t_{1/2}$
2.12	>9 days
4.21	~5 days
6.32	~17 mins
7.89	< 17 mins
9.47	< 17 mins

Note that the detection limit of $t_{1/2}$ is 17 mins.

Figure 3.11a summarizes the temporal changes in the ion mobility size distributions in terms of *n*-mer concentration. In keeping with simple Brownian flocculation, the monomer concentration decreases monotonically, with each successive *n*-mer appearing later in time. For this set of experimental conditions, dimers and trimers reached a peak concentration at t ~80 min and ~ 200 min, respectively. Note that the defined reaction time starts from the moment Au colloids were mixed with ammonia acetate buffer solution, to the time we collect the ion-mobility spectrum.

Fig 3.11b shows *DF* versus t for various ionic strengths. Generally a higher *DF* was observed for longer reaction times and higher ionic strengths. Because of the depletion of monomer Au-NP, at C = 9.47 mmol/L, *DF* approaches a constant when t > 80 min. This result indicates the flocculation rate is dominated by monomer-*n*-mer

interactions such that when the monomer is depleted the aggregation rate essentially stops. This implies that aggregate-aggregate coagulation is too slow to be observed for the time scales and concentration ranges considered here.

(3) Determination of the Rate-Determining Step

Using the curves in Fig. 3.11a we now examine the kinetics of flocculation. Although ES-DMA can inform more advanced models of flocculation, our purpose it to demonstrate the utility of ES-DMA for studies of colloidal aggregation, we draw upon the irreversible population balance equation [83] attributed to Smoluchowski and assume the rate constants, k_D (or coagulation coefficients) to be particle size independent. Using this assumption we write

$$\frac{dN_{total}(t)}{dt} = -k_D[N_{total}(t)]^2, \tag{3.19}$$

where k_D is the lumped rate constant, and $N_{total}(t) = \sum_{n=1}^{n=\infty} N_{c,n}(t)$ is the total number of Au-NP clusters ($\leq N_o$, the total number of primary particles at t=0). Integration finds

$$N_{total}(t) = \frac{N_0}{1 + k_D N_0 t}, \tag{3.20}$$

which we use to plot the decay of $N_{total}(t)$ with t as shown in Figure 3.12. Increasing the ionic strength causes $N_{total}(t)$ to decay more sharply. This result is consistent with an Arrhenius form for the rate constant,

$$k_D = A_o e^{-E_a^*/k_b T}, \qquad (3.21)$$

which depends on both a collision frequency, A_o, and an activation barrier, E_a. As mentioned in section 3.2.2, the activation barrier for flocculation depends on the energy barrier between the secondary minimum (Φ_{sec}/k_bT) and maximum (Φ_{max}/k_bT). As the salt concentration rises, the electrostatic barrier collapses, and the rate constant should likewise increase. Fitting the curves in Fig 3.11 (Table 3.3) finds rate constants of $k_D \approx 10^{-17}$ cm^3/s for C = 4.21 mmol/L, $k_D \approx 8*10^{-17}$ cm^3/s for C = 6.32 mmol/L, $k_D \approx 2*10^{-15}$ cm^3/s for C = 7.89 mmol/L, and $k_D \approx 4*10^{-15}$ cm^3/s for C = 9.47 mmol/L. Comparing these rate constants with a diffusion limited rate constant (k_D^{fast}) value of ~10^{-11} cm^3/s for 10 nm-sized Au-NP's [68, 83] indicates that electrostatic repulsion decreases the flocculation rate by 10^3-10^6 within the range investigated.

$\boldsymbol{C}$ (mmol)	$\boldsymbol{k_D}$ (cm^3/s)
4.21	10^{-17}
6.32	$8*10^{-17}$
7.89	$2*10^{-15}$
9.47	$4*10^{-15}$

Table 3.3: flocculation rate constant versus salt concentration.

From the rate constants, we can determine the energy barrier to flocculation in the primary minimum. First we cast our experimental results into a dimensionless stability ratio,

$$W \equiv \frac{k_D^{fast}}{k_D}, \qquad (3.22)$$

as defined by Lin et. al. [68, 70] which compares the flocculation rate driven solely by Brownian motion to the experimentally observed flocculation rate. Larger values of W correspond to more stable suspensions. Plotting W versus the ionic strength in Fig. 3.13, clearly shows a monotonic decrease in W with C. By extrapolation of the data to $W = 0$, we obtain the critical salt concentration, n_c, to induce Au-NP flocculation (6.5±1.0 mmol/L). Notably, n_c provides an estimation of the onset of rapid flocculation [70].

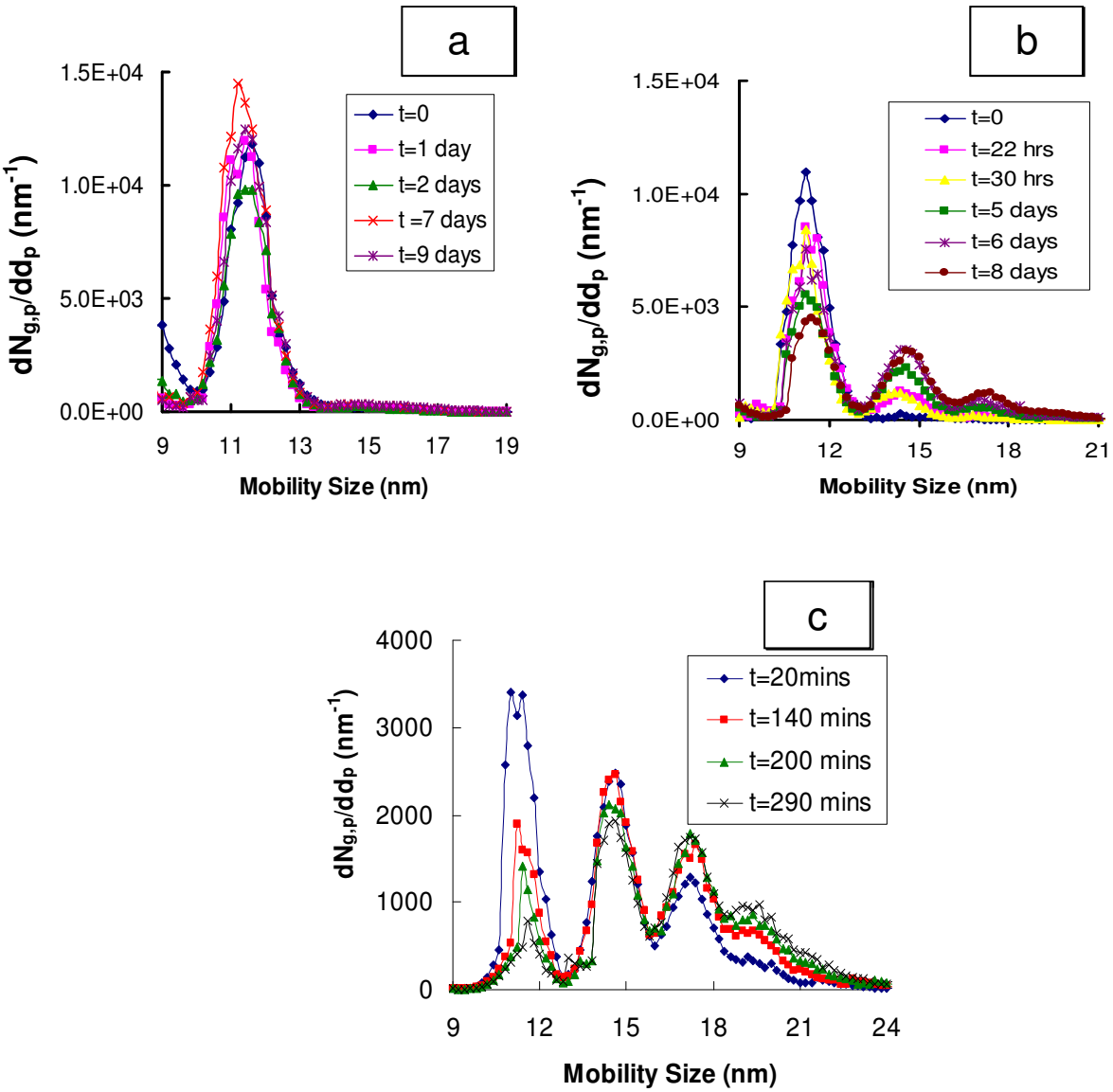

Figure 3.10: (a) Ion-mobility spectra of unconjugated colloidal Au vs reaction time, *t*. Mobility size of monomer is ~10 nm. a: *C*=2.12 mmol/L ; b: *C*=4.21 mmol/L ; c: *C*=7.89 mmol/L.

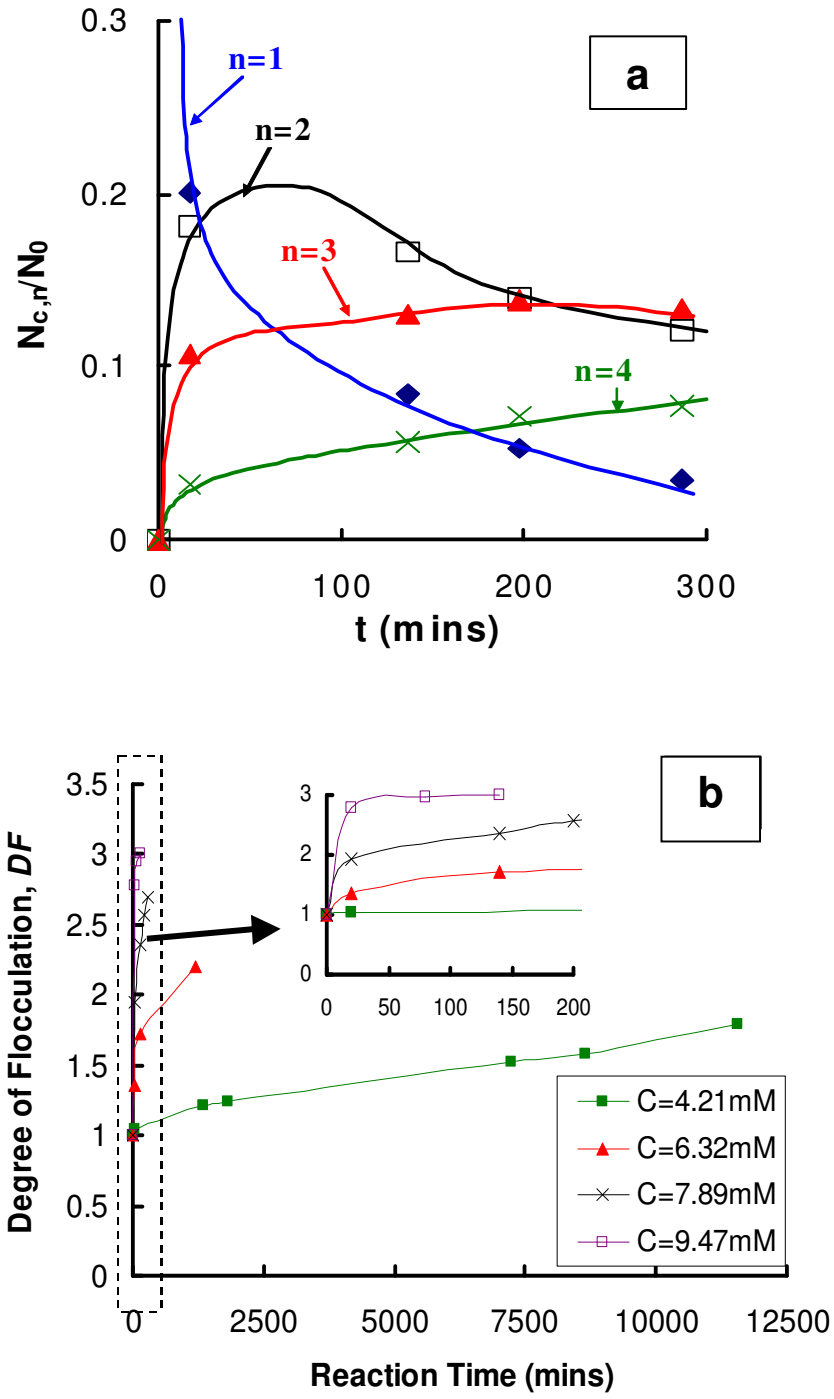

Figure 3.11: (a) Number concentration of different Au-aggregates vs reaction time. C=7.89 mmol/L. $N_{c,n}$ is the number concentration of Au-NP in solution, and n is the number of individual particles in one aggregate. □: n = 1; □: n = 2; ▲: n = 3; ×: n = 4. (b) Degree of flocculation, DF, vs reaction time. C varies from 4.21 mmol/L to 9.47 mmol/L.

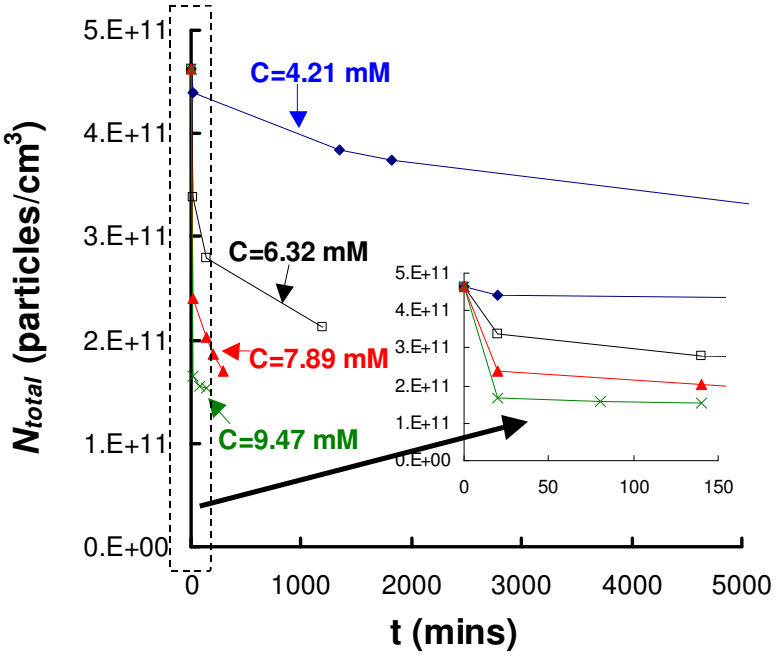

Figure 3.12: Total number concentration of Au–NPs in solution, N_{total}, vs. reaction time, t.

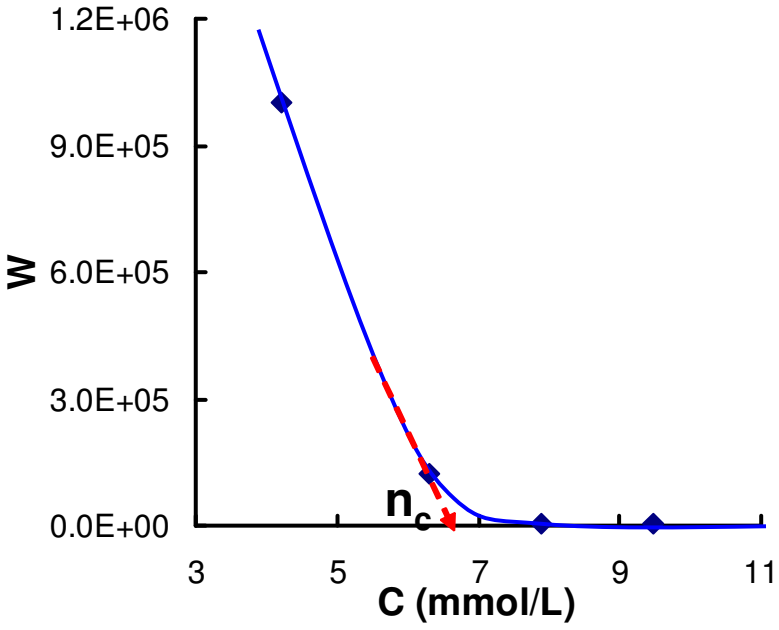

Figure 3.13: Stability ratio of Au colloids vs ionic strength; the interpolate on the X-axis (concentration of ammonium acetate) represents the critical concentration of salt needed for flocculation of Au colloids, n_c.

This value of n_c enables determination of the surface potential between two Au-NPs, ψ_s, and the surface charge density of individual Au nanoparticles, Q_s, through the following equations [70]:

$$|\psi_s| = \frac{4kT}{ez}\left(arctanh\left[\frac{n_c z^6 l_b^3 A_{eff}^2}{49.6(k_b T)^2} \right] \right)^{1/4} \qquad (3.23)$$

$$|Q_s| = \varepsilon_0 \varepsilon_r \kappa |\psi_s| \qquad (3.24)$$

Applying these relationships finds $|\psi_s|$ to be 64 ± 2 mV. This magnitude may be compared with the linear trend in zeta potential versus diameter of citrate stabilized gold measured using a commercial electrophoresis instrument by Kim, et al. [63]. Extrapolating their data to 10 nm finds ψ_s to be -65 mV. The excellent agreement validates ES-DMA as a tool to quantitatively study colloidal stability.

Further applying equation 3.22, we find Q_s to be ≈0.012 C/m^2 (= 0.075 e/nm^2), indicating the average number of elementary charges on the monomer ($d_{p,\, n=1}$ = 10.9 nm) is ~28. Substituting ψ_s back into Eqs. 4-6 yields $E_a \approx 1.4\ kT$ for C = 4.21 mmol/L, ≈ 0.4 kT for C = 6.32 mmol/L, ≈ -0.4 kT for C =7.89 mmol/L, and ≈ -1.0 kT for C = 9.47 mmol/L. Since the diffusion-limited flocculation is defined as $E_a << kT$, the boundary between diffusion-limited and reaction-limited regimes lies in the salt concentration range of ~6-8 mmol/L. Thus, we conclude that the Au-NPs experience intermediate values of the interactive potential as illustrated in Figure 3.9 for the range of ionic concentrations employed in these experiments (C = 4.21 mmol/L to 9.47 mmol/L).

(4) Dimensionless Analysis

We now summarize our analysis and characterization by demonstrating how to extend our analysis to other cases with the DLVO theory. Having determined the surface charges via the critical salt concentration, we now return to Eq. 3.16 to determine the height of the energy barrier. Following the analysis by Prieve and Ruckenstein [69, 70], Fig. 3.14a shows the stability ratio to increase exponentially with the height of the energy barrier, consistent with the theory that increasing the energy barrier of flocculation improves the stability of primary colloidal monomers. This realization provides a convenient means of examining how other parameters such as particle size affect the activation energy and, thus, *W*. As depicted in Fig. 3.13b by assuming a constant surface charge density (0.075 e/nm^2), E_a^* increases linearly with particle size when $E_a^* > 0$ ($C < 5$ mmol/L) and decreases linearly when $E_a^* < 0$. Hence larger particles should display better stability in the reaction-limited regime, and small-sized particles should have better stability in the diffusion-limited regime.

Moreover, from the change in E_a^* we can predict the effect of coatings on NPs. Generally, for example, a negatively-charged conjugate attached to the surface of a Au-NP should increase resistance to flocculation as it increases electrostatic repulsion and decreases van der Waals attraction [45]. Indeed, the charge density of a conjugated Au-NP can be at least 10 times higher (>1 e/nm^2 when the surface packing density of singly-charged molecules reached 5×10^{14} cm^{-2}) than that of an unconjugated Au-NP (0.075 e/nm^2) [46, 57, 84, 85], contributing a significant increase in electrostatic repulsion. By coating the colloids with a covalently bound negatively-charged layer, colloidal stability may be improved since E_a^* is increased.

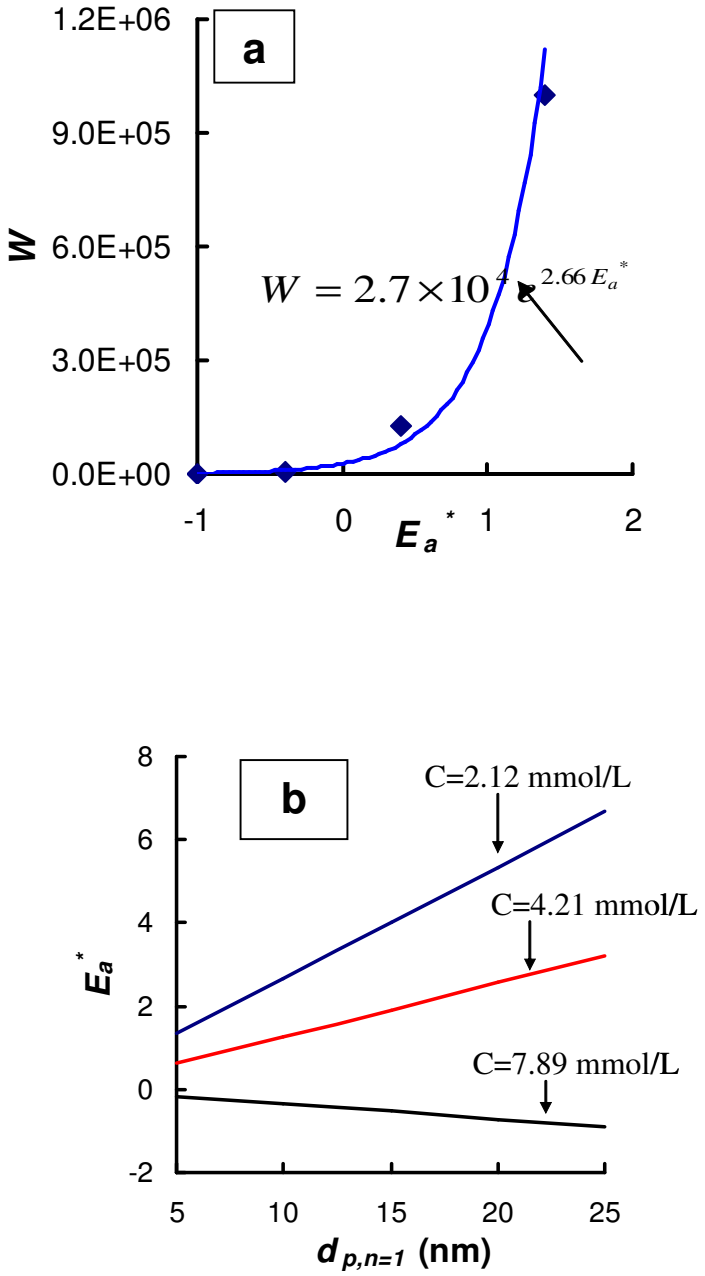

Figure 3.14: (a) Dimensionless analysis. W vs E_a^*. (b) E_a^* vs $d_{p,n=1}$ (primary particle diameter) obtained by Eq. 3.8 by assuming a constant surface charge density, 0.075 e/nm^2.

3.3 Extended Applications

3.3.1 Quantifying DNAs immobilization on Au Nanoparticles[86]

(1) Introduction

A key problem in nano-science and technology is how to determine the molecular surface coverage of nanoparticles derivatives with organic or biological molecules, particularly those without a fluorescent tag. Many approaches to functionalize engineered particles have been developed, but characterizing the number of moieties dotting the surface of a nanoparticle remains a critical technical challenge and a major barrier to commercial development. For example, measuring surface coverage will be key to the development, manufacturing, quality control, and regulatory approval of nanobiomaterials for therapeutic use. Additionally, surface coverage measurements will aid quantitative understanding of the results from nanoparticle sensors, enable engineering of particles for energy applications, and facilitate nanoparticle toxicology studies.

In Sec 3.1 we have demonstrated how to use ES-DMA to characterize Self-assembled layers on Au-NPs, which have a well-known packing structure and density. In this section we will explore more into the DNA immobilization process on Au-NP by using ES-DMA.

(2) Material and Preparation

Commercially available monodisperse Au colloids (20 nm, Ted Pella Inc.) were used in this study. Commercial custom oligonucleotides were synthesized and HPLC-purified by the vendor and used as-received without further purification. The 5' thiol-modified oligonucleotides were used without removing the protective S-$(CH_2)_6$OH group from the 5' end. For brevity, these oligonucleotides are referred to as T_xSH where *x* represents the number of thymine bases per strand, between 5 and 30.

Conjugated Au colloids were prepared by adding DNA at 200 μmol/L to the particles in the ratio of 50 μL per 850 μL of gold nanoparticles and the solution was allowed to react ≥18 h. Salts were added in two stages. First, 20 μL of 5 M NaCl and 10 μL of 1 mol/L K_2HPO_4 were added per 850 μL of particles. Second, after ≥3 hours an additional 149 μL, 373 μL, or 746 μL of salts was added to achieve the desired ionic strength, after which the reaction proceeded for ≥ 48 h.

The Au colloid solution was then centrifuged at 13200 rpm for 10 min in order to separate the colloids from the supernatant and to reduce the nonvolatile salt concentration. The supernatant was removed, leaving less than 20 μL in the vial, and replaced with an equivalent volume of >18.0 MΩ·cm water. The Au colloids easily redispersed by vortex mixing. Centrifugation followed by replacement of the supernatant with water more than one time resulted in flocculation of the bare Au colloids. Fortunately, DNA coated colloids displayed greater stability as they required duplicate centrifugation for solutions to which a second aliquot of salt was added. This indicates

that having DNA coatings effectively decreases van der Waals attraction between Au-NPs in solution to improve the stability of Au colloids.

Following centrifugation, typically 60 μL of a 20 mM ammonium acetate buffer (Sigma, 99.9 %, 0.2 S/m, pH 8) was added to 900 μL of solution to provide the requisite conductivity for the electrospray system. The addition proceeded in 10 μL aliquots interspersed by vortex mixing for ≥ 5 seconds, since direct addition tended to induce particle flocculation particularly for the bare particles.

(3) Results and Discussion

Figure 3.15 displays two ion mobility spectra: one (red) acquired from a solution containing bare Au nanoparticles nominally 20 nm in diameter and the other (blue) from a solution of 20 nm Au nanoparticles coated with thiol-modified ssDNA [$(dT)_{20}$-SH], where dT represents deoxythymine and the subscript denotes the number of bases per strand. Similar to the spectrum we observed in Sec 3.1 for SAM-coated Au-NPs, the first set of peaks (< 10 nm) corresponds to salt particles that result from the drying of droplets not containing Au particles. The second set of peaks (> 15 nm) represent Au particles, one bare and the other modified with $(dT)_{20}$-SH, both encrusted with any nonvolatile salts. Subtraction of the diameter of the bare particle from the DNA coated nanoparticle determines the apparent coating thickness, *H*, presented in Figure 3.16, which is twice the thickness of the coating layer on either side of the particle.

Using ES-DMA, Pease et. al. [86] investigated the dependence of the coating thickness on the number of dT nucleotides within a ssDNA strand, N_b, and the salt concentration, n_s. The dependence of the coating thickness on the number of bases per strand is related to the spatial configuration of the bases within the strand in the dry state. If the strands pack together tightly in a brush structure, similar to alkanethiol self-assembled monolayers, then the bases will extend into configurations that minimize inter-strand repulsion. Accordingly, the coating thickness should scale linearly with the contour length (i.e. the length of the ssDNA backbone), such that $H \sim N_b$. However, if packing allows for sufficient space between the strands, the bases will adopt a random coil configuration to maximize entropy (appropriate for dried strands), and then the coating thickness should be proportional to the linear end-to-end distance, $\langle x^2 \rangle^{1/2}$, of a strand. For freely jointed Gaussian chains, $\langle x^2 \rangle^{1/2} = c N_b^{1/2} N_k^{1/2} l_b$, where N_k represents the number of bases per Kuhn length ($l_k = N_k l_b$), l_b describes the length of a base, and $c = 0.62$ for end-tethered strands on a hard sphere with minimal surface attraction [appropriate for oligo(dT) strands on gold],[87] though a variety of prefactors remain available to account for surface-strand interactions.[88] Accordingly, we expect $H \sim N_b^{1/2}$, and, indeed, Figure 3.16 shows square root scaling to fit the data well. We, thus, conclude that the strands adopt a random coil configuration on the nanoparticle surface. [88, 89]

Knowing the configuration of the strands enables estimation of the surface coverage. Here we note that while the structure of the strands may change upon drying, the surface coverage does not. The drag force experienced by the coated particle in the DMA depends on the diameter of the particle, D, the projected area of the coiled strands characterized by $\langle x^2 \rangle^{1/2}$, and the surface coverage, σ. Knowing D and $\langle x^2 \rangle^{1/2}$ allows

inference of ρ from the data with a suitable model. We derive an analytical expression for the drag force for a "lumpy sphere" model, in which the ssDNA occupies N_m hemispherical caps of radius $\langle x^2 \rangle^{1/2}$, where N_m represents the number of caps around the 2-D projection of the particle's circumference. The apparent coating thickness, H, determines, N_m, which gives a measure of a strand's footprint. The surface coverage, consequently, may be approximated as $\sigma = [(D + H)^2 - D^2]^2 / [2\pi D \langle x^2 \rangle]^2$. A detailed derivation may be found in ref [86]. Using this model, we find ρ ranges between $2.0 \cdot 10^{12}$ and $6.9 \cdot 10^{13}$ strands/cm^2 as displayed in Figure 3.17, assuming $l_b = 0.59$ nm and $N_k = 3$ ($l_k = 1.8$ nm) for $N_b = 10$ to 30 bases.[90, 91] By comparison, "brushes" prepared under similar conditions have reported coverages from $1.0 \cdot 10^{13}$ to $2.0 \cdot 10^{13}$ strands/cm^2 for 12 mers on nanoparticles and $4.0 \cdot 10^{12}$ to $2.5 \cdot 10^{13}$ strands/cm^2 for 25 mers on planar substrates in reasonable agreement with the values derived from our model.

The relationship between the surface coverage and the salt concentration, n_s, of the solutions used for ssDNA adsorption is shown in Figure 3.17. Because DNA in solution is highly charged, strands anchored to the surface repel incoming strands due to charge-charge repulsion, i.e. through excluded volume effects.[90, 91] Decreasing the Debye length, λ_D, by increasing the ionic strength moderates this repulsion, allowing DNA to pack more tightly on the surface. An increase in the salt concentration accordingly leads to higher surface coverages as demonstrated in Figure 3.17.

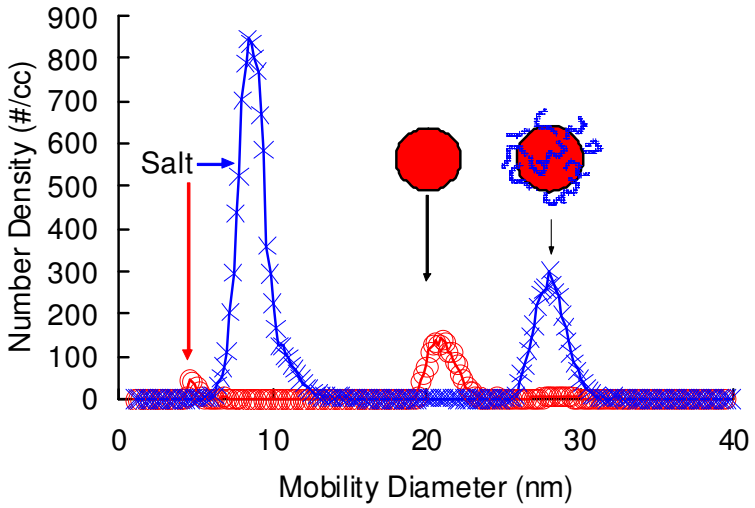

Figure 3.15: Two typical particle size distributions of nominally 20 nm Au particles, one bare (o) and the other coated with $(dT)_{20}$-SH (x). The difference between the two particle size distributions determines the apparent coating thickness.

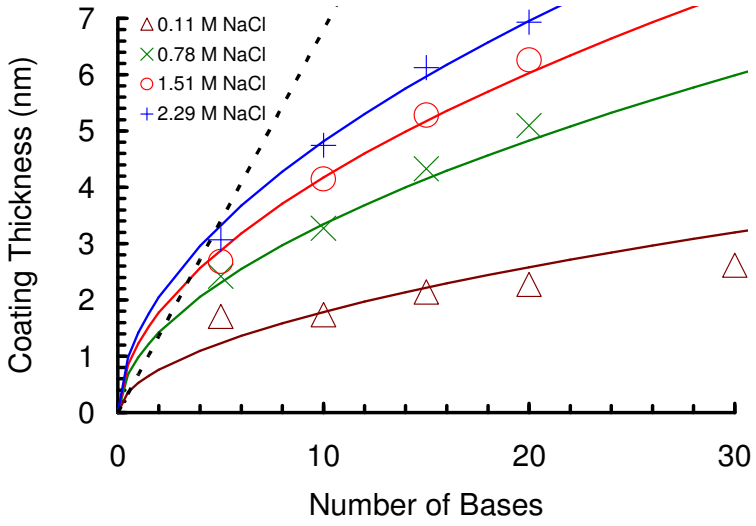

Figure 3.16: Apparent coating thickness, H, versus number of dT nucleotides per strand, N_b, for a variety of salt concentrations, n_s. The dashed and solid lines respectively represent fits for a contour length model for fully stretched out DNA versus that of a square root dependence [$H = 1.1 N_b^{0.53} n_s^{0.35}$ nm $L^{0.35}$ $mol^{-0.35}$] characteristic of strands coiled into low grafting density layers. The error range in the measurement of coating thickness is ± 0.3 nm.

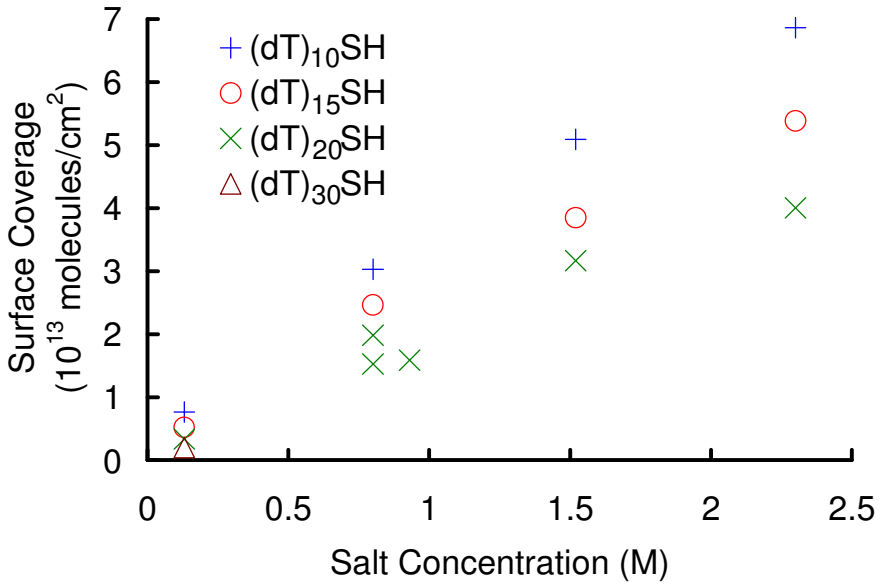

Figure 3.17: The surface coverage, σ, versus the salt concentration of the ssDNA solution in which the particles were immersed during preparation. Shorter strands display higher surface coverages because each strand occupies a smaller footprint.

3.3.2 Characterization of Viruses and Antibodies

(1) Introduction

We extend our ion-mobility approach to biologically interesting materials, such as antibodies and viruses. These materials are difficult to characterize with current instrumental techniques due to their small-size and low density. By ES-DMA we obtain the physical size and molecular weight of viruses and antibodies in solutions. From the change between ion-mobility spectra we track the stability of viruses, antibodies, and proteins in solution.

(2) Materials

Virus particles used in this study are PP7 and PR772, which are bacteriophages purified at FDA using CsCl gradient ultracentrifugation and suspended in a 10 mmol/L ammonium acetate buffer solution. Upon receipt, the solutions were further dialyzed for at least 18 hours into a 2 mmol buffer solution using 10 kg/mol molecular weight cut off Slide-A-Lyzer cartridges (Pierce) at room temperature. The purified samples were then analyzed by ES-DMA. The detailed information of ES-DMA operation has been described in the previous sections. Figure 18c depicts the temporal decomposition of the capsid. A sample of PR772 was stored at room temperature for 18 weeks after dialysis. Data collect after 18 weeks captures significant changes in the viral structure. Initially the size distribution consists of only intact viron and free capsomers as shown in Figure 18b.

Antibody samples were prepared as follows [92]. Polyclonal rabbit antibodies specific to the bacteriophage MS2 with a concentration of 2.8 mg/mL were obtained from Tetracore (Rockville, MD, product #TC-7004). To remove nonvolatile salts which may obscure the true size, 150 μL of as-received antibodies were dialyzed through with a slide-a-lyzer cartridge (Pierce) having a 10 kg/mol cut off. Dialysis proceeded for 18 hours in a 20 mmol/L ammonium acetate solution at pH 8. Protein low binding microcentrifuge tubes (Eppendorf) were used to prevent antibody adsorption to the sidewalls. Solutions to examine the effect of pH were prepared by adding 25.0 μL or 125 μL of glacial acetic acid or 50.0 μL of 30% ammonium hydroxide (J. T. Baker) and raising the volume to 1.00 mL with ammonium acetate solution of the specified strength. The samples were maintained at 4 °C until use.

(3) Results and Discussion

Figure 3.18 shows the particle size distribution of two different viruses as received from the FDA. Two distinct peaks exist forPP7 and three distinct peaks exist for PR772. The first peaks at ~10-20 nm present residue salts and the dissembled capsomeres in both PP7 and PR772. The second peaks represent the dried size of virus particles: PP7 is at 23.2 nm (3.18a) and PR772 at 59.2 nm (3.18b), which are consistent with the result reported by FDA (PP7 is 26 nm and PR772 is 55-60 nm) measured by electron microscopy[93, 94]. The peak shown at ~42 nm represent the doubly-charged PR772, which is less than 5% of singly charged PR772 (59.2 nm) and not interested in this size range.

This result shows that ES-DMA can effectively detect the presence of viruses and the corresponding number concentration measured in the gas phase.

After 18 weeks, as shown in Figure 18c, the primary peak of intact capsids were significantly decreased. In addition, this size distribution contains information regarding the structure of degrading products. The peak observed at 50 nm may be explained by partially disintegrated capsids. To confirm this point, we sampled the 50 nm-sized particles on a TEM grid by 3-hours of electrostatic deposition. TEM images (Figure 18d) clearly show irregularly shaped capsids for 50 nm-sized samples. This contrasts with particles collected at the 60 nm-sized, which display the straight sidewalls expected of the intact viron. As the multiple facet comprise the icosahedral viron, removal of several of these would be necessary to produce the 50 nm sized disintegrated capids.

Figure 3.19 shows typical ES-DMA spectra of antibody containing solutions[92]. The spectra show two types of peaks. The first peaks at 8.6 nm for the rabbit IgG in Fig. 3.19a and 9.4 nm for the human IgG in Fig 3.19b represent individual, intact antibodies. These mobility sizes represent the diameter of a sphere sustaining the same aerodynamic drag and charge as the antibody and are similar to the 9.3 nm size found for bovine IgG by Bacher, et al.[95] Variation among the sizes observed may be due to differences in molecular weight, glycosylation patterns (rabbit v. human v. bovine),[96] or the mechanical robustness of the antibody structure. The other peaks (>1) represent antibodies in different aggregation states.

The mobility size measured with ES-DMA can be compared with sizes obtained from protein crystallography, and detailed information is described in the reference [92].

We recently demonstrated a method to convert the projected areas, A_i, of DNA coated gold particles into the mobility size, d, under conditions of random orientation due to Brownian motion.[86, 97] We find,

$$d = \left(\frac{\sqrt{\pi}}{6} \sum_{i=1}^{3} A_i^{-1/2} \right)^{-1}, \tag{3.25}$$

where A_i represents the projected area of the i^{th} surface. Calculations of the sizes of aggregates were conducted by using the protein databank to obtain each of the three projections, A_{front}, A_{side}, and A_{top}[97] (giving A_{front} = 85.1 nm^2, A_{side} = 65.8 nm^2, A_{top} = 57.9 nm^2). Then using these A_i in Eq. 3.25, we calculated the mobility size of antibodies in different aggregation states. As shown in Table 3.3, our calculated size (by using the protein databank) compares well with the experimental observation in ion-mobility spectra.

Bacher, et al.,[95] correlated the mobility size (in nm) of a variety of biomolecules from antibodies to viruses with their molecular weights, M_w (in kg/mol). They assert proteins to be globular spheres of constant density and develop an empirical correlation,

$$M_w = -22.033 + 9.830\, d - 1.247\, d^2 + 0.228\, d^3, \tag{3.26}$$

which may be inverted to give $d = 1.832 M_w^{0.3256}$ (M_w for one antibody is 150kg/mol). The final column in Table 3.4 shows that this correlation does reasonably well for the monomers, dimers and trimers on which it was based. This result offers the opportunity to monitor protein aggregation, which is of particular concern in the pharmaceutical industry.

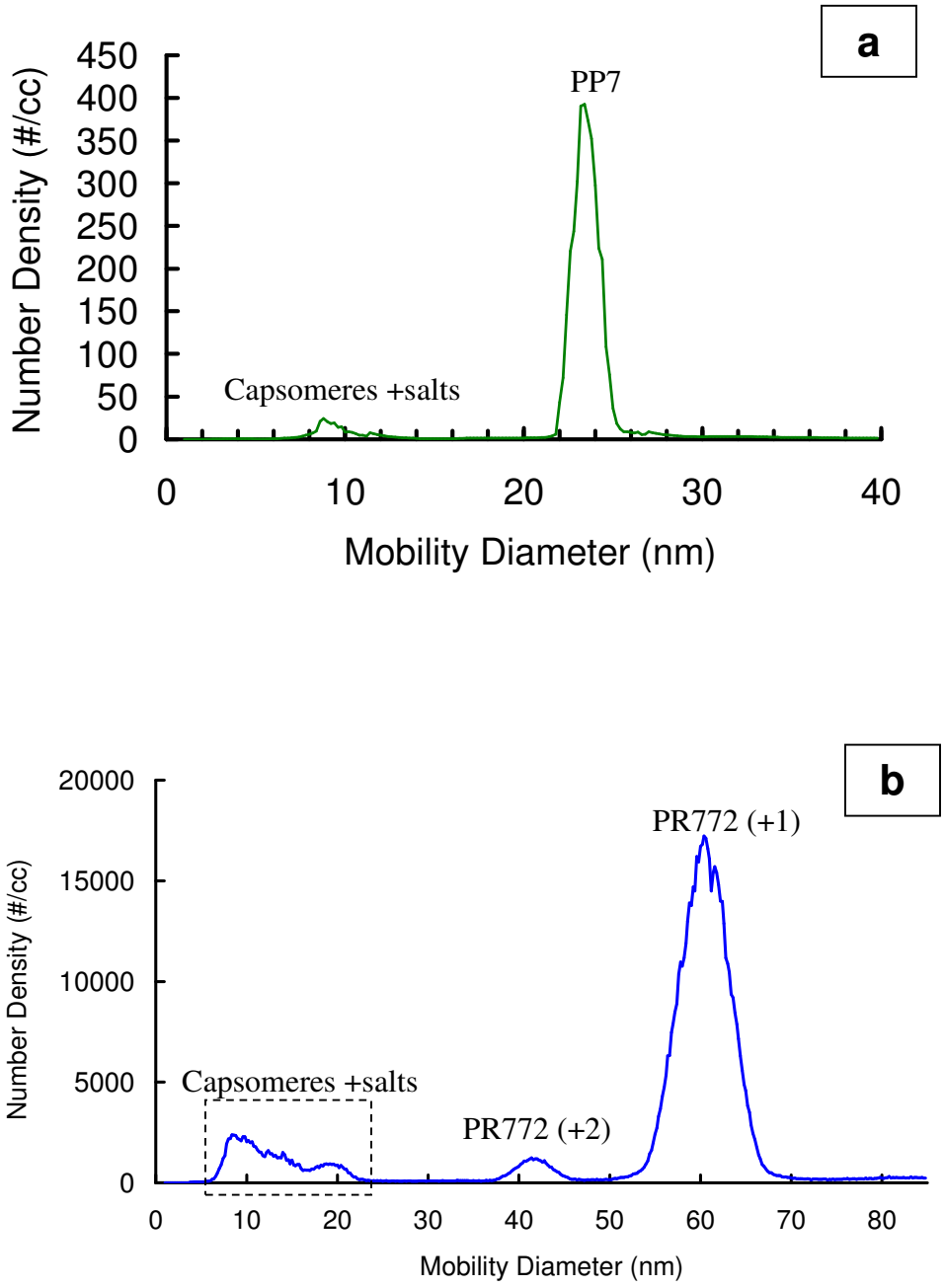

Figure 3.18: Ion-mobility spectrum of dialyzed virus particles. (a) PP7 (b) PR772.

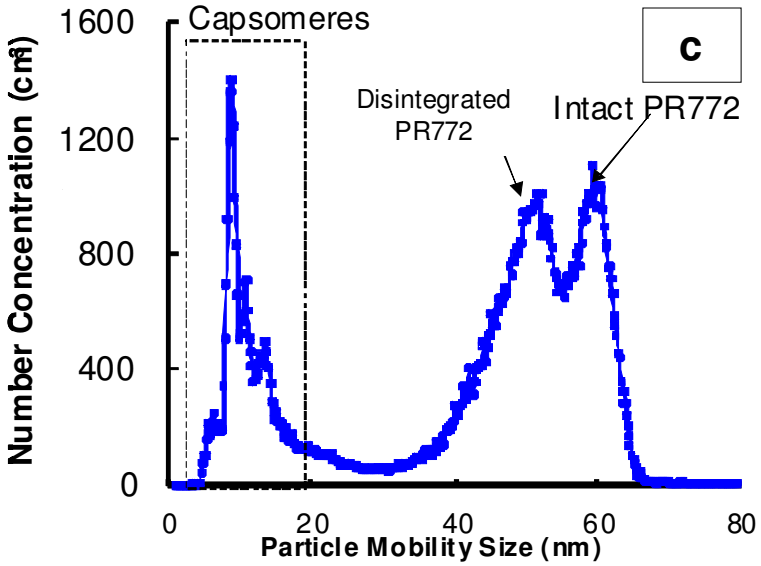

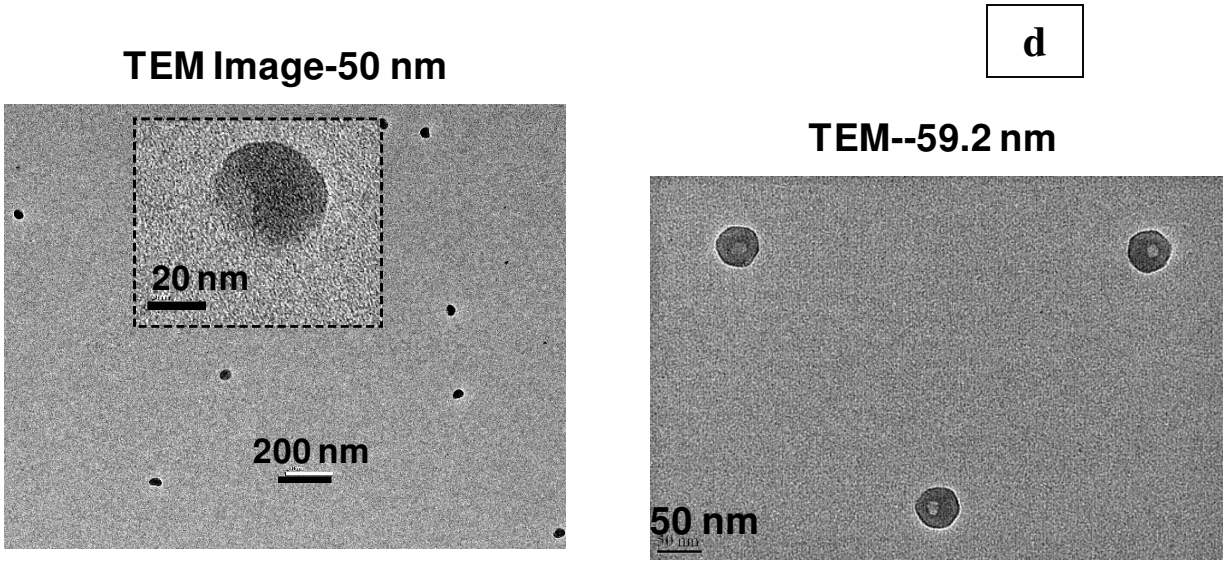

Figure 3.18: (c) Size distribution of PR772 sample after being dialyzed and stored at room temperature for 18 weeks. Samples were 5-times diluted by 2mM ammonium acetate solution. (d) TEM images of sized classified (50 nm, 60 nm) PR772 collected after 18 weeks.

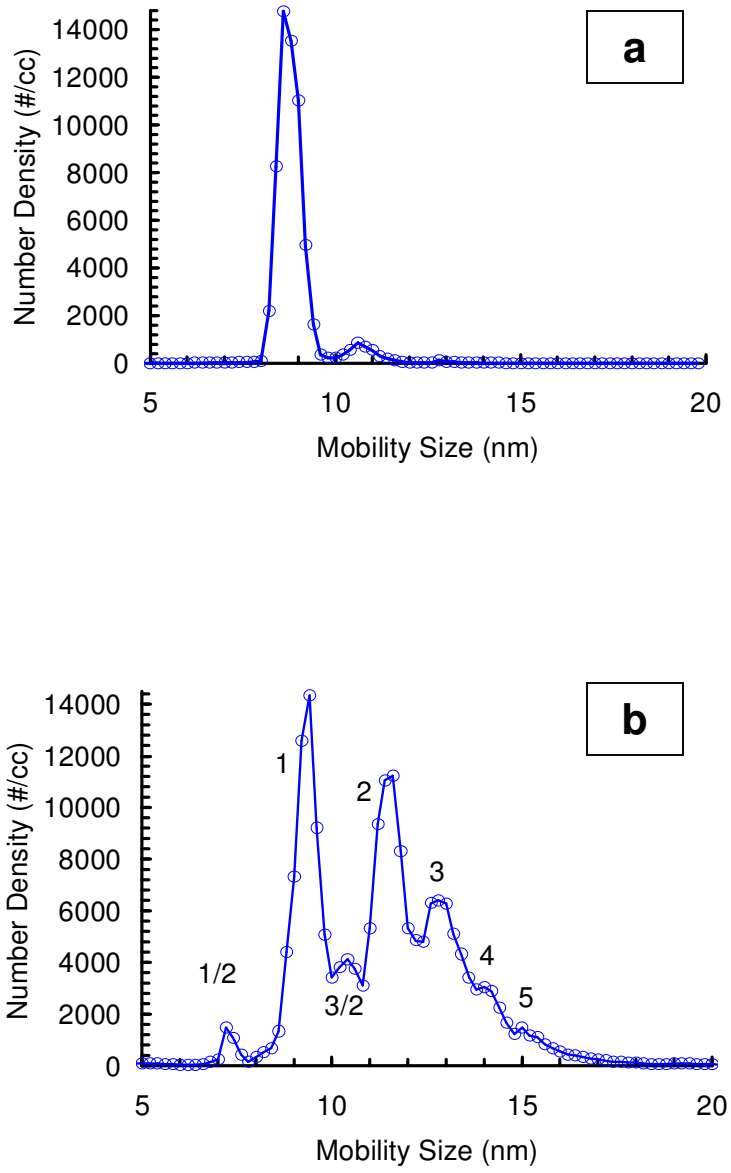

Figure 3.19: Number density versus the mobility size for various agglomerates of IgG. (a) Rabbit IgG at 18 µg/mL (120 nmol/L or $7.3 \cdot 10^{13}$ antibodies/mL) and pH 8 in 20 mmol/L ammonium acetate. (b) Human IgG previously lyophilized at approximately 75 µg/mL (500 nmol/L or $3.0 \cdot 10^{14}$ antibodies/mL) and pH 8 in 2.0 mmol/L ammonium acetate.

Table 3.4: Comparison of Measured and Calculated Mobility Size

Number of Antibodies	Measured Mobility Size (nm)	Calculated Size (nm)	M.w correlated Size (nm)
1	9.4	9.3	9.4
2	11.5	11.7	11.7
3	12.9	13.3	13.4
4	13.9	14.4	14.7

3.4 Conclusion

We have demonstrated a systematic approach to characterize functionalized self-assembled monolayers (SAMs) of alkylthiol molecules on Au nanoparticles with ES-DMA. The mobility measurement using a DMA has sufficient resolution to track both the packing density of SAMs, and the thermally induced desorption kinetics of SAMs from Au nanoparticles. For the size range (10-60 nm) of MUA-conjugated Au nanoparticles we considered, the curvature effect on SAM binding is evidently negligible, and the binding energy is consistent with similar studies of SAMs on flat surfaces. This study suggests the ES-DMA to be a useful tool for the study of packing density and stability of coatings on nanoparticles.

DNA-immobilization on Au nanoparticles has also been studied and an analytical model successfully correlated the projected surface area of DNA measured by ES-DMA to the surface packing. We estimate the packing density from the change of mobility size of Au nanoparticles and found that decreasing the Debye length is a promising way to increase the surface packing density.

We have applied this ES-DMA to characterize the flocculation process of nanoparticles in a solution. This instrument has sufficient resolution to identify the aggregation state of NPs and to track changes in the number concentration versus various ionic strengths and reaction time. For the range of reaction times we considered, we find the degree of flocculation to be proportional to the ionic strength and the residence time. From these data we determine the surface potential and surface charge density of commercial Au-NPs, which are consistent with literature reported values. From the rate

constant and energy barrier we can clearly delineate the critical salt concentration, and the boundary between the diffusion-limited and reaction-limited interactive potential regimes to be ~6.5 mmol/L.

This kinetic study using ES-DMA provides an opportunity to further characterize the size distribution of biological materials. Virus particles show a narrow particle size distribution (~±10%), which is contributed by their defined icosahedra structure. Antibody proteins (rabbit IgG and human IgG) show distinct peaks in their ion-mobility spectrum representing different aggregation states. These results can be applied to further research on antibody-virus reactions, protein aggregation processes, and virus degrading processes.

Chapter 4

Conclusion and Future Work

Electric fields can have a great impact on the nanoparticle transports, improving their synthesis, classification, characterization, and device integration. The directional forces generated by electric fields effectively minimize the effect of the non-directional forces and their random Brownian motion, which is a dominant factor in the trajectory of nano-sized materials.

Because the Coulomb interaction provides a directional force to overcome other non-directional external forces, both the deposition efficiency and the coverage selectivity of nanoparticles assembly processes can be improved. Using substrates patterned with a reverse biased p-n junction is a promising way to guide deposition because it provides a charged patterned surface with a strong electric field. Brownian dynamic simulation proves that electric field is the dominant factor in achieving high coverage selectivity of this electrostatic-directed particle assembly process. By using this model we can estimate the influence of other parameters in the device integration process, such as the dopant concentrations, material properties of nanoparticles and substrates, and the design of p-n junction patterns in the future research.

Applying electric fields toward size classification improved the size purity and the corresponding device performance of the bio-sensing processes. This promising result can be extended to other applications like nano-LED and energy harvesting materials.

The coupling effect between size-selected nanoparticles and the biological molecules is highly interesting, and this approach can be applied extensively in future research.

By using electric fields we can conduct a systematic time-of–flight measurement, namely electrospray-differential ion-mobility analysis (ES-DMA), which can be applied toward characterizing particle sizes of a variety of materials (nanoparticles, nanotubes, nanorods) and surface coatings. Our results indicate the potential of ES-DMA to quantify the coverage and configuration of biological molecules and organic coatings on nanoparticles. We considered the specific example of thiol-modified ssDNA and find it adopts a random coil configuration. We believe the analytical model to be valid generally for sufficiently long and flexible molecules.

With temperature programmed desorption, information regarding the surface binding energy of molecules adsorbed on Au nanoparticles can be obtained from the change of particle size (particle mobility). Moreover, the stability of different kinds of colloidal nano-materials can also be characterized by the ES-DMA system, and the kinetic information regarding solution-phase aggregation can be characterized from the change of particle size and the corresponding number concentration.

Additionally, ES-DMA can be further applied to biological reaction such as, and virus degradation, which can contribute to nano-therapeutics and bio-pharmaceuticals. In the future work we can apply internal standard materials, such as Au-NP and polystyrene, to improve the ES-DMA characterization. We expect to have a high-precision measurement on viral concentration in solution by scaling the virus concentration to a

known concentration of these standard materials, which may minimize the instrumental variation.

Real-time detection on the viruses-antibodies reaction is one of the most interesting projects in therapeutic technology. However, having a simple and precise characterization method is a challenge. Electrospray-ionization-masstroscopy (ESI-MS) would be a promising way, but the operating range is generally not sufficient (usually <100 Da), which limits its application. To solve this problem, ES-DMA seems to be a promising way, and the operating range can be achieved from 150 Da up to 10^{11} Da by choosing a suitable electrostatic classifier. The information such as the ratio of bonded antibodies to virus, the type of bindings, binding energy and the rate constant may be obtained. Moreover, protein flocculation is also highly interesting. My Ph.D. works on the Au-NPs and antibodies indicate that ES-DMA can also be used for on-line detecting the early stage of protein flocculation. Conclusively, Having a thorough study and a good cooperation between biologist, chemists and engineers may expand the capacity of this ES-DMA technique.

Appendix A

Data Acquisition and Analysis of ES-DMA

An Electrospray aerosol generator (TSI 3480) is used to deliver nano-sized materials from liquid phase (colloidal dispersion) to gas phase (aerosols). Colloidal samples are prepared in a 1.5 ml vial (non-conductive, disposable). To avoid electrical instability, the amount of samples required is at least 100 μL, and the position of capillary inlet in liquid should be away from the liquid surface.

To improve the stability of cone-jet at capillary tip, the carrier gas used was 1 Lpm of air plus 0.2 Lpm of CO_2. Particles leaving the TSI 3480 required a second neutralizer (Po 210 housing) to avoid the change of charge equilibrium during particle transport to DMA. Followed by a 2^{nd} neutralization, particles enter the electrostatic classifier (TSI 3080n). Because of the significant loss for nano-sized materials, especially when d_p <20nm, the residence time for particle transport should be minimized.

A high Voltage power supply (Bertan 5A) was used with the DMA. The ramp voltage is controlled by a home-made program developed using a LabView interface. Sheath flow rate for DMA depends on the size range of samples interested in. To avoid the electric breakdown at a higher applied voltage (V_{DMA}>3 kV), nitrogen is chosen as the carrier gas for DMA. For the unknown range or size larger than 40 nm, we use 10 Lpm N_2 sheath flow. If the size range is less than 40 nm, we use 30 Lpm N_2 as the sheath flow.

Sampling flow is fixed at 1 Lpm and connected to CPC. Number concentration of particles measured by CPC is also recorded by a personal computer using a home-made program. A simple description of this data acquisition program is shown in Figure A1. Note that the limit of our measured mobility size is 2.5 nm because of the limit of condensation particle counter (CPC). At the end of mobility analysis, particle size, applied voltage and number concentration are recorded in an ASCII file and then plotted by MS excel or Matlab as the ion-mobility spectra for the data comparison.

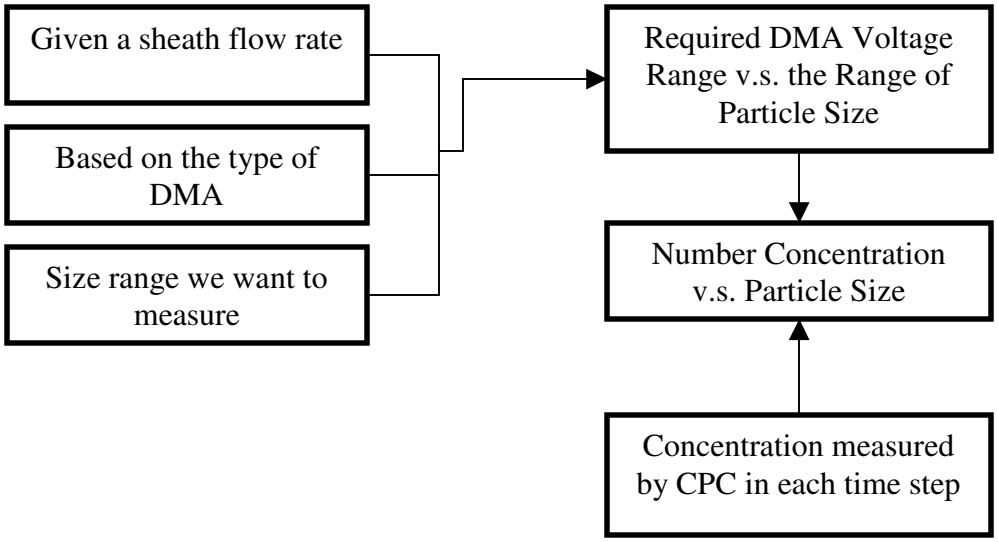

Figure A1: A simple description of data acquisition program of DMA.

Converting ion-mobility spectra measured after DMA into particle size distributions before DMA requires the following two steps:

1. Covert number concentration of singly-charged particle to the total number concentration of particles by considering the charge efficiency, β. (Eq. 1.9)

2. Considering the transfer function of DMA:

The number concentration detected by CPC represents the average concentration of the particles going through the collection slit of DMA. Hence the measured particle size, d_p, represents the average size for particles having a size ranging from d_p-Δd_p to d_p+Δd_p. A representative size distribution is shown in Figure A2a, where a concentration gradient, $dN_{g,p}/dd_p$ is an average value. The half-width of the size distribution, Δd_p, depends on the aerosol-to-sheath flow ratio ($Q_{aerosol}/Q_{sheath}$).

The resolution of particle mobility measured by DMA is define as follows,

$$\Delta Z_e = \left(\frac{Q_{aerosol}}{Q_{sheath}}\right) Z_e \qquad \text{(A.1)}$$

Converting into the resolution of particle mobility in free molecular regime into the resolution of particle size,

$$\Delta d_p = \left[1 - \left(\frac{Q_{aerosol}}{Q_{sheath}} + 1\right)^{-0.5}\right] d_p \qquad \text{(A.2)}$$

Next we consider the size distribution of these size-selected particles. Using a normal size distribution, Figure A2a can be converted into Figure A2b, which a

concentration gradient of specific sized particles can be obtained. Combining all the data points of $dN_{g,p}/dd_p$ the ion-mobility spectrum can be converted into a full size distribution similar to Figure 3.8 and 3.9, and the integration of peak represents the total number concentration of particles detected in the gas phase, which can be used to track the concentration change in liquid phase extensively.

This data analysis can be further improved by considering the diffusion loss. Generally, a standard calibration method is a promising to improve our concentration analysis. Considering the transfer function and the charge efficiency, a suggested detection limit is ~10^{10} particles/cm^{-3}. Because of the diffusion loss, a higher concentration was needed for the particles less than 20 nm.

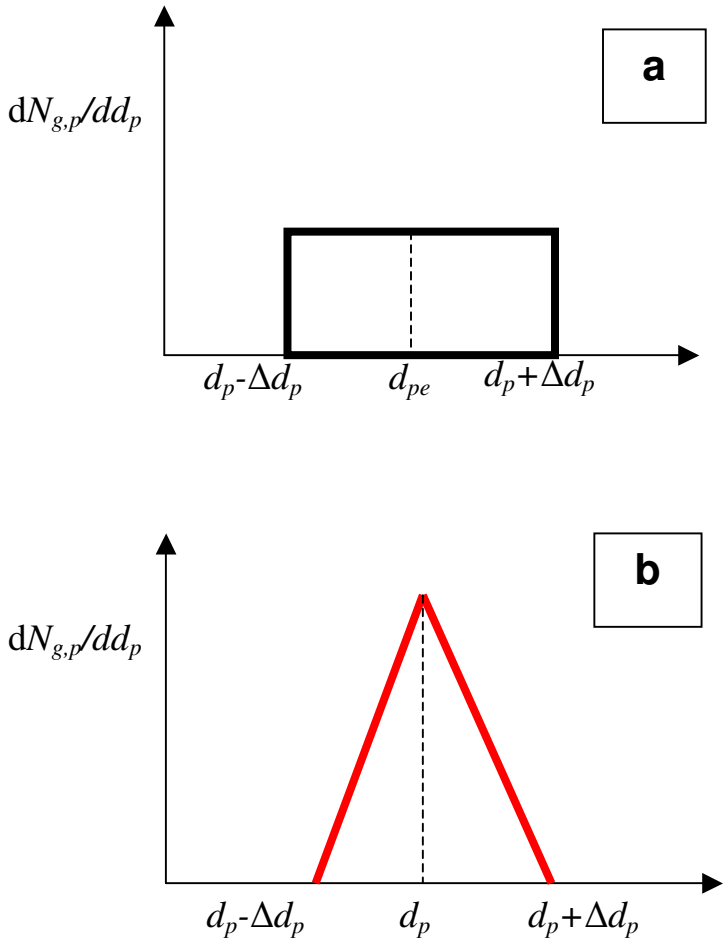

Figure A2: Transfer Function of DMA. (a) Determine the size range based on the resolution of DMA. (b) Use normal distribution to obtain the right number concentration gradient, $dN_{g,p}(d_p)/dd_p$.

Appendix B

Operations and Maintenance of ES-DMA

This appendix is referred from TSI 3480 manual[98] plus my personal operation experience.

B1. Preparing a Buffer Solution for Electrospray Ionization

A buffer solution is intended for the uses of:

(1) Rinse the capillary before, after, or between sample uses.

(2) Aconductive solvent for electrospray.

A 20 mM ammonium acetate buffer solution is prepared for these two reasons. The procedure for making this buffer solution (subsequently referred to as the standard buffer solution) is outlined here:

(1) Dissolve 0.77 grams of ammonium acetate in 500 milliliters of de-ionized water (18 MΩ.cm).

(2) Assuming the solution has an initial pH of ~7 (conductivity is 0.2 S/m), add 0.02 mL of 1 mol/L ammonium hydroxide to adjust the buffer solution pH to be 8.

For rinsing the capillary, we use this 20 mM buffer solution. For adjusting the conductivity of colloidal samples, 2-3 mM of ammonium acetate aqueous solution will be

preferred, which is prepared by mixing 100 mL of 20 mM ammonia acetate solutiomn with 850 mL of DI water.

B2. Operation of Electrospray Aerosol Generator

1. Following the operation procedures in TSI menu, check the viewing window to make sure the capillary tip is near the center of the viewing window.

2. Insert and open the sample vial into the chamber. To avoid contamination, platinum wire and the capillary should be rinsed by a clean DI water or clean buffer solution before inserting samples into the chamber. Note that the high voltage should be turned off if the bottom half of the pressure chamber is removed.

3. Turn the pressure regulator knob clockwise until the pressure gauge reads ~3.7 psi.

4. Turn the air to reach 1.0 Lpm and CO_2 to reach 0.2 Lpm.

5. The liquid should drip out of the 25 μm capillary about 2 minutes. For 40 μm capillary it takes less than one minute. If not, start doing trouble-shooting.

6. After seeing the dripping mode, **t**urn on the voltage to reach the stable cone-jet mode. Notes that do not increase the voltage exceeding ~10V while reaching stable otherwise a corona discharging effect could be occurred and the capillary tip will get clogged.

B3. Maintenance of Electrospray Aerosol Generator

(1) Periodic Maintenance

Periodic cleaning of several parts of the Electrospray is necessary to ensure proper performance. The service intervals depend on the type and concentration of aerosols generated with the Electrospray. The following maintenance schedule is suggested for the Electrospray:

(1.1) Purging the capillary Daily

1. Use 20 mM ammonia acetate buffer solution (volatile solution preferred) to run a pulsing/stable cone-jet mode, about 15-30 mins to flush away the sample residues.

2. Remove the buffer vial from the change and use only CLEAN Aair to PURGE the whole system. Overnight preferred.

3. If the capillary tip looks dirty, rinse it with ethanol.

(1.2) Clean the orifice at least once for two days. If the volumetric ratio of sample is high, clean it up once or twice a day. Use ethanol to rinse the orifice plate at first and then use DI water, repeating this process for 3 times. Then Use air to dry the orifice. Notes that the capillary should be removed from the orifice before cleaning the orifice.

The rest of system will also need maintenance, see the details in TSI menu.

B3.2. Special Maintenance

(1) Removing the Capillary

The capillary needs to be removed when cleaning any part of the Electrospray chamber or if the capillary becomes damaged or the capillary tip becomes dirty.

1. Remove power from the instrument and turn off all flows.

2. Remove the cover of Electrospray particle generator.

3. Loosen the hex nut on the inlet fitting but do not remove it.

4. Carefully pull the capillary from the capillary guide leaving the guide behind. If having difficulty to pull the capillary, it indicates that either the capillary guide or capillary outer wall is dirty. Use ethanol to clean it after pulling off the capillary.

5. Remove the high-voltage shield by loosening the mounting screw and pulling the high-voltage shield upward until it clears the capillary.

6. Loosen the hex nut on the high-voltage fitting but do not remove it.

7. Pull the capillary straight up until it clears the high-voltage fitting.

8. If the capillary tip appears dirty, rinse or soak the capillary tip in alcohol or a mild detergent.

(2) Installing the Capillary

1. Remove power from the instrument and turn off all flows.

2. Remove the cover.

3. Loosen the hex nut on the inlet fitting but do not remove it.

4. Remove the high-voltage shield by loosening the mounting screw and pulling the high-voltage shield upward.

5. Loosen the hex nut on the high-voltage capillary guide but do not remove it.

6. Insert the long end of the capillary into the high-voltage capillary guide until the end of the capillary reaches the end of the platinum wire. Twist the capillary until it becomes retained by the corkscrew of the platinum wire, and then tighten the hex nut on the high-voltage fitting.

7. Attach the high-voltage shield to the cabinet by sliding the capillary through the high-voltage shield, routing the high voltage wire through the groove in the bottom edge of the high voltage shield, and tightening the mounting screw.

8. Turn on the power to the instrument. If the cover is removed, high voltage will not be supplied to the instrument, but the capillary viewing window LED will turn on.

9. Carefully insert the capillary tip into the capillary guide. While looking through the viewing window, continue pushing the capillary into the capillary guide until the tip of the capillary first appears, then tighten the hex nut on the inlet fitting. If having difficulty to put in the capillary, it indicates the capillary guide is dirty.

Rinse the capillary guide and dry it before putting capillary. Do not force it otherwise the capillary will be stuck.

10. If the capillary is centered in the viewing window, installation is complete. If not, loosen the hex nut on the inlet fitting and adjust the position of tip.

B4. Selection of Differential Mobility Analyzer

Description of differential mobility analyzer (named as electrostatic classifier) is described in TSI menu[15]. For the size range larger than 50 nm. We use L-DMA (model 3080L). For the size range smaller than 50 nm, we used nano-DMA (model 3080N). In order to have a high resolution of ion-mobility, we used 10 Lpm for L-DMA. For Nano-DMA we use 10LPM for the sample size larger than 45 nm and 30 Lpm for the size less than 45 nm.

For the reason of achieving the maximum intensity of signal, we used all l.2 Lpm aerosol flow from electrospray and 1 Lpm signal (size-selected) flow. Note that avoiding the fluctuation of flow rates is the most important thing in order to have a precise mobility size comparison.

Reference

1. Parthangal, P. M.; Cavicchi, R. E.; Zachariah, M. R., A generic process of growing aligned carbon nanotube arrays on metals and metal alloys. *Nanotechnology* **2007,** 18, (18), -.
2. West, J. L.; Halas, N. J., Engineered nanomaterials for biophotonics applications: Improving sensing, imaging, and therapeutics. *Annual Review of Biomedical Engineering* **2003,** 5, 285-292.
3. Paciotti, G. F.; Myer, L.; Weinreich, D.; Goia, D.; Pavel, N.; McLaughlin, R. E.; Tamarkin, L., Colloidal gold: A novel nanoparticle vector for tumor directed drug delivery. *Drug Delivery* **2004,** 11, (3), 169-183.
4. Parthangal, P. M.; Cavicchi, R. E.; Zachariah, M. R., A universal approach to electrically connecting nanowire arrays using nanoparticles - application to a novel gas sensor architecture. *Nanotechnology* **2006,** 17, (15), 3786-3790.
5. Talley, C. E.; Jackson, J. B.; Oubre, C.; Grady, N. K.; Hollars, C. W.; Lane, S. M.; Huser, T. R.; Nordlander, P.; Halas, N. J., Surface-enhanced Raman scattering from individual Au nanoparticles and nanoparticle dimer substrates. *Nano Letters* **2005,** 5, (8), 1569-1574.
6. Corrigan, T. D.; Guo, S.; Phaneuf, R. J.; Szmacinski, H., Enhanced fluorescence from periodic arrays of silver nanoparticles. *Journal of Fluorescence* **2005,** 15, (5), 777-784.
7. Corrigan, T. D.; Guo, S. H.; Szmacinski, H.; Phaneuf, R. J., Systematic study of the size and spacing dependence of Ag nanoparticle enhanced fluorescence using electron-beam lithography. *Applied Physics Letters* **2006,** 88, (10), -.
8. Ermak, D. L.; Buckholz, H., Numerical-Integration of the Langevin Equation - Monte-Carlo Simulation. *Journal of Computational Physics* **1980,** 35, (2), 169-182.
9. Krinke, T. J.; Deppert, K.; Magnusson, M. H.; Schmidt, F.; Fissan, H., Microscopic aspects of the deposition of nanoparticles from the gas phase. *Journal of Aerosol Science* **2002,** 33, (10), 1341-1359.
10. Park, H.; Kim, S.; Chang, H. S., Brownian dynamic simulation for the aggregation of charged particles. *Journal of Aerosol Science* **2001,** 32, (11), 1369-1388.
11. Tsai, D. H.; Kim, S. H.; Corrigan, T. D.; Phaneuf, R. J.; Zachariah, M. R., Electrostatic-directed deposition of nanoparticles on a field generating substrate. *Nanotechnology* **2005,** 16, (9), 1856-1862.
12. Kruis, F. E.; Fissan, H.; Peled, A., Synthesis of nanoparticles in the gas phase for electronic, optical and magnetic applications - A review. *Journal of Aerosol Science* **1998,** 29, (5-6), 511-535.

13. Grobelny, J.; Tsai, D. H.; Kim, D. I.; Pradeep, N.; Cook, R. F.; Zachariah, M. R., Mechanism of nanoparticle manipulation by scanning tunnelling microscopy. *Nanotechnology* **2006,** 17, (21), 5519-5524.
14. Hind, W. C., Aerosol Technology, 2nd edition. **1998**.
15. *TSI Model 3080 Electrostatic Classifier Manual*. TSI inc.
16. H. Ibach, H. L., *Solid-State Physics, 2nd edition*. 1995.
17. Fuchs, N. A., *Geophys. Pura Appl.* **1963,** 56, 185.
18. *TSI Model 3089 Electrostatic Aerosol Sampler Manual*. TSI inc.
19. Cavicchi, R. E.; Walton, R. M.; Aquino-Class, M.; Allen, J. D.; Panchapakesan, B., Spin-on nanoparticle tin oxide for microhotplate gas sensors. *Sensors and Actuators B-Chemical* **2001,** 77, (1-2), 145-154.
20. Barry, C. R.; Lwin, N. Z.; Zheng, W.; Jacobs, H. O., Printing nanoparticle building blocks from the gas phase using nanoxerography. *Applied Physics Letters* **2003,** 83, (26), 5527-5529.
21. Barry, C. R.; Steward, M. G.; Lwin, N. Z.; Jacobs, H. O., Printing nanoparticles from the liquid and gas phases using nanoxerography. *Nanotechnology* **2003,** 14, (10), 1057-1063.
22. Jacobs, H. O.; Campbell, S. A.; Steward, M. G., Approaching nanoxerography: The use of electrostatic forces to position nanoparticles with 100 nm scale resolution. *Advanced Materials* **2002,** 14, (21), 1553-+.
23. Fissan, H.; Kennedy, M. K.; Krinke, T. J.; Kruis, F. E., Nanoparticles from the gas phase as building blocks for electrical devices. *Journal of Nanoparticle Research* **2003,** 5, (3-4), 299-310.
24. Krinke, T. J.; Deppert, K.; Magnusson, M. H.; Fissan, H., Nanostructured deposition of nanoparticles from the gas phase. *Particle & Particle Systems Characterization* **2002,** 19, (5), 321-326.
25. Krinke, T. J.; Fissan, H.; Deppert, K., Deposition of aerosol nanoparticles on flat substrate surfaces. *Phase Transitions* **2003,** 76, (4-5), 333-345.
26. Park, J. Y.; Phaneuf, R. J., Investigation of the direct electromigration term for Al nanodots within the depletion zone of a pn junction. *Journal of Applied Physics* **2003,** 94, (10), 6883-6886.
27. H. Ibach, H. L., *Solid-State Physics*. 2nd ed.; Springer: 1996.
28. Fissan, H. J.; Helsper, C.; Thielen, H. J., Determination of Particle-Size Distributions by Means of an Electrostatic Classifier. *Journal of Aerosol Science* **1983,** 14, (3), 354-357.
29. Chen, D. R.; Pui, D. Y. H.; Mulholland, G. W.; Fernandez, M., Design and testing of an aerosol sheath inlet for high resolution measurements with a DMA. *Journal of Aerosol Science* **1999,** 30, (8), 983-999.
30. ImageJ NIH.
31. Kulkarni, P.; Biswas, P., A Brownian dynamics simulation to predict morphology of nanoparticle deposits in the presence of interparticle interactions. *Aerosol Science and Technology* **2004,** 38, (6), 541-554.
32. Su, K. H.; Wei, Q. H.; Zhang, X.; Mock, J. J.; Smith, D. R.; Schultz, S., Interparticle coupling effects on plasmon resonances of nanogold particles. *Nano Letters* **2003,** 3, (8), 1087-1090.

33. Pluym, T. C.; Powell, Q. H.; Gurav, A. S.; Ward, T. L.; Kodas, T. T.; Wang, L. M.; Glicksman, H. D., Solid Silver Particle-Production by Spray Pyrolysis. *Journal of Aerosol Science* **1993,** 24, (3), 383-392.
34. Mahadevan, R.; Lee, D.; Sakurai, H.; Zachariah, M. R., Measurement of condensed-phase reaction kinetics in the aerosol phase using single particle mass spectrometry. *Journal of Physical Chemistry A* **2002,** 106, (46), 11083-11092.
35. Schlichting, H., *Boundary-Layer Theory*. 7th ed.; McGraw Hill: 1979.
36. Wiedensohler, A., An Approximation of the Bipolar Charge-Distribution for Particles in the Sub-Micron Size Range. *Journal of Aerosol Science* **1988,** 19, (3), 387-389.
37. Kan, H. C.; Phaneuf, R. J., Focusing of low energy electrons by submicrometer patterned structures in low energy electron microscopy. *Journal of Vacuum Science & Technology B-an International Journal Devoted to Microelectronics and Nanometer Structures-Processing Measurement and Phenomena* **2001,** 19, (4), 1158-1163.
38. Kadaksham, A. T. J.; Singh, P.; Aubry, N., Dielectrophoresis of nanoparticles. *Electrophoresis* **2004,** 25, (21-22), 3625-3632.
39. Phaneuf, R. J.; Kan, H. C.; Marsi, M.; Gregoratti, L.; Gunther, S.; Kiskinova, M., Imaging the variation in band bending across a silicon pn junction surface using spectromicroscopy. *Journal of Applied Physics* **2000,** 88, (2), 863-868.
40. Cao, Y. W.; Jin, R.; Mirkin, C. A., DNA-modified core-shell Ag/Au nanoparticles. *Journal of the American Chemical Society* **2001,** 123, (32), 7961-7962.
41. S.-H. Guo, S.-J. T., H.-C. Kan, D.-H. Tsai , M. R. Zachariah, and R. J. Phaneuf, Fluorescence Enhancement from Size-selected Nanoparticles on a Substrate: The Role of Field Enhancement and Shadowing. *Advanced Materials* **2007**.
42. D-H Tsai, T. H., H.C Kan, R. J. Phaneuf, and M. R. Zachariah, Spatial and size-resolved electrostatic-directed deposition of nanoparticles on a field-generating substrate: theoretical and experimental analysis. *Nanotechnology* **2007,** 18, 365201.
43. Corrigan, T. D.; Guo, S.-H.; Szmacinski, H.; Phaneuf, R. J., Systematic study ofhe size and spacing dependence of Ag nanoparticle enhanced fluorescence using electron-beam lithography. *Applied Physics Letters* **2006,** 88, 101112.
44. Sandhyarani, N.; Pradeep, T., Current understanding of the structure, phase transitions and dynamics of self-assembled monolayers on two- and three-dimensional surfaces. *International Reviews in Physical Chemistry* **2003,** 22, (2), 221-262.
45. Weisbecker, C. S.; Merritt, M. V.; Whitesides, G. M., Molecular self-assembly of aliphatic thiols on gold colloids. *Langmuir* **1996,** 12, (16), 3763-3772.
46. Brewer, S. H.; Glomm, W. R.; Johnson, M. C.; Knag, M. K.; Franzen, S., Probing BSA binding to citrate-coated gold nanoparticles and surfaces. *Langmuir* **2005,** 21, (20), 9303-9307.
47. Bottger, P. H. M.; Bi, Z.; Adolph, D.; Dick, K. A.; Karlsson, L. S.; Karlsson, M. N. A.; Wacaser, B. A.; Deppert, K., Electrospraying of colloidal nanoparticles for seeding of nanostructure growth. *Nanotechnology* **2007,** 18, (10), -.

48. Lenggoro, I. W.; Lee, H. M.; Okuyama, K., Nanoparticle assembly on patterned "plus/minus" surfaces from electrospray of colloidal dispersion. *Journal of Colloid and Interface Science* **2006,** 303, (1), 124-130.
49. Love, J. C.; Estroff, L. A.; Kriebel, J. K.; Nuzzo, R. G.; Whitesides, G. M., Self-assembled monolayers of thiolates on metals as a form of nanotechnology. *Chemical Reviews* **2005,** 105, (4), 1103-1169.
50. Lenggoro, I. W.; Xia, B.; Okuyama, K.; de la Mora, J. F., Sizing of colloidal nanoparticles by electrospray and differential mobility analyzer methods. *Langmuir* **2002,** 18, (12), 4584-4591.
51. Higgins, K. J.; Jung, H. J.; Kittelson, D. B.; Roberts, J. T.; Zachariah, M. R., Size-selected nanoparticle chemistry: Kinetics of soot oxidation. *Journal of Physical Chemistry A* **2002,** 106, (1), 96-103.
52. Liao, Y. C.; Roberts, J. T., Self-assembly of organic monolayers on aerosolized silicon nanoparticles. *Journal of the American Chemical Society* **2006,** 128, (28), 9061-9065.
53. Moulder, J. F., *Handbook of X-ray Photoelectron Spectroscopy*. Physical Electronics, Inc.: Eden Prairie, MN, 1995.
54. Kaufman, S. L., Electrospray diagnostics performed by using sucrose and proteins in the gas-phase electrophoretic mobility molecular analyzer (GEMMA). *Analytica Chimica Acta* **2000,** 406, (1), 3-10.
55. Giersig, M.; Mulvaney, P., Formation of Ordered 2-Dimensional Gold Colloid Lattices by Electrophoretic Deposition. *Journal of Physical Chemistry* **1993,** 97, (24), 6334-6336.
56. Nuzzo, R. G.; Dubois, L. H.; Allara, D. L., Fundamental-Studies of Microscopic Wetting on Organic-Surfaces .1. Formation and Structural Characterization of a Self-Consistent Series of Polyfunctional Organic Monolayers. *Journal of the American Chemical Society* **1990,** 112, (2), 558-569.
57. Schreiber, F., Structure and growth of self-assembling monolayers. *Progress in Surface Science* **2000,** 65, (5-8), 151-256.
58. Shuler, S. F.; Davis, G. M.; Morris, J. R., Energy transfer in rare gas collisions with hydroxyl- and methyl-terminated self-assembled monolayers. *Journal of Chemical Physics* **2002,** 116, (21), 9147-9150.
59. Hind, W., *Aerosol Technology*. Wiley-Interscience: 1998.
60. Terrill, R. H.; Postlethwaite, T. A.; Chen, C. H.; Poon, C. D.; Terzis, A.; Chen, A. D.; Hutchison, J. E.; Clark, M. R.; Wignall, G.; Londono, J. D.; Superfine, R.; Falvo, M.; Johnson, C. S.; Samulski, E. T.; Murray, R. W., Monolayers in three dimensions: NMR, SAXS, thermal, and electron hopping studies of alkanethiol stabilized gold clusters. *Journal of the American Chemical Society* **1995,** 117, (50), 12537-12548.
61. Nishida, N.; Hara, M.; Sasabe, H.; Knoll, W., Thermal desorption spectroscopy of alkanethiol self-assembled monolayer on Au(111). *Japanese Journal of Applied Physics Part 1-Regular Papers Short Notes & Review Papers* **1996,** 35, (11), 5866-5872.
62. Nishida, N.; Hara, M.; Sasabe, H.; Knoll, W., Dimerization process in alkanethiol self-assembled monolayer on Au(111). *Japanese Journal of Applied Physics Part 2-Letters* **1996,** 35, (6B), L799-L802.

63. Kim, T.; Lee, K.; Gong, M. S.; Joo, S. W., Control of gold nanoparticle aggregates by manipulation of interparticle interaction. *Langmuir* **2005,** 21, (21), 9524-9528.
64. Dinsmore, A. D.; Weitz, D. A., Direct imaging of three-dimensional structure and topology of colloidal gels. *Journal of Physics-Condensed Matter* **2002,** 14, (33), 7581-7597.
65. Elliott, S. L.; Butera, R. J.; Hanus, L. H.; Wagner, N. J., Fundamentals of aggregation in concentrated dispersions: Fiber-optic quasielastic light scattering and linear viscoelastic measurements. *Faraday Discussions* **2003,** 123, 369-383.
66. Enustun, B. V.; Turkevich, J., Coagulation of Colloidal Gold. *Journal of the American Chemical Society* **1963,** 85, (21), 3317-&.
67. Kobayashi, M.; Juillerat, F.; Galletto, P.; Bowen, P.; Borkovec, M., Aggregation and charging of colloidal silica particles: Effect of particle size. *Langmuir* **2005,** 21, (13), 5761-5769.
68. Lin, W.; Kobayashi, M.; Skarba, M.; Nu, C. D.; Galletto, P.; Borkovec, M., Heteroaggregation in binary mixtures of oppositely charged colloidal particles. *Langmuir* **2006,** 22, (3), 1038-1047.
69. Prieve, D. C.; Ruckenstein, E., Role of Surface-Chemistry in Primary and Secondary Coagulation and Hetero-Coagulation. *Journal of Colloid and Interface Science* **1980,** 73, (2), 539-555.
70. Russell W.B., S. D. A., and Schowalter W.R., *Colloidal Dispersion*. Cambridge: 1989.
71. Schowalter, W. R.; Eidsath, A. B., Brownian flocculation of polymer colloids in the presence of a secondary minimum. *Proceedings of the National Academy of Sciences of the United States of America* **2001,** 98, (7), 3644-3651.
72. Spielman, L. A., Viscous Interactions in Brownian Coagulation. *Journal of Colloid and Interface Science* **1970,** 33, (4), 562-&.
73. Weitz, D. A.; Lin, M. Y.; Lindsay, H. M., Universality Laws in Coagulation. *Chemometrics and Intelligent Laboratory Systems* **1991,** 10, (1-2), 133-140.
74. Andelman, P., *Soft Condensed Matter Physics in Molecular and Cell Biology*. Taylor and Francis: 2006.
75. Pease L. F. III, T. D.-H., Zangmeister R. A., Zachariah M. R., Tarlov M. J., Quantifying the Surface Coverage of Conjugate Molecules on Functionalized Nanoparticles. *Journal of Physical Chemistry C* **2007** (in press).
76. Tsai D.-H., Z. R. A., Pease L. F. III, Tarlov M. J., Zachariah M. R., Gas-Phase Ion-Mobility Characterization of SAM Functionalized Au Nanoparticles. *Langmuir* **2007**, (submitted).
77. Kim, S. H., Mulholland G. W. , Zachariah, M. R., Understanding Ion-Mobility and Transport Properties of Aerosol Nanowires. *Journal of Aerosol Science* **2007,** 38, 823-842.
78. Kim, S. H.; Zachariah, M. R., In-flight size classification of carbon nanotubes by gas phase electrophoresis. *Nanotechnology* **2005,** 16, (10), 2149-2152.
79. Kim, S. H.; Woo, K. S.; Liu, B. Y. H.; Zachariah, M. R., Method of measuring charge distribution of nanosized aerosols. *Journal of Colloid and Interface Science* **2005,** 282, (1), 46-57.

80. Hogan, C. J.; Kettleson, E. M.; Ramaswami, B.; Chen, D. R.; Biswas, P., Charge reduced electrospray size spectrometry of mega- and gigadalton complexes: Whole viruses and virus fragments. *Analytical Chemistry* **2006,** 78, (3), 844-852.
81. Leonard F. Pease III, D.-H. T., Rebecca A. Zangmeister, Joshua L. Hertz, Michael R. Zachariah, Michael J. Tarlov, Characterizing the Packing of Colloidal Nanoclusters. *Physical Review Letters* **2007**, (manuscript).
82. Sandler S.R., a. K. W., *Polymer Synthesis II*. 1977.
83. Friedlander, S. K., *Smoke, Dust, and Haze, Fundamental of Aerosol Dynamics, 2nd edition*. 2000.
84. Kimura, K.; Takashima, S.; Ohshima, H., Molecular approach to the surface potential estimate of thiolate-modified gold nanoparticles. *Journal of Physical Chemistry B* **2002,** 106, (29), 7260-7266.
85. Kunze, J.; Burgess, I.; Nichols, R.; Buess-Herman, C.; Lipkowski, J., Electrochemical evaluation of citrate adsorption on Au(111) and the stability of citrate-reduced gold colloids. *Journal of Electroanalytical Chemistry* **2007,** 599, (2), 147-159.
86. L.Pease, D.-H. T., R. Zangmeister, M.R. Zachariah and M.J. Tarlov, Quantifying the Surface Coverage of Conjugate Molecules on Functionalized Nanoparticles. *Journal of Physical Chemistry C* **2007**.
87. Kimura-Suda, H.; Petrovykh, D. Y.; Tarlov, M. J.; Whitman, L. J., Base-dependent competitive adsorption of single-stranded DNA on gold. *Journal of the American Chemical Society* **2003,** 125, (30), 9014-9015.
88. AdamutiTrache, M.; McMullen, W. E.; Douglas, J. F., Segmental concentration profiles of end-tethered polymers with excluded-volume and surface interactions. *Journal of Chemical Physics* **1996,** 105, (11), 4798-4811.
89. Netz, R. R.; Andelman, D., Neutral and charged polymers at interfaces. *Physics Reports-Review Section of Physics Letters* **2003,** 380, (1-2), 1-95.
90. Tinland, B.; Pluen, A.; Sturm, J.; Weill, G., Persistence length of single-stranded DNA. *Macromolecules* **1997,** 30, (19), 5763-5765.
91. Rief, M.; Clausen-Schaumann, H.; Gaub, H. E., Sequence-dependent mechanics of single DNA molecules. *Nature Structural Biology* **1999,** 6, (4), 346-349.
92. Leonard F. Pease III, J. T. E., De-Hhao Tsai, Michael R. Zachariah, Michael J. Tarlov, Determination of Protein IgG Antibody Flocculation with Differential Mobility Analysis. *manuscript in preparation* **2007**.
93. Brorson, K.; Sofer, G.; Robertson, G.; Lute, S.; Martin, J.; Aranha, H.; Haque, M.; Satoh, S.; Yoshinari, K.; Moroe, I.; Morgan, M.; Yamaguchi, F.; Carter, J.; Krishnan, M.; Stefanyk, J.; Etzel, M.; Riorden, W.; Korneyeva, M.; Sundaram, S.; Wilkommen, H.; Wojciechowski, P., "Large pore size" virus filter test method recommended by the PDA virus filter task force. *Pda Journal of Pharmaceutical Science and Technology* **2005,** 59, (3), 177-186.
94. Lute, S. e. a., Small virus retentive filter test method recommended by the PDA virus filter task force. I. Method development. *manuscript* **2007**.
95. Bacher, G.; Szymanski, W. W.; Kaufman, S. L.; Zollner, P.; Blaas, D.; Allmaier, G., Charge-reduced nano electrospray ionization combined with differential mobility analysis of peptides, proteins, glycoproteins, noncovalent protein complexes and viruses. *Journal of Mass Spectrometry* **2001,** 36, (9), 1038-1052.

96. Burton, D. R.; Dwek, R. A., Immunology - Sugar determines antibody activity. *Science* **2006,** 313, (5787), 627-628.
97. L.Pease, D.-H. T., R. Zangmeister, M.R. Zachariah and M.J. Tarlov, Charaterization of Packing Structure in Colloidal Nanoclusters. *Physical Review Letters, manuscript* **2007**.
98. *TSI Model 3480 Electrospray Aerosol Generator Manual* TSI inc.